



Letter Report
TLR-RES/DE/REB-2023-04

EVALUATING STATIC ISOTHERMAL MOLTEN SALT COMPATIBILITY WITH STRUCTURAL ALLOYS

Date: May 2023

Prepared by:
Oak Ridge National Laboratory
Bruce A. Pint
Dino Sulejmanovic
Rishi Pillai
Yi-Feng Su

Project Manager:
U.S. Nuclear Regulatory Commission
Wendy Reed

Prepared for U.S. Nuclear Regulatory Commission
Contract No. 3131002N0007 (Tasks 2, 3, 4 and 8)

DISCLAIMER

This report was prepared as an account of work sponsored by an agency of the U.S. Government. Neither the U.S. Government nor any agency thereof, nor any employee, makes any warranty, expressed or implied, or assumes any legal liability or responsibility for any third party's use, or the results of such use, of any information, apparatus, product, or process disclosed in this publication, or represents that its use by such third party complies with applicable law.

This report does not contain or imply legally binding requirements. Nor does this report establish or modify any regulatory guidance or positions of the U.S. Nuclear Regulatory Commission and is not binding on the Commission.

DOCUMENT AVAILABILITY

Reports produced after January 1, 1996, are generally available free via OSTI.GOV.

Website www.osti.gov

Reports produced before January 1, 1996, may be purchased by members of the public from the following source:

National Technical Information Service
5285 Port Royal Road
Springfield, VA 22161
Telephone 703-605-6000 (1-800-553-6847)
TDD 703-487-4639
Fax 703-605-6900
E-mail info@ntis.gov
Website <http://classic.ntis.gov/>

Reports are available to US Department of Energy (DOE) employees, DOE contractors, Energy Technology Data Exchange representatives, and International Nuclear Information System representatives from the following source:

Office of Scientific and Technical Information
PO Box 62
Oak Ridge, TN 37831
Telephone 865-576-8401
Fax 865-576-5728
E-mail reports@osti.gov
Website <https://www.osti.gov/>

This report was prepared as an account of work sponsored by an agency of the United States Government. Neither the United States Government nor any agency thereof, nor any of their employees, makes any warranty, express or implied, or assumes any legal liability or responsibility for the accuracy, completeness, or usefulness of any information, apparatus, product, or process disclosed, or represents that its use would not infringe privately owned rights. Reference herein to any specific commercial product, process, or service by trade name, trademark, manufacturer, or otherwise, does not necessarily constitute or imply its endorsement, recommendation, or favoring by the United States Government or any agency thereof. The views and opinions of authors expressed herein do not necessarily state or reflect those of the United States Government or any agency thereof.

Materials Science and Technology Division

***EVALUATING STATIC ISOTHERMAL MOLTEN SALT
COMPATIBILITY WITH STRUCTURAL ALLOYS***

Bruce Pint, Dino Sulejmanovic, and Rishi Pillai

May 2023

**Prepared by
OAK RIDGE NATIONAL LABORATORY
Oak Ridge, TN 37831
managed by
UT-BATTELLE LLC
for the
US DEPARTMENT OF ENERGY
under contract DE-AC05-00OR22725**

CONTENTS

CONTENTS.....	iii
FIGURE LIST.....	v
TABLE LIST.....	ix
ABBREVIATION LIST.....	xi
1. EXECUTIVE SUMMARY.....	1
2. INTRODUCTION.....	3
3. Evaluation of the Effects of Salt Volume to Sample Surface Ratio.....	5
3.1 EXPERIMENTAL PROCEDURE.....	5
3.2 Results.....	6
3.3 Discussion.....	10
3.4 Summary.....	12
4. Effect of Capsule Container (Task 3).....	13
4.1 Experimental Procedure.....	13
4.2 Results.....	14
4.3 FLiNaK results.....	23
4.4 Discussion.....	43
4.5 Summary.....	45
5. Effect of the Test Methodology (Task 2).....	46
5.1 Experimental Procedure.....	46
5.1.1 Capsule Tests.....	46
5.1.2 Crucible Test.....	46
5.1.3 Glovebox Test.....	47
5.2 Results.....	48
5.3 Discussion.....	51
5.4 Summary.....	52
6. Comments on Characterization (task 8).....	53
7. Example Data Comparing Flowing and Static Experiments.....	56
8. Recommendations on Evaluating Compatibility Data.....	60
8.1 How to evaluate technologies.....	60
9. Acknowledgements.....	62
10. References.....	63

FIGURE LIST

Figure 3-1. (a) schematic of standard inner and outer molten salt capsule and (b) capsules loaded in box furnace for isothermal testing.	6
Figure 3-2. Specimen mass loss for 316H specimens after 500 h at 700°C in purified NaCl-MgCl ₂ as a function of the salt volume/specimen surface area ratio in Mo and 316H capsules.	7
Figure 3-3. Light microscopy of polished sections of representative specimens (a,e) V/SA = 6.5, (b,f) V/SA = 2.5, (c,g) V/SA = 0.9 and (d,h) V/SA = 0.2.	8
Figure 3-4. (a) SEM backscattered electron image of a polished section of the 316H specimen exposed for 500 h at 700°C in static NaCl-MgCl ₂ salt V/SA=6.5, (b-f) associated EDS maps of (a).	9
Figure 3-5. EDS line scans from 316H specimens exposed for 500 h at 700°C in purified NaCl-MgCl ₂ salt (a) V/SA = 6.5, (b) V/SA = 2.5, (c) V/SA = 0.9 and (d) V/SA = 0.2.	9
Figure 3-6. Box and whisker plots of the depth of attack based on the light microscopy images of selected specimens.	10
Figure 3-7. Specimen mass loss for 316H and Hastelloy N specimens exposed to Cl and F salts at 550°-700°C.	11
Figure 3-8. Arrhenius plot of V/SA over specimen mass change slopes from Figure 3-7.	11
Figure 4-1. Images of polished 316H specimens with (a) BN rod or (b) graphite rod to hold the specimen upright in the salt.	14
Figure 4-2. Specimen mass loss for 316H specimens in 5 different container materials after 500 h at 700°C in purified NaCl-MgCl ₂ with and without a Mg addition.	15
Figure 4-3. Light microscopy of polished sections of representative 316H specimens exposed for 500 h at 700°C in (a-e) NaCl-MgCl ₂ and (f-j) NaCl-MgCl ₂ with Mg; (a,f) 316H capsule, (b,g) Mo capsule, (c,h) Ni capsule, (d,i) BN container and (e,j) graphite container.	15
Figure 4-4. Box and whisker plots of the depth of attack based on the light microscopy images of selected specimens exposed to NaCl-MgCl ₂ salt with and without Mg additions.	16
Figure 4-5. (a) SEM image of a polished cross-section of a 316H specimen exposed for 500 h at 700°C to NaCl-MgCl ₂ salt with a Mg addition in a 316H capsule and (b-h) EDS maps of the same region.	16
Figure 4-6. EDS profile from the line shown in Figure 4-5a from a 316H specimen exposed for 500 h at 700°C to NaCl-MgCl ₂ salt with a Mg addition exposed in a 316H capsule.	17
Figure 4-7. Post-test metallic salt impurities measured by ICP-OES in the NaCl-MgCl ₂ salt with and without Mg in the various capsule experiments.	17
Figure 4-8. (a) SEM image of a polished cross-section of a 316H specimen exposed for 500 h at 700°C to NaCl-MgCl ₂ salt in a Mo capsule and (b-h) EDS maps of the same region.	18
Figure 4-9. EDS profile from the line shown in Figure 4-8a from a 316H specimen exposed for 500 h at 700°C to NaCl-MgCl ₂ salt in a Mo capsule.	18
Figure 4-10. (a) SEM image of a polished cross-section of a 316H specimen exposed for 500 h at 700°C to NaCl-MgCl ₂ salt in a Ni capsule and (b-h) EDS maps of the same region.	19
Figure 4-11. (a) SEM image of a polished cross-section of a 316H specimen exposed for 500 h at 700°C to NaCl-MgCl ₂ salt in a Ni capsule and (b) EDS profile from the line shown in (a).	19
Figure 4-12. EDS line profiles from the Ni capsule after exposure for 500 h at 700°C to NaCl-MgCl ₂ salt with and without a Mg addition.	20
Figure 4-13. (a) SEM image of a polished cross-section of a 316H specimen exposed for 500 h at 700°C to NaCl-MgCl ₂ salt with a Mg addition in a Ni capsule and (b-h) EDS maps of the same region.	20

Figure 4-14. (a) SEM image of a polished cross-section of a 316H specimen exposed for 500 h at 700°C to NaCl-MgCl ₂ salt with a Mg addition in a Ni capsule and (b) EDS profile from the line shown in (a).....	21
Figure 4-15. (a) SEM image of a polished cross-section of a 316H specimen exposed for 500 h at 700°C to NaCl-MgCl ₂ salt in a BN container and (b-f) EDS maps of the same region.....	21
Figure 4-16. EDS profile from the line shown in Figure 4-15a of a 316H specimen exposed for 500 h at 700°C to NaCl-MgCl ₂ salt in a BN container.	22
Figure 4-17. (a) SEM image of a polished cross-section of a 316H specimen exposed for 500 h at 700°C to NaCl-MgCl ₂ salt with a Mg addition in a BN container and (b-h) EDS maps of the same region.	22
Figure 4-18. (a) SEM image of a polished cross-section of a 316H specimen exposed for 500 h at 700°C to NaCl-MgCl ₂ salt in a graphite container and (b-f) EDS maps of the same region.	23
Figure 4-19. EDS profile from the line shown in Figure 4-18a of a 316H specimen exposed for 500 h at 700°C to NaCl-MgCl ₂ salt in a graphite container.....	23
Figure 4-20. Specimen mass loss for 316H and 709 specimens in 5 different container materials after 500 h at 700°C in dried FLiNaK salt.	24
Figure 4-21. Light microscopy of polished sections of representative (a-d,h) 316H and (e-g) 709 specimens exposed for 500 h at 700°C in FLiNaK salt (a,e) 316H capsule, (b,f) Mo capsule, (c,g) Ni capsule, (d) BN container and (h) graphite container.....	25
Figure 4-22. Box and whisker plots of the depth of attack based on the light microscopy images of selected specimens exposed to FLiNaK salt.....	25
Figure 4-23. (a) SEM image of a polished cross-section of a 316H specimen exposed for 500 h at 700°C to dried FLiNaK salt in a 316H crucible and (b-f) EDS maps of the same region.	26
Figure 4-24. EDS profile from the line shown in Figure 4-23a of a 316H specimen exposed for 500 h at 700°C to dried FLiNaK salt in a 316H capsule.....	26
Figure 4-25. (a) SEM image of a polished cross-section of a 709 specimen exposed for 500 h at 700°C to dried FLiNaK salt in a 316H crucible and (b-f) EDS maps of the same region.	27
Figure 4-26. EDS profile from the line shown in Figure 4-25a of a 709 specimen exposed for 500 h at 700°C to dried FLiNaK salt in a 316H capsule.....	27
Figure 4-27. Post-test metallic salt impurities measured by ICP-OES in the dried FLiNaK salt in the various capsule experiments with 316H and 709 specimens.	28
Figure 4-28. (a) SEM image of a polished cross-section of a 316H specimen exposed for 500 h at 700°C to dried FLiNaK salt in a Mo crucible and (b-f) EDS maps of the same region.	28
Figure 4-29. EDS profile from the line shown in Figure 4-28a of a 316H specimen exposed for 500 h at 700°C to dried FLiNaK salt in a Mo capsule.	29
Figure 4-30. (a) SEM image of a polished cross-section of a 709 specimen exposed for 500 h at 700°C to dried FLiNaK salt in a Mo capsule and (b-f) EDS maps of the same region.	29
Figure 4-31. (a) SEM image of a polished cross-section of a 709 specimen exposed for 500 h at 700°C to dried FLiNaK salt in a Mo capsule and (b) EDS profile from the line shown in (a).....	30
Figure 4-32. (a) SEM image of a polished cross-section of a 316H specimen exposed for 500 h at 700°C to dried FLiNaK salt in a Ni capsule and (b-f) EDS maps of the same region.....	30
Figure 4-33. EDS profile from the line shown in Figure 4-28a of a 316H specimen exposed for 500 h at 700°C to dried FLiNaK salt in a Ni capsule.	31
Figure 4-34. (a) SEM image of a polished cross-section of a 709 specimen exposed for 500 h at 700°C to dried FLiNaK salt in a Ni capsule and (b-f) EDS maps of the same region.....	31
Figure 4-35. EDS profile from the line shown in Figure 4-34a of a 709 specimen exposed for 500 h at 700°C to dried FLiNaK salt in a Ni capsule.	32
Figure 4-36. (a) SEM image of a polished cross-section of a 316H specimen exposed for 500 h at 700°C to dried FLiNaK salt in a BN crucible and (b-f) EDS maps of the same region.	32

Figure 4-37. (a) SEM image of a polished cross-section of a 316H specimen exposed for 500 h at 700°C to dried FLiNaK salt in a BN container and (b) EDS profile from the line shown in (a).	33
Figure 4-38. (a) SEM image of a polished cross-section of a 316H specimen exposed for 500 h at 700°C to dried FLiNaK salt in a graphite crucible and (b-f) EDS maps of the same region.	33
Figure 4-39. (a) SEM image of a polished cross-section of a 316H specimen exposed for 500 h at 700°C to dried FLiNaK salt in a graphite container and (b) EDS profile from the line shown in (a).	34
Figure 4-40. Specimen mass loss for Ni-based Hastelloy N and 617 specimens in 3 different container materials after 500 h at 700°C in dried FLiNaK salt.	35
Figure 4-41. Light microscopy of polished sections of representative Ni-based alloys (a-c) Hastelloy N and (d-f) 617 specimens exposed for 500 h at 700°C in FLiNaK salt (a,d) 316H capsule, (b,e) Mo capsule and (c,f) Ni capsule.	36
Figure 4-42. Box and whisker plots of the depth of attack based on the light microscopy images of selected specimens exposed to FLiNaK salt.	36
Figure 4-43. (a) SEM image of a polished cross-section of a Hastelloy N specimen exposed for 500 h at 700°C to dried FLiNaK salt in an alloy N crucible and (b-f) EDS maps of the same region.	37
Figure 4-44. EDS profile from the line shown in Figure 4-39a of a Hastelloy N specimen exposed for 500 h at 700°C to dried FLiNaK salt in an alloy N capsule.	37
Figure 4-45. Post-test metallic salt impurities measured by ICP-OES in the dried FLiNaK salt in the various capsule experiments with alloys N and 617 specimens.	38
Figure 4-46. (a) SEM image of a polished cross-section of a Hastelloy N specimen exposed for 500 h at 700°C to dried FLiNaK salt in a Mo capsule and (b-f) EDS maps of the same region.	38
Figure 4-47. a) SEM image of a polished cross-section of a Hastelloy N specimen exposed for 500 h at 700°C to dried FLiNaK salt in a Mo capsule and (b) EDS profile from the line shown in (a).	39
Figure 4-48. (a) SEM image of a polished cross-section of a Hastelloy N specimen exposed for 500 h at 700°C to dried FLiNaK salt in a Ni capsule and (b-f) EDS maps of the same region.	39
Figure 4-49. EDS profile from the line shown in Figure 43a of a Hastelloy N specimen exposed for 500 h at 700°C to dried FLiNaK salt in a Ni capsule.	40
Figure 4-50. (a) SEM image of a polished cross-section of a 617 specimen exposed for 500 h at 700°C to dried FLiNaK salt in an alloy N capsule and (b-f) EDS maps of the same region.	40
Figure 4-51. (a) SEM image of a polished cross-section of a 617 specimen exposed for 500 h at 700°C to dried FLiNaK salt in an alloy N capsule and (b) EDS profile from the line shown in (a).	41
Figure 4-52. (a) SEM image of a polished cross-section of a 617 specimen exposed for 500 h at 700°C to dried FLiNaK salt in a Mo capsule and (b-f) EDS maps of the same region.	41
Figure 4-53. (a) SEM image of a polished cross-section of a 617 specimen exposed for 500 h at 700°C to dried FLiNaK salt in a Mo capsule and (b) EDS profile from the line shown in (a).	42
Figure 4-54. (a) SEM image of a polished cross-section of a 617 specimen exposed for 500 h at 700°C to dried FLiNaK salt in a Ni capsule and (b-f) EDS maps of the same region.	42
Figure 4-55. EDS profile from the line shown in Figure 4-54a of a 617 specimen exposed for 500 h at 700°C to dried FLiNaK salt in a Ni capsule.	43
Figure 4-56. EDS line profiles from capsules exposed for 500 h at 700°C to NaCl-Mg ₂ Cl salt with 316H specimens in a 316H capsule with a Mg addition.	44

Figure 4-57. Specimen mass loss for 316H and Hastelloy N specimens exposed to three different batches of FLiNaK.....	45
Figure 5-1. A picture of the experimental setup for the crucible test to assess compatibility of alloys in molten salts.....	47
Figure 5-2. A picture showing the glovebox crucible test with electrochemistry setup.	48
Figure 5-3. Schematic of the electrochemical measurement configuration used during the glovebox tests.	48
Figure 5-4. Mass change data of 316H specimens exposed in commercial and laboratory FLiNaK using three different exposure methods.	49
Figure 5-5. Corrosion potential transients measured from 100 h exposures in two FLiNaK salts.	50
Figure 5-6. Light microscopy of the 316H specimens exposed for 100 h at 700°C in (a-c) commercial FLiNaK and (d-f) laboratory FLiNaK using (a,d) capsules, (b,e) crucibles and (c,f) glovebox.....	50
Figure 5-7. Box and whisker plots of the depth of attack based on the light microscopy images of selected specimens exposed to FLiNaK salt for 100 h at 700°C using three different methods.....	51
Figure 5-8. Pre- and post-test metallic salt impurities measured by ICP-OES in the commercial (C) or laboratory (L) FLiNaK salt in the capsule (cap), glovebox (GB) and crucible (pot) experiments.....	51
Figure 6-1. Concentration of metallic species in FLiNaK salt before and after flowing for 1000h in the 316H TCL. [Raiman 2022].	54
Figure 7-1. Normalized mass change of 316H samples exposed to FLiNaK salt for 1000 h in capsules or a TCL. Actual temperatures of the loop specimens were 552°C and 647°C.	57
Figure 7-2. Specimen mass change of 316H specimens as a function of estimated exposure temperature in flowing FLiBe salt compared to values for FLiNaK salt after 1,000 h.	57
Figure 7-3. Measured depth of attack on alloy tubing exposed to flowing Cl salt as a function of exposure time with some tests stopped due to plugging of the loop.....	58

TABLE LIST

Table 3-1. Alloy compositions determined by inductively coupled plasma and combustion analyses.....	5
Table 3-2. Summary of measured values from 316H specimens exposed for 500 h at 700°C in purified NaCl-MgCl ₂	7
Table 4-1. Salt impurities (in ppmw) determined by combustion analysis (O,H) and inductively coupled plasma-mass spectroscopy	14
Table 4-2. Summary of capsules analyzed after salt exposure for 500 h at 700°C.....	43
Table 5-1. Task 2 test matrix showing the V/SA ratios for three test methods	46

ABBREVIATION LIST

ASME	American Society of Mechanical Engineers
DFT	Density Functional Theory
DOE	Department of Energy
EDS	Energy dispersive spectroscopy
EPMA	electron probe microanalysis
EXAFS	Extended X-ray Absorption Fine Structure
FEFF	software for <i>ab initio</i> multiple scattering calculations of XAFS & XANES
FIB	Focused ion beam
GB	Glovebox
GDOES	glow discharge optical emission spectroscopy
ICP-OES	inductively coupled plasma-optical emission spectroscopy
LCAC	low carbon arc cast (molybdenum)
MSRE	Molten Salt Reactor Experiment
NMR	Nuclear Magnetic Resonance
ORNL	Oak Ridge National Laboratory
PDF	pair-distribution function
PIM	polarizable ionic model
SA	Surface Area (of specimen)
SEM	Scanning electron microscopy
SS	Stainless steel
TCL	Thermal convection loop
UHP	Ultra-High Purity (gas)
V	Volume (of salt)
WDS	Wavelength dispersive spectroscopy
XAFS	X-ray Absorption Fine Structure
XANES	X-ray Absorption Spectroscopy

1. EXECUTIVE SUMMARY

Molten salt reactors, particularly the fluid-fueled types, pose unique considerations with regards to compatibility of materials with molten salt coolants during operations. A sound understanding of materials compatibility would be crucial to monitor and manage the life-time performance of nuclear structural components. In a previous report [Raiman 2021], several technical gaps were identified, including the lack of systematic data collection using static corrosion methodologies, and testing standards. Though this report did not attempt to develop a standard for molten salt corrosion static experiments, it provides insights on key experimental parameters used to assess molten salt compatibility of structural materials in static halide salts that could aid development of test standards. In addition, the report advances the understanding of materials compatibility in MSR designs to prepare the NRC staff for future licensing reviews. Because of the variety of MSR designs under consideration, with both fast and thermal neutron spectra, the experiments used representative fluoride and chloride salts. Selected experiments were conducted to quantify the effect of different parameters including:

- (1) the effect of changing the ratio of molten salt volume (V) to alloy specimen surface area (SA) (Task 4);
- (2) changing the capsule material (Task 3); and
- (3) changing the test methodology including welded capsules, sealed crucibles and open crucibles in a glove box (Task 2).

For most experiments, type 316H stainless steel (SS) test specimens were exposed to both FLiNaK salt and NaCl-MgCl₂ salt with and without Mg additions. Triplicates of each condition were conducted to gather statistical information on the differences and all the experiments were conducted at 700°C for 100-500 h.

For experiment set 1 (V/SA), the volume (V) of salt was held constant but different size specimens (thereby changing the surface area) of type 316H stainless steel were exposed in Mo and 316 capsules to create a wide range of V/SA ratios. A high V/SA condition resulted in much larger mass losses compared to smaller V/SA experiments and the scatter in mass losses also increased. Capsule materials investigated included 316, alloy N, Mo, Ni, boron nitride (BN) and graphite. Additional experiments were conducted with specimens of alloy 709 SS and Ni-based alloys Hastelloy N and 617. While some results can be understood based on changes in the V/SA ratios, the overall results suggest that the container material is significantly influencing the observed reaction perhaps by reacting with the salt or the dissolution reaction products. Because of the relatively short exposure times, identifying specific reactions with the capsule material was difficult (experiment set 2). Comparing capsule experiments to crucible tests (where the container was not welded shut) without welding showed similar results (experiment set 3). However, when the same experiment was repeated in an uncovered crucible in a glovebox, higher mass losses were observed for 316H SS specimens exposed to two batches of FLiNaK salt with different levels of impurities. The advantage of the glovebox experiment is that electrochemical measurements can be made on the salt during the exposure. Electrochemistry is another technique that can be used to characterize the

salt and monitor its evolution with time as a means to understand and predict the longer term compatibility between the salt and materials it contacts.

In addition to the three experimental variables investigated in Tasks 2-4, Task 8 used various characterization techniques to evaluate the effect on the microstructure in each case. In addition to specimen mass change, the primary strategy was examining metallographic cross-sections of the specimens to determine the depth of attack and characterize any gradient in the composition due to selective dissolution in the salt using scanning electron microscopy and energy dispersive spectroscopy (SEM/EDS). In addition to examining the corroded specimen, characterizing the salt chemistry before and after the exposure was very helpful in understanding the reactions.

While it is not possible to define an optimal static experiment, these tests were conducted to highlight how choices in experimental parameters can affect static test results. These factors need to be considered when reviewing data. In addition, it should be noted that static, isothermal exposures are not expected to produce the same results as more prototypic flowing salt tests in a thermal gradient where mass transfer can occur from the hot leg to the cold leg and inhibit coolant flow with possible catastrophic effects. A static experiment that shows limited attack either because of a low V/SA or the addition of a redox agent like Mg to the salt does not resolve the issue of salt compatibility in the system.



2. INTRODUCTION

In considering the methodology for conducting molten halide salt compatibility experiments, there are no applicable test standards. There is an ISO standard (ISO 17245:2015 [ISO standard 2015]) for molten salts related to hot corrosion (primarily sulfates with SO_2/SO_3 in the atmosphere) but that is not relevant to halide salts (i.e., chlorides and fluorides) where salt purity and environmental $\text{O}_2/\text{H}_2\text{O}$ ingress can drastically affect the compatibility results with structural materials. In the absence of standards, a wide range of experimental conditions can be found in the literature which makes interpreting these results particularly difficult. Even when standards are specified, it is very difficult to get the same result in round robin testing [Pint 2020]. Some experimental variables are application-dependent, including the type of material and salt composition to be investigated as well as exposure times and temperatures. The researcher-determined experimental variables include the salt container material, the size of the specimen, the amount of salt used and the atmosphere of the experiment. Perhaps the most significant factor is whether the salt will be static (and usually isothermal) or flowing, especially in a temperature gradient [Vreeland 1953], which is more representative of the application. Obviously, static salt tests are much easier to conduct and thus a majority of published data are static tests [Raiman 2018].

In traditional liquid metal compatibility experiments, solubility of reaction products (e.g., Ni has a high solubility in Pb) is recognized as being an important factor in compatibility [Epstein 1957, Weeks 1971, DeVan 1979, Chopra 1985, Guminski 1994]. Refractory elements like Mo have a low solubility in most liquid metals and thus are relatively inert and can be used as containers in compatibility experiments [Vreeland 1953, Pint 2013]. Because of the importance of solubility, the volume (V) of liquid relative to the surface area (SA) of the exposed specimen is an important parameter. A large V/SA ratio (~ 10 , with units of cm^3/cm^2) was considered necessary to prevent the liquid from quickly saturating with the reaction product, although this ratio was not always achieved. For a static isothermal capsule compatibility experiment, a small specimen mass loss suggests minimal dissolution in the liquid and provides an indication of good compatibility between that material and the liquid. However, if only a small amount of liquid is used, saturation of specimen elements in the liquid can minimize the mass change and suggest better compatibility than is the case.

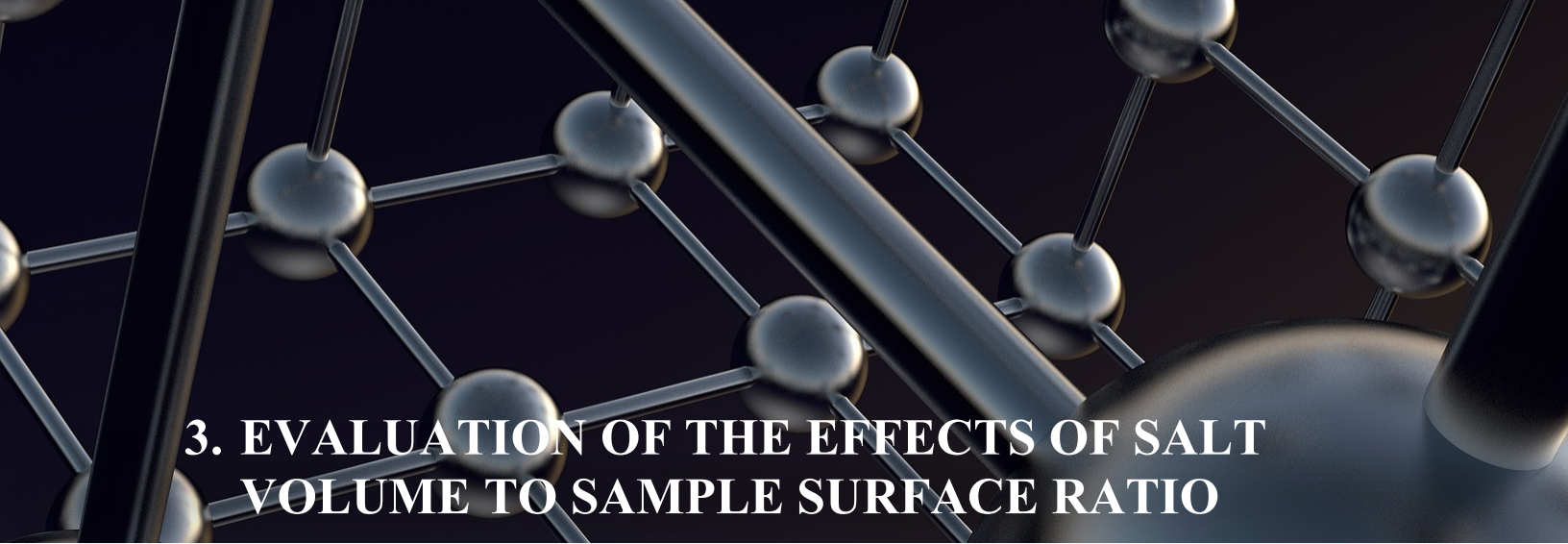
The methodology for evaluating molten salt and liquid metal compatibility at Oak Ridge National Laboratory (ORNL) is little changed after more than 70 years [Vreeland 1953]. Static experiments are conducted in capsules that are welded shut to prevent impurity ingress during the experiment. Flowing experiments begin with thermal convection loops (TCLs) and proceed to forced convection or pumped loops, which cost ~ 10 times more than a TCL experiment. Compatibility issues can be identified and studied in TCL experiments, while pumped loops investigate a broader range of thermal hydraulic issues at prototypical operating conditions in addition to compatibility [Yoder 2014, Britsch 2019]. This project is focused on static experiments but includes a comparison of static results to flowing experiments.

In all of the experiments, standard exposures of 100-500 h at 700°C were used and primarily type 316H stainless steel specimens were exposed. Several companies developing molten salt reactors are initially considering 316H as a structural material and the alloy has a maximum operating temperature of 650°C -

700°C due to high temperature strength limitations [Viswanathan 2001]. The first series of experiments determined the effect of varying the V/SA ratio on the mass change observed in a molten salt capsule experiment using purified NaCl-MgCl₂ salt. In order to achieve large variations in V/SA, Mo and 316H capsules were used—when the specimen is the same as the container SA is greatly increased. Molybdenum capsules were selected because Mo forms less stable halide compounds [Zhang 2018, Pint 2019] and therefore is somewhat inert to the salt. The effect of capsule material was investigated more broadly in the second set of experiments where both NaCl-MgCl₂ and FLiNaK salt were used as well as other specimens including alloy 709 SS and Ni-based alloys N and 617. It can be argued that the easiest capsule test to understand is a monometallic experiment where the container and the specimen are made from the same material to ensure no galvanic interaction takes place. However, this is impractical for some materials that are not readily available in tube form. Screening a large number of candidates in a static capsule test using the candidate material as both specimen and container (i.e., a monometallic capsule experiment) would require a much larger amount of material and much more machining, assuming the material could be machined into a capsule or crucible. The other issue with a monometallic experiment is that the inherently small V/SA ratio (because the SA includes the specimen and the container) results in small mass changes because the salt attacks both the specimen and the container.

These first two sets of experiments used welded capsules with the recognition that welded capsules are not widely used in the molten salt research community. (ORNL uses welded capsules to ensure that there is no impurity ingress into the salt during the experiment.) Thus, the final set of experiments compared welded capsule results to other techniques including crucible tests in a sealed (bolted) container (i.e., no welding) and crucible tests in a glovebox where electrochemical measurements are possible [e.g., Vignarooban, 2015]. In this final set of experiments, the same container material (Mo) was used in each test with similar V/SA ratios.

It is not clear that there is an optimal way to conduct static experiments; for example, a preferred V/SA ratio or “universal” capsule material. It also is apparent that there are not simple “correction factors” to account for these effects. However, it is important to be aware of all these test parameters and their influence on reported results. The final section of the report discusses how this information may be useful in interpreting data submitted to the NRC and help to put diverse data sets into context.



3. EVALUATION OF THE EFFECTS OF SALT VOLUME TO SAMPLE SURFACE RATIO

3.1 EXPERIMENTAL PROCEDURE

Isothermal capsule testing of 316H specimens (composition in Table 3-1) was conducted in 316H (composition certified within specification but not specifically determined) or low carbon arc cast Mo inner capsules (25 mm outer diameter x 100 mm tall x 1.2mm wall). To achieve a range of salt volume (cm^3) to specimen surface area (cm^2) V/SA ratios, 316H specimens of different sizes (~6 x 12 x 1.5mm, ~20 x 12 x 1.5mm, and 12.5 outer diameter x 1.75 wall thickness x 25 mm long tubes) were used with the coupons polished to a 600-grit finish. (If the container was the same material as the specimen, then the portion of the capsule exposed to salt was included in the SA calculation. The surface area of the wire and nipple shown in Figure 3-1a were ignored.) The NaCl-MgCl₂ salt was made from reagent-grade salts and purified using a two-step process [Young 1993, Chen 1993, Mayes 2018, Kurley 2019]: first the carnallite method was used to mix the salt with NH₄Cl (2:1) and then heat to 450°C for 2 h and 750°C for 1 h; the next step was sparging at 650°C (1) with CCl₄ for 35-40 h, (2) with ultra-high purity (UHP) Ar for 0.5h, (3) with Ar-4%H₂ for 12-15 h and (4) with UHP Ar for 0.5 h. Capsules were loaded with ~28 g of salt in an Ar-filled glove box with impurity levels ≤ 1 ppm O₂ and H₂O. The specimens were cleaned prior to exposure using deionized water, acetone and methanol. The specimens were attached to one end of the capsule using Mo or type 316L SS wire (to match the capsule material) and the capsules were sealed inside the glove box using autogenous (i.e. no filler metal) gas tungsten arc welding at the top and bottom of the capsule, Figure 3-1a. The inner capsules were then placed inside type 304 stainless steel outer capsules and sealed using electron beam welding to provide secondary containment and prevent the primary capsule from oxidizing. The capsules were exposed in a box furnace in laboratory air for 500 h at 700°C, Figure 3-1b. After exposure, the capsules were inverted to allow the salt to drain away from the specimen [Vreeland 1953, Raiman 2019] and the capsules were then opened in the same glove box. After exposure, the specimens were ultrasonically cleaned using deionized water at 40°C. Before and after exposure, the specimens were weighed using a Mettler Toledo XP205 balance with an accuracy of $\sim \pm 0.04$ mg. Selected specimens were then sectioned and mounted in epoxy and polished for characterization using light microscopy and a Tescan model MIRA3 scanning electron microscope (SEM) equipped with energy dispersive x-ray spectroscopy (EDS). ImageJ software was used to quantify the reaction product thickness with at least 30 measurements made from each cross-section.

Table 3-1. Alloy compositions determined by inductively coupled plasma and combustion analyses

Alloy	Fe	Ni	Cr	Mo	C	Other
316H	68.5	10.4	16.5	1.9	0.034	1.5Mn,0.3Si,0.4Cu,0.1Co,0.03N
709	51.3	25.2	20.1	1.5	0.064	0.9Mn,0.4Si,0.2Nb,0.02Ti,0.15N
Hast N	3.7	71.9	7.2	16.0	0.052	0.5Co,0.3Mn,0.3Si,0.01N,0.007S

617 [†]	1.6	54.1	22.2	8.6	0.05	11.6Co,1.1Al,0.4Ti,0.1Mn,0.1Si,<0.002S
------------------	-----	------	------	-----	------	--

[†] heat number 314626 from Thyssen Krupp [Wright 2014]



Figure 3-1. (a) schematic of standard inner and outer molten salt capsule and (b) capsules loaded in box furnace for isothermal testing. The wire and nipple used to secure the specimen in (a) were the same material as the capsule

3.2 RESULTS

The capsule experiments were conducted in triplicate to determine reproducibility. The mass change results are shown in Figure 3-2 as a function of the salt volume/specimen surface area ratio in Mo and 316H capsules. For the smallest V/SA ratio, unexpected small mass *gains* were observed as summarized in Table 3-2. Mass losses increased with increasing V/SA, as the 316H specimen decreased in size, i.e., more salt volume per unit surface area. The standard deviation also increased with increasing V/SA, Table 3-2. For comparison, a Mo coupon in a Mo capsule (V/SA ~0.2) resulted in a mass loss of 0.2 mg/cm² for the Mo specimen, which was larger than expected. This comparison was not conducted in triplicate so the reproducibility was not assessed.

Figure 3-3 shows representative light microscopy images of the four types of specimen geometries. Consistent with the mass change data, the most significant attack was observed for the largest V/SA condition with a small 316H coupon in a Mo capsule, Figures 3-3a and 3-3e. Deep void penetrations were observed, which is typical for alloys exposed to molten salts [Koger 1973, Olson 2015, Zheng 2016, Sun 2018, Ding 2019, Pint 2019, Raiman 2019]. Considerably less attack was observed for the large coupon specimens with a V/SA = 2.5, Figures 3-3b and 3-3f. Much less attack was observed for the other specimens with lower V/SA values. At high magnification, surface roughening was observed but no void formation, Figures 3-3g and 3-3h. There was no clear evidence of why a mass gain would be measured on the 316H specimens in a 316H capsule, Figures 3d and 3h. Of course, a 0.1 mg/cm² mass gain corresponds to ~100nm of metal or 0.6µm of oxide so higher resolution characterization is needed. The Mo specimen is not shown but small pits were observed on the surface with an average depth of 0.5µm.

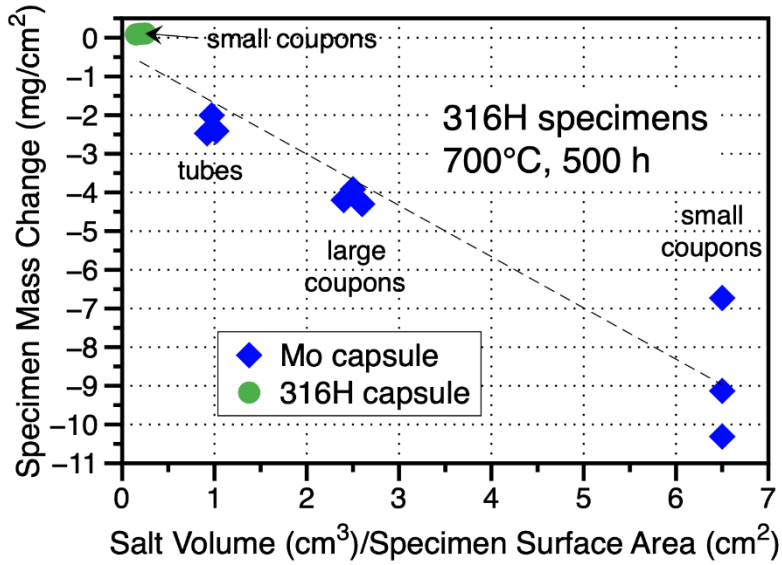


Figure 3-2. Specimen mass loss for 316H specimens after 500 h at 700°C in purified NaCl-MgCl₂ as a function of the salt volume/specimen surface area ratio in Mo and 316H capsules. Three separate capsule experiments were conducted at each condition.

Table 3-2. Summary of measured values from 316H specimens exposed for 500 h at 700°C in purified NaCl-MgCl₂

V/SA ratio	Mass change (mg/cm ²)	Average mass change (mg/cm ²)	Standard Deviation (mg/cm ²)
6.5	-10.3, -9.1, -6.7	-8.72	1.83
2.5	-4.3, -4.2, -3.9	-4.14	0.20
0.9	-2.5, -2.4, -2.0	-2.30	0.25
0.2	0.09, 0.10, 0.11	0.10	0.01

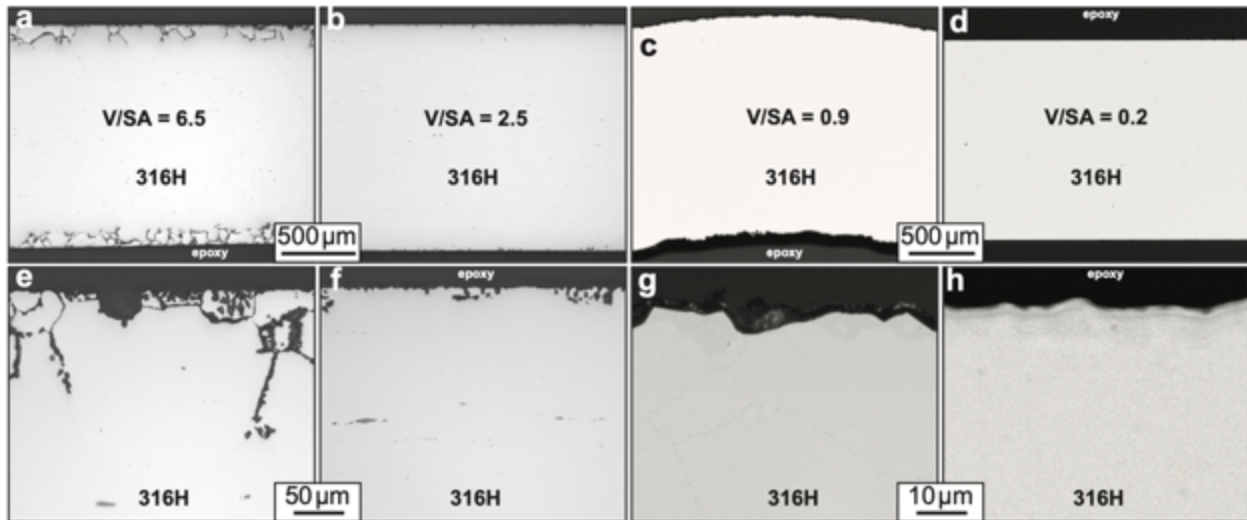


Figure 3-3. Light microscopy of polished sections of representative specimens (a,e) $V/SA = 6.5$, (b,f) $V/SA = 2.5$, (c,g) $V/SA = 0.9$ and (d,h) $V/SA = 0.2$.

To quantify the chemical attack observed under these conditions, Figure 3-4 shows SEM EDS maps from a polished cross-section from one of the $V/SA=6.5$ specimens. As expected, Figure 3-4b shows Cr depletion at the surface and associated void formation deeper in the specimen (dark areas in the SEM image, Figure 3-4a). In the depleted areas, Ni and Mo enrichment were observed, Figures 3-4e and 3-4f, because of Fe and Cr dissolution. The maps are indicating Mo, Cr and Ni enrichment in the epoxy which is not accurate. To better quantify the depletion in the alloy substrate, Figure 3-5a shows an EDS line profile from a similar region of this specimen. The line profile shows a non-uniform depletion of Cr and Mn in the outer region of the specimen with Ni and Mo enrichment. The other profiles in Figure 3-5 show similar trends but with less affected metal. In Figure 3-5b, a relatively uniform depleted region was observed to a depth of $15\ \mu\text{m}$ for a $V/SA=2.5$ specimen. For the $V/SA=0.9$ specimen shown in Figure 3-5c, the surface depletion was $<10\ \mu\text{m}$ but a second depleted grain boundary was profiled deeper in the specimen. Finally, in Figure 3-5d for the $V/SA=0.2$, the amount of Cr depletion was limited to a depth of $\sim 5\ \mu\text{m}$. A thin Cr-rich reaction product may have formed on this specimen resulting in a small mass gain, Table 3-2. The mass gain could be due to C, N or O uptake in this reaction product, which are difficult to detect by SEM/EDS, especially in a thin film.

Based on the light microscopy images, an assessment was made of the depth of attack (Figure 3-6). Not all of the low V/SA specimens were sectioned because the mass gains were very similar, shown in Table 3.2. In general, there was a decreasing trend in the observed depth of attack with decreasing V/SA . Similar to the mass change data in Table 3-2, there was a large amount of scatter for the $V/SA=6.5$ specimens. The deeper attack for high V/SA was along grain boundaries so microstructure (e.g. alloy grain size) could be a parameter affecting the attack [Muránsky 2019, Feng 2022].

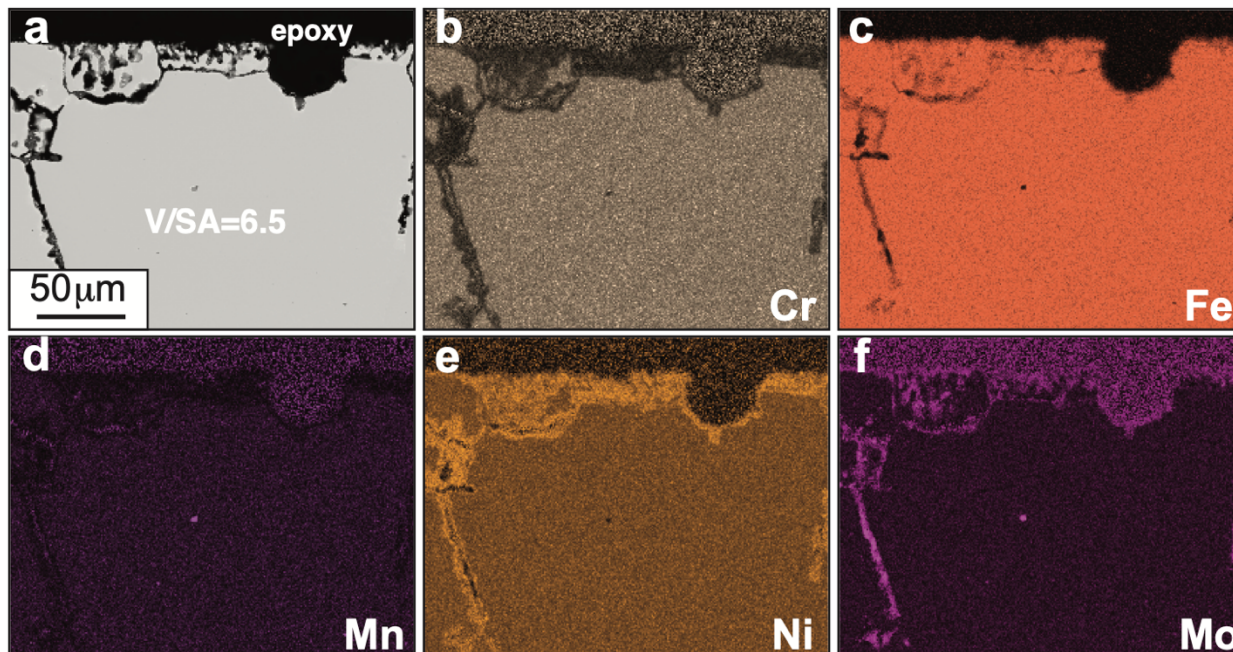


Figure 3-4. (a) SEM backscattered electron image of a polished section of the 316H specimen exposed for 500 h at 700°C in static NaCl-MgCl₂ salt V/SA=6.5, (b-f) associated EDS maps of (a).

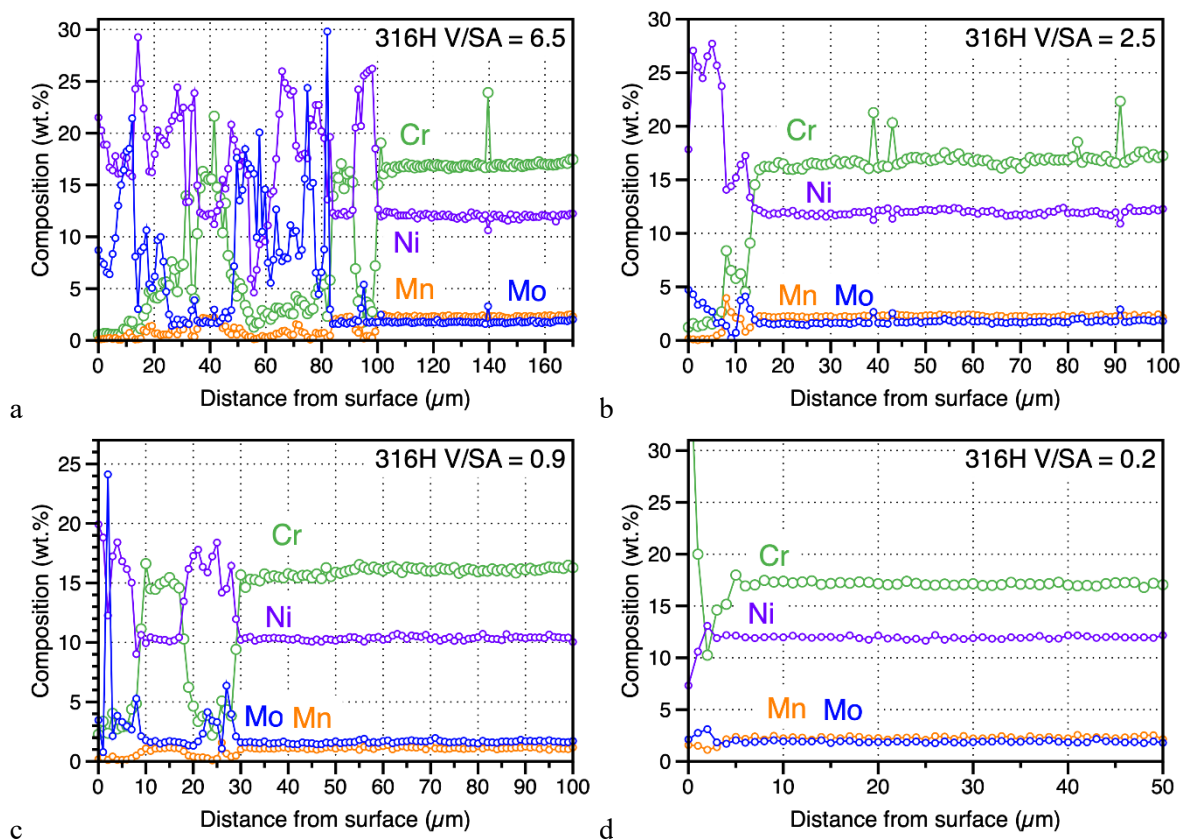


Figure 3-5. EDS line scans from 316H specimens exposed for 500 h at 700°C in purified NaCl-MgCl₂ salt (a) V/SA = 6.5, (b) V/SA = 2.5, (c) V/SA = 0.9 and (d) V/SA = 0.2.

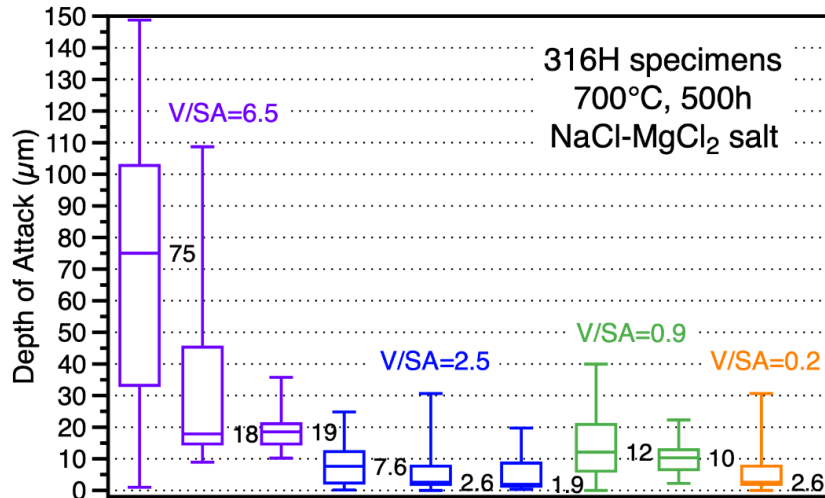


Figure 3-6. Box and whisker plots of the depth of attack based on the light microscopy images of selected specimens. The median values are shown and the boxes are defined by the 25% and 75% values. The whiskers show the minimum and maximum values measured.

3.3 DISCUSSION

One of the key issues here is whether the use of Mo capsules affects these results, perhaps accelerating the mass loss because of a reaction with Fe or Ni or a galvanic effect [Olson 2015, Guo 2018, Ding 2019]. A monometallic experiment, i.e., 316H in a 316H container, is the most ideal experiment to eliminate any dissimilar material effects. It may also be the most realistic for the application depending on the geometry and the actual V/SA in the application. However, a monometallic capsule experiment results in a very low V/SA value and very little mass change, Table 3-2. Therefore, it can make it difficult to compare numerous candidate materials, particularly materials not available in tube or sheet form to fabricate a capsule/container. The issue of capsule material selection is further discussed in the next section of this report where different capsule materials are compared with Cl and F salts. The 0.2 mg/cm² mass loss for a Mo coupon in a Mo capsule and associated ~0.5µm surface pits were surprising given the expected inertness of Mo to the salt. A more dedicated study would be needed to assess the salt compatibility of Mo to see if the reaction were reproducible and how the Mo starting surface microstructure compared to that observed after salt exposure. If a truly inert container could be identified, this experiment could be repeated to eliminate this issue.

In terms of optimizing the experiment, the small 316H specimen in a Mo capsule resulted in the most mass loss but also the most scatter in the results, Table 3-2. This may be due to the stochastic nature of the attack, especially where the reaction is concentrated on a relatively small surface area with varying depths of attack which is dependent on the specimen microstructure of each specimen exposed, Figures 3-3a, 3-4 and 3-6. Thus, it may not be optimal in this case to use the largest V/SA ratio. The very small mass gain for the 316H specimens in a 316H capsule may reflect a small Cr-rich reaction product forming at the surface as suggested by the line profile in Figure 3-5d. A 0.1 mg/cm² mass gain would correspond to a 0.6 µm oxide, or possibly a mixed O-C layer.

Previously, a number of combinations of salt, materials and temperature have been conducted in monometallic and Mo capsules tests. Figure 3-7 summarizes those results, typically for 500 or 1000 h exposures at 550°-700°C with purified NaCl-MgCl₂ or FLiNaK salt [Sulejmanovic 2021]. Most of the results are for 316H specimens but two data sets are for Hastelloy N (Table 3-1) at 700°C with Mo and

Hastelloy N capsules. As a function of temperature, the results are very limited with most of the studies conducted at 700°C. Figure 3-8 tries to summarize the effect of temperature on the slopes shown in Figure 3-7. There is significant scatter in the results at 700°C and not enough data points to develop a reliable temperature effect based on this information. Perhaps further study could determine an optimal V/SA ratio but the issue of dissimilar interactions between the specimen and container would still need to be resolved.

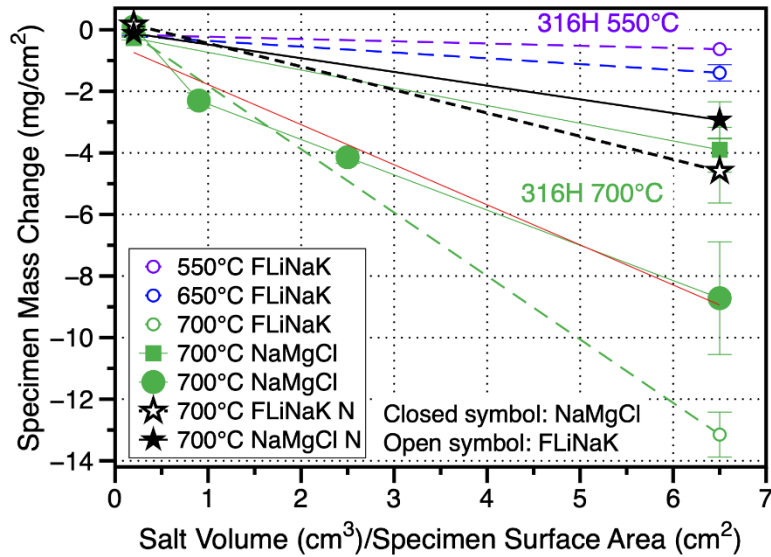


Figure 3-7. Specimen mass loss for 316H and Hastelloy N specimens exposed to Cl and F salts at 550°-700°C. In prior work, only the extreme values for V/SA were evaluated with small specimens in Mo or 316H/Hastelloy N capsules.

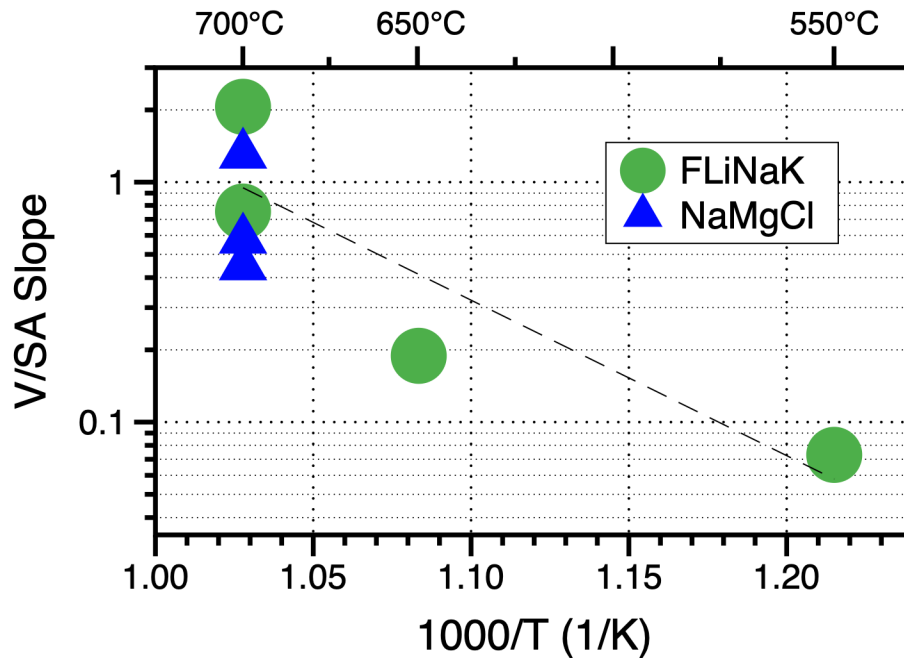
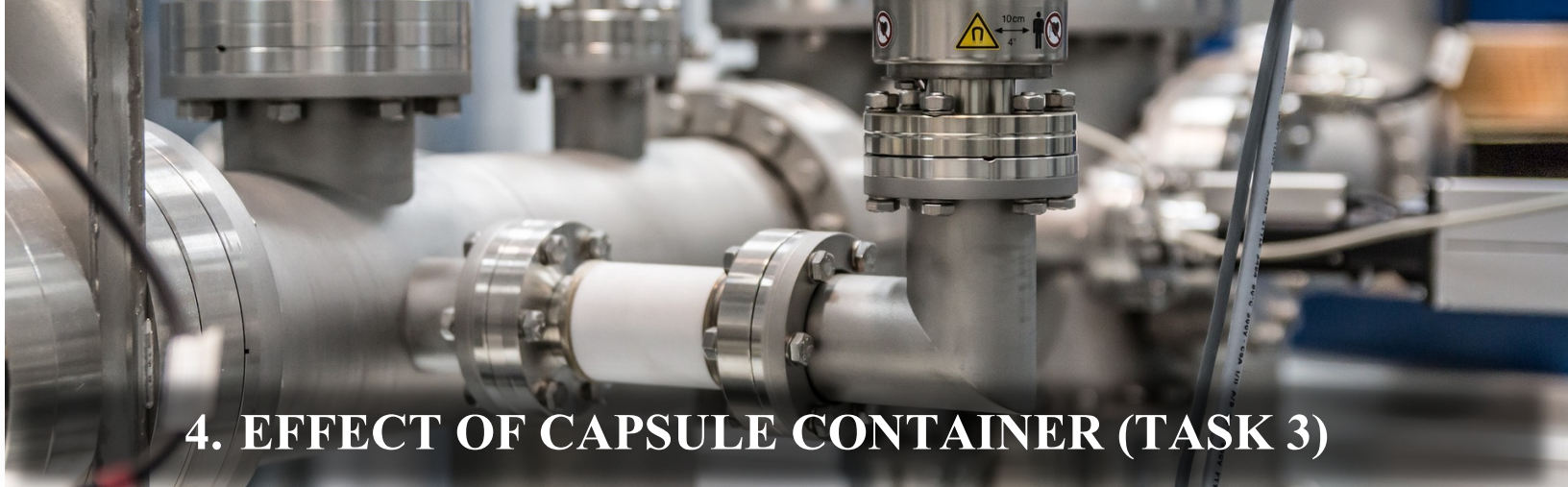


Figure 3-8. Arrhenius plot of V/SA over specimen mass change slopes from Figure 3-7.

3.4 SUMMARY

A set of capsule experiments was conducted in triplicate to quantify the effect of changing the ratio of molten salt volume to sample surface area using 316H specimens in NaCl-MgCl₂ salt at 700°C for 500 h. By changing the capsule material and the specimen size, decreasing the V/SA ratio resulted in a decreased mass loss which corresponded with decreased depth of attack and Cr loss in the steel substrates. This illustrates the importance of this parameter. In comparing diverse molten salt compatibility data sets, this ratio should be calculated as a qualitative normalizing strategy. However, the current data set is too limited to capture other parameters such as the effect of temperature on this ratio. It is not possible to define an optimal ratio for this type of experiment but very small ratios lead to minimal mass change and large ratios lead to large scatter in the mass change and depth of attack.



4. EFFECT OF CAPSULE CONTAINER (TASK 3)

4.1 EXPERIMENTAL PROCEDURE

Isothermal capsule testing was conducted on the four alloys with the measured compositions shown in Table 3-1. The alloy 709 [Kikuchi 1985] and 617 [Wright 2014] alloy heats are the same ones used for the DOE ASME Boiler & Pressure Vessel code case work. As described in the previous section, the specimens were $\sim 6 \times 12 \times 1.5$ mm coupons polished to a 600 grit finish. The salt exposures were conducted in inner capsules (25 mm outer diameter x 100 mm tall x 1.2mm wall) made of 316H, low carbon arc cast Mo, Ni 200, or Hastelloy N, Figure 3-1. Or alternatively BN or graphite crucibles were placed inside 316H inner capsules that were then welded shut as welding or sealing was not possible with the BN or graphite crucibles.

The NaCl-MgCl₂ salt was made from reagent-grade salts and purified using a two-step process [Young 1993, Chen 1993, Mayes 2018, Kurley 2019]: as described in the previous section (#3). The FLiNaK salt was purchased from Materion and was not further purified. The as-received salt was analyzed, and the results are summarized in Table 4-1 and compared to several other batches of FLiNaK salt [Sulejmanovic 2021] used in section #5. In general, the metallic impurities were low, but the O₂ level was higher, and variable compared to commercial salt purified by hydro-fluorination [Kelleher 2015] that also contained a Zr addition.

Similar to section #3, capsules were loaded with ~ 30 g of Cl salt or ~ 32 g of FLiNaK salt in an Ar-filled glove box with impurity levels ≤ 1 ppm O₂ and H₂O. The BN and graphite crucibles held ~ 22 g of Cl salt or ~ 23 g of FLiNaK. For some of the capsules, ~ 13 mg of Mg powder was added as a redox addition [Olander 2002, Zhang 2018, Pint 2019]. The specimens were cleaned prior to exposure using deionized water, acetone and methanol. For the capsule experiments, the specimens were attached to one end of the capsule using Mo or 316L wire. For the BN and graphite experiments, a rod was inserted in the specimens to keep them upright and fully exposed to salt during the experiment, Figure 4-1. After loading the salt, the inner capsules were sealed inside the glove box using gas tungsten arc welding. The inner capsules were then placed inside type 304 stainless steel outer capsules and sealed using electron beam welding to provide secondary containment and prevent the primary capsule from oxidizing during the isothermal exposure.

The capsules were exposed in a box furnace in laboratory air for 500 h at 700°C. After exposure, the capsules were inverted to allow the salt to drain away from the specimen [Vreeland 1953] and the capsules were then opened in the same glove box. After exposure, the specimens were ultrasonically

Table 4-1. Salt impurities (in ppmw) determined by combustion analysis (O,H) and inductively coupled plasma-mass spectroscopy

	O	H	Cr	Mn	Fe	Ni	Zr
Materion #1	1460±744	38	1.1	0.6	9.8	0.7	0.4
Materion #2	2087±874	12	–	–	–	–	–
Comm. FLiNaK	372±67	7	7.1	1.0	16	6.5	314
Laboratory FLiNaK	–	–	13	6.1	61	195	0.2

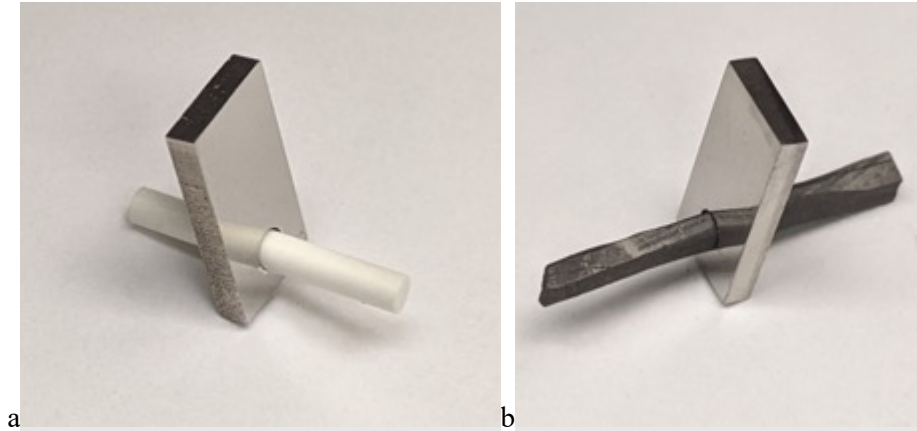


Figure 4-1. Images of polished 316H specimens with (a) BN rod or (b) graphite rod to hold the specimen upright in the salt.

cleaned using deionized water at 40°C. Before and after exposure, the specimens were weighed using a Mettler Toledo model XP205 balance with an accuracy of ±0.04 mg. The same characterization procedure described in section #3 was used for these specimens with the addition of ICP-OES to analyze the salt after exposure for Cr, Fe, Ni and Mn content.

4.2 RESULTS

All of the experiments were conducted in triplicate to determine reproducibility. For the NaCl-MgCl₂ experiments, the mass change results are summarized in Figure 4-2. Some of the changes may be explained by variations in the V/SA ratio (shown in Figure 4-2) as described in section #3. However, even accounting for changes in the V/SA ratio, the container material clearly had a strong impact on the mass change results. In order to compare the exposed specimens, low magnification images are shown in Figure 4-3. The differences in the amount of attack reflect the higher mass losses using Mo and Ni

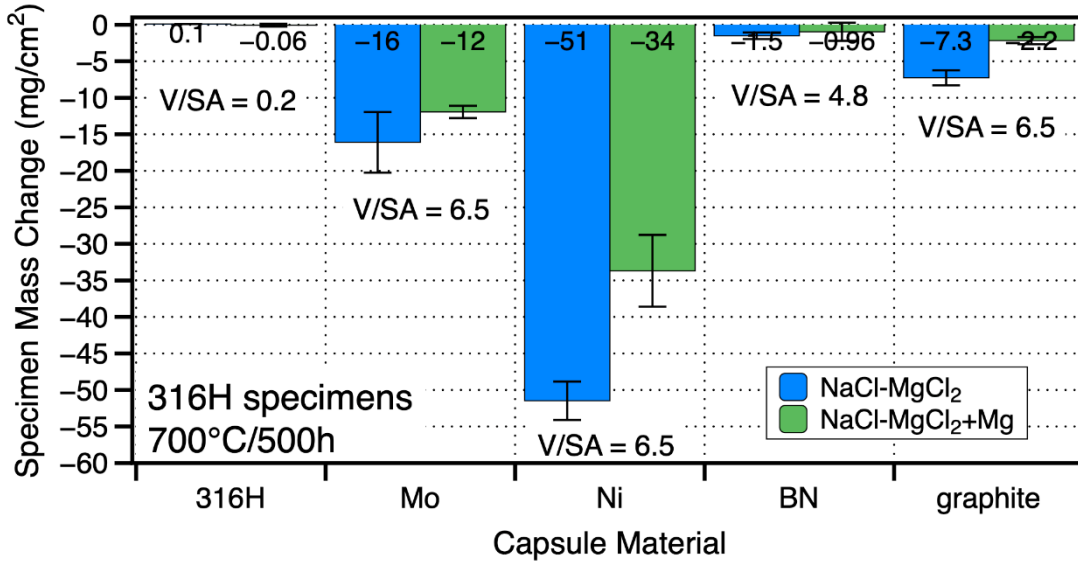


Figure 4-2. Specimen mass loss for 316H specimens in 5 different container materials after 500 h at 700°C in purified NaCl-MgCl₂ with and without a Mg addition.

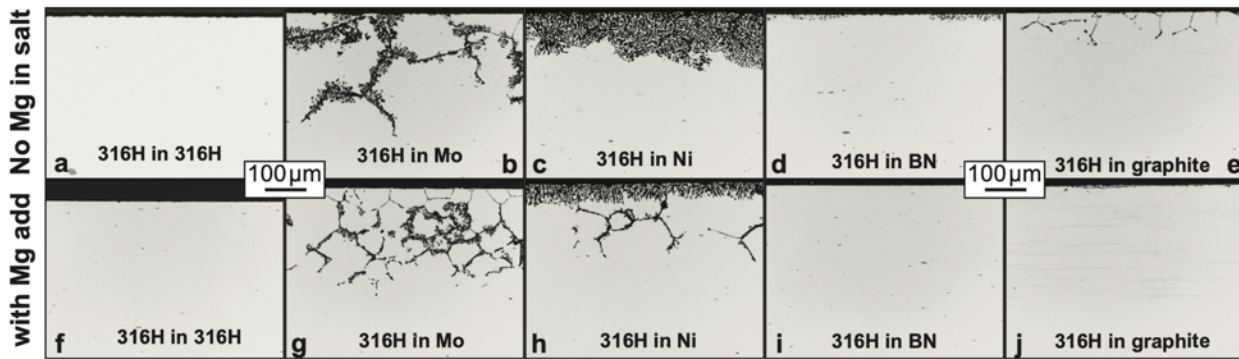


Figure 4-3. Light microscopy of polished sections of representative 316H specimens exposed for 500 h at 700°C in (a-e) NaCl-MgCl₂ and (f-j) NaCl-MgCl₂ with Mg; (a,f) 316H capsule, (b,g) Mo capsule, (c,h) Ni capsule, (d,i) BN container and (e,j) graphite container.

capsules and the smaller losses with 316H, BN and graphite shown in Figure 4-2. (The attack in Figures 4-3b and 4-3g indicate a different alloy grain size that appears to be a variation in these two locations.) Figure 4-4 summarizes the observed depth of attack measurements on various specimens for comparison. Similar attack with deep void penetrations has been observed in most studies of alloys exposed to halide salts [Koger 1973, Olson 2015, Zheng 2016, Sun 2018, Raiman 2018, Ding 2019, Pint 2019, Raiman 2019, Kurlay 2019, Sulejmanovic 2021]. Box and whisker plots are used to show the distribution of measured values as the attack is not uniform. Very little visible attack was observed for the tests in 316H capsules and BN with the Mg addition.

Figures 4-5 to 4-19 show EDS maps and line profiles to further quantify the different observations in NaCl-MgCl₂ salt. Figure 4-5 shows the limited attack observed with a 316H

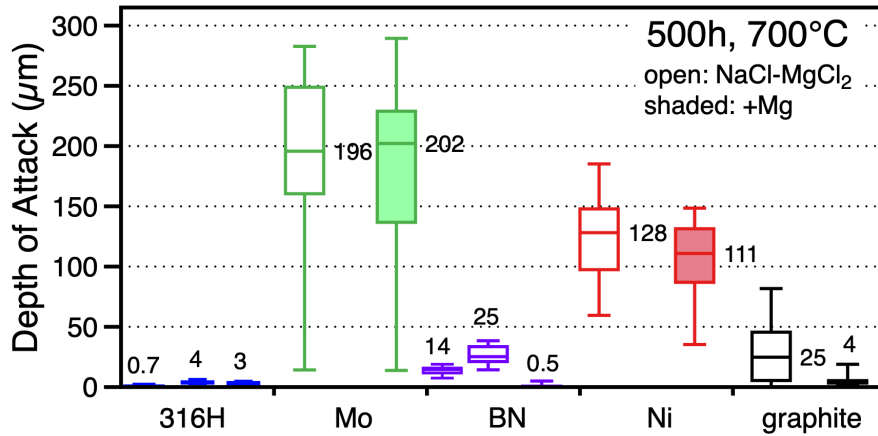


Figure 4-4. Box and whisker plots of the depth of attack based on the light microscopy images of selected specimens exposed to NaCl-MgCl₂ salt with and without Mg additions. The median values are shown and the boxes are defined by the 25% and 75% values. The whiskers show the minimum and maximum values measured.

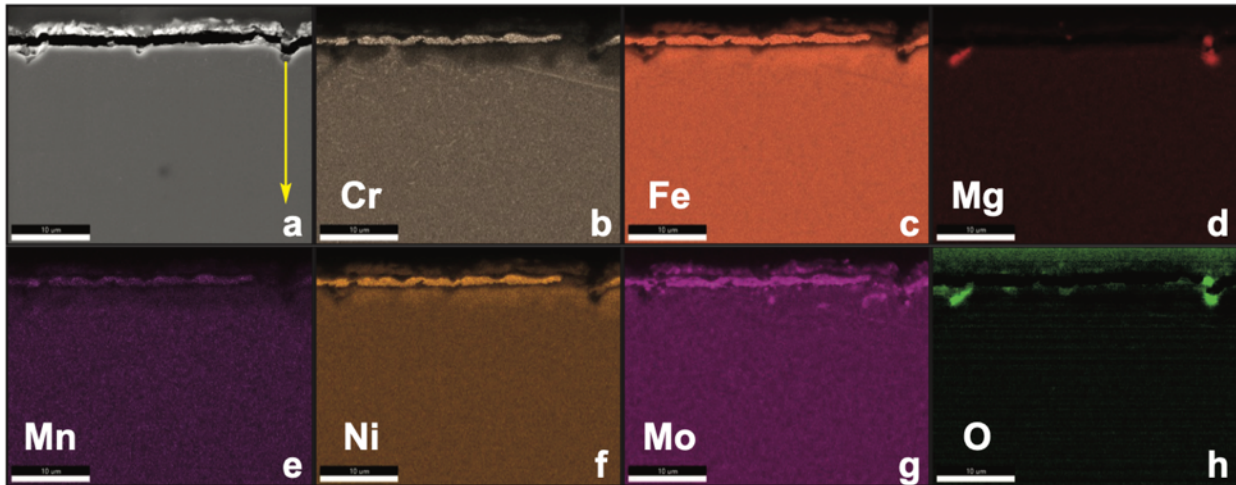


Figure 4-5. (a) SEM image of a polished cross-section of a 316H specimen exposed for 500 h at 700°C to NaCl-MgCl₂ salt with a Mg addition in a 316H capsule and (b-h) EDS maps of the same region.

specimen in a 316H capsule with a Mg addition. From the maps, there appears to be a reaction layer at the surface but this could be polishing debris in the gap between the specimen and epoxy in the mount. The surface Cr depletion is limited to <5 µm, Figure 4-6, which is consistent with the small mass losses observed, averaging 0.06 mg/cm². Characterization of 316H in a 316H capsule without Mg were shown in the previous section.

Figure 4-7 shows the salt chemistry after the test. Despite the small specimen mass change, a large Cr and Mn content was measured after the test because the capsule also was reacting with the salt.

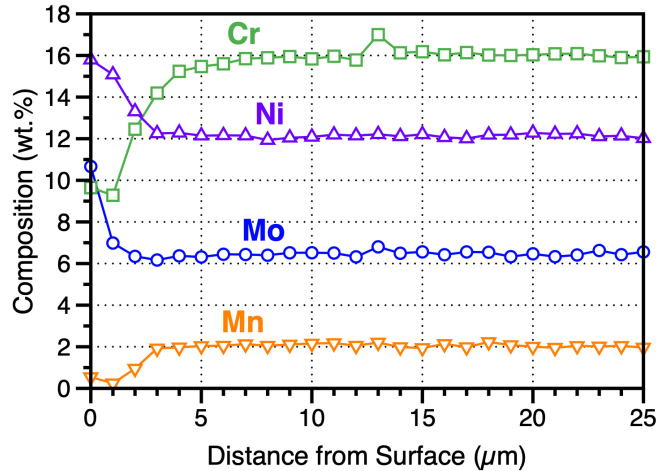


Figure 4-6. EDS profile from the line shown in Figure 4-5a from a 316H specimen exposed for 500 h at 700°C to NaCl-MgCl₂ salt with a Mg addition exposed in a 316H capsule.

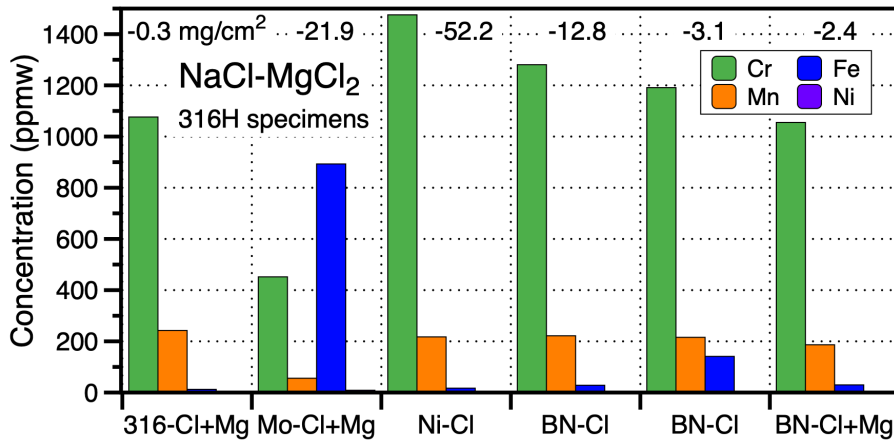


Figure 4-7. Post-test metallic salt impurities measured by ICP-OES in the NaCl-MgCl₂ salt with and without Mg in the various capsule experiments. The BN crucible results are from an initial set of experiments that were repeated because of the variability observed.

Figure 4-8 shows much more dramatic attack when a Mo capsule was used. The maps show strong Cr, Fe and Mn depletion along alloy grain boundaries. The line profile (location shown in Figure 4-8a) confirms this with limited depletion in the grains, Figure 4-9. In addition to increased Ni and Mo contents, a strong O signal was observed in the dark regions (Fig. 4-8h) which may reflect oxidized salt that was not removed during cleaning as Mg also was detected in these regions, Figure 4-8d. This was a second group of three experiments (average -16 mg/cm²) compared to a similar set of capsules shown in Figure 3.4 where the average mass loss was -8.7 mg/cm². Figure 3.4 does not show such significant Cr and Fe depletion at grain boundaries or Mg and O on the grain boundaries. In Figure 4-7, Cr, Fe and Mn all were detected in the salt. When the specimen surface becomes depleted in Cr and Mn, it is expected that Fe will then dissolve into the salt. However, it would be useful to repeat and confirm this result because it is very different from the other results. Previous work with an unalloyed Fe specimen in a Mo capsule with commercial FLiNaK salt indicated significant reaction between the Mo capsule and Fe [Pint 2022a].

With a Ni capsule and Cl salt without Mg, the attack was not as concentrated on the alloy grain boundaries but reflected a deep Cr, Fe and Mn depletion in the bulk, Figures 4-10 and 4-11.

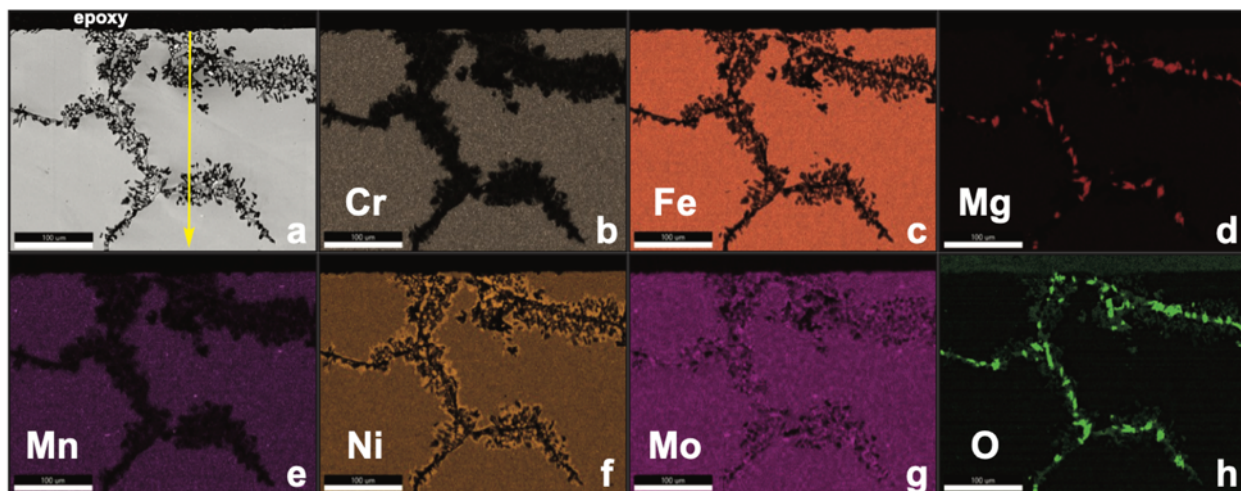


Figure 4-8. (a) SEM image of a polished cross-section of a 316H specimen exposed for 500 h at 700°C to NaCl-MgCl₂ salt in a Mo capsule and (b-h) EDS maps of the same region.

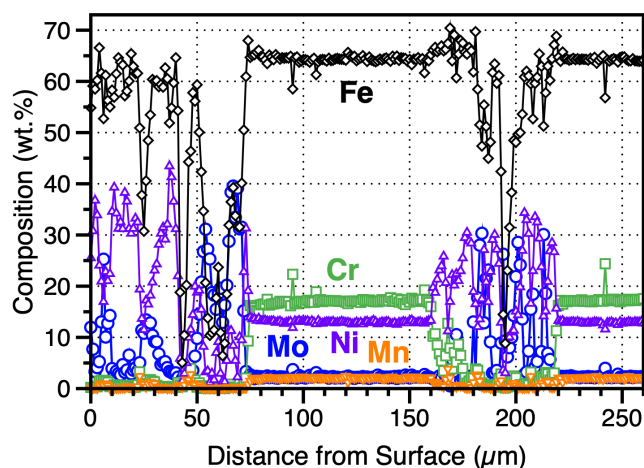


Figure 4-9. EDS profile from the line shown in Figure 4-8a from a 316H specimen exposed for 500 h at 700°C to NaCl-MgCl₂ salt in a Mo capsule.

With a Ni capsule, the measured depth of attack (Figure 4-4) was less but the mass loss was much higher (Figure 4-2). The salt in this case had the highest Cr content, which is contrary to the expectation that Cr in the salt would react with the Ni capsule. Profiles from the Ni capsule are shown in Figure 4-12. Only a small amount of Cr was found in the capsule but a large amount of Fe was found, which is consistent with the low Fe content in the salt.

In contrast to Figures 4-9 and 4-10 in salt without a Mg addition, the attack was less severe and more concentrated on alloy grain boundaries for a Ni capsule with a Mg addition to the salt, Figures 4-13 and 4-14. Similar to Figure 4-9, there was very little Cr depletion within the grains but very significant attack at grain boundaries deep in the specimen. Salt chemistry was not measured after this experiment but the Ni capsule showed much less Fe and more Cr had diffused into the wall, Figure 4-12.

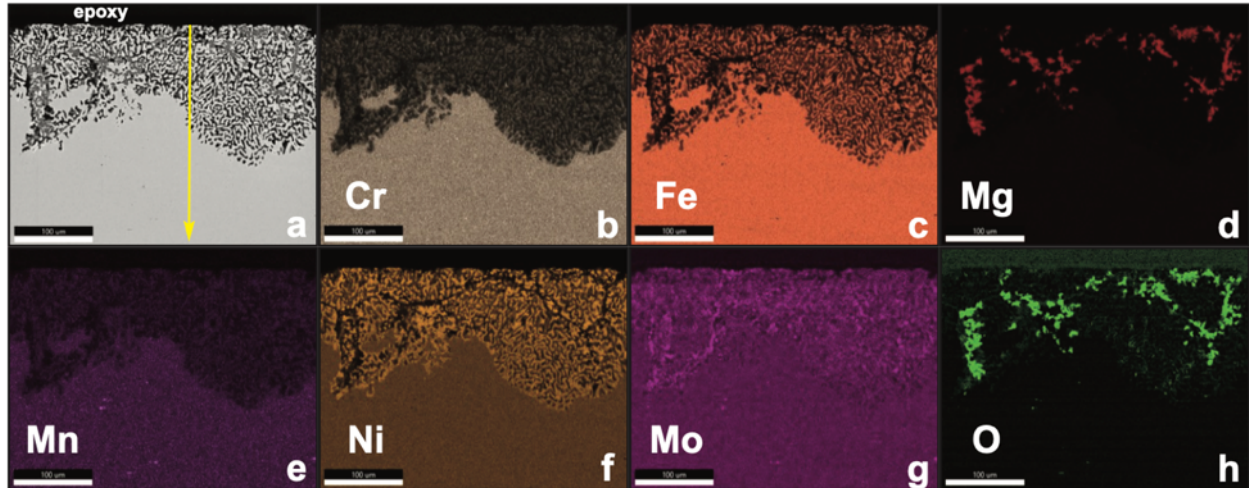


Figure 4-10. (a) SEM image of a polished cross-section of a 316H specimen exposed for 500 h at 700°C to NaCl-MgCl₂ salt in a Ni capsule and (b-h) EDS maps of the same region.

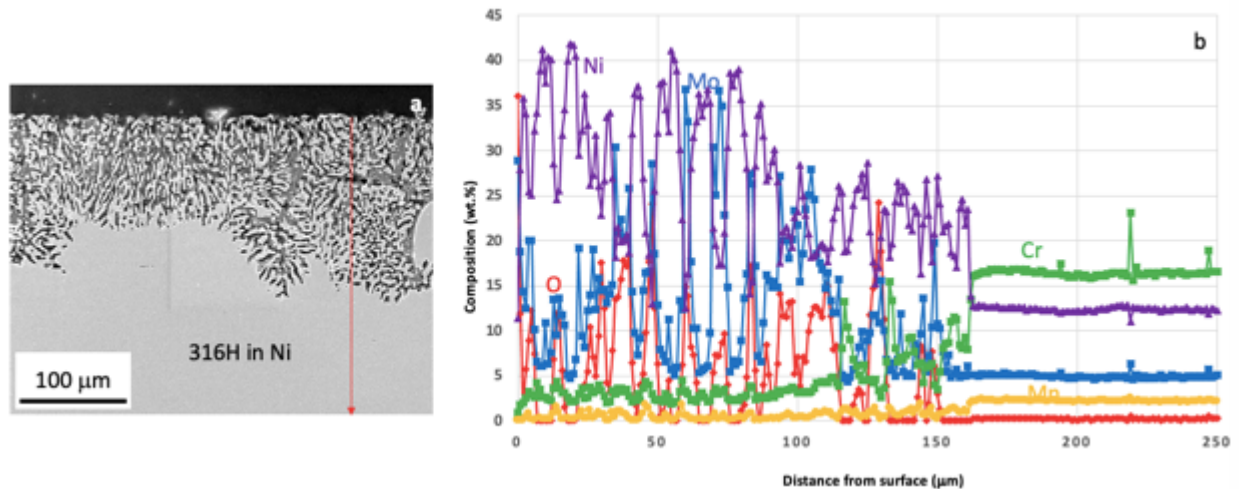


Figure 4-11. (a) SEM image of a polished cross-section of a 316H specimen exposed for 500 h at 700°C to NaCl-MgCl₂ salt in a Ni capsule and (b) EDS profile from the line shown in (a).

Figure 4-15 shows the limited attack observed when the experiment was performed in a BN crucible. The depth of attack was ~20 µm based on the EDS line profile where the Cr is highly depleted in this region, Figure 4-16. The first experiments conducted with a BN crucible used a SS wire to hold the specimens upright and were repeated. Figure 4-17 shows EDS characterization that found evidence of a N-rich phase in that first set of experiments, Figure 4-17c. Subsequent XRD analysis identified a Mo₃Fe₃N phase in specimens exposed to salt with and without Mg. However, the Mo map in Figure 4-17g does not show correspondence with the N map. The experiments also were repeated because MgO was observed on the steel surface, Figures 4-17d and 17h. When the experiments were repeated (data shown in Figures

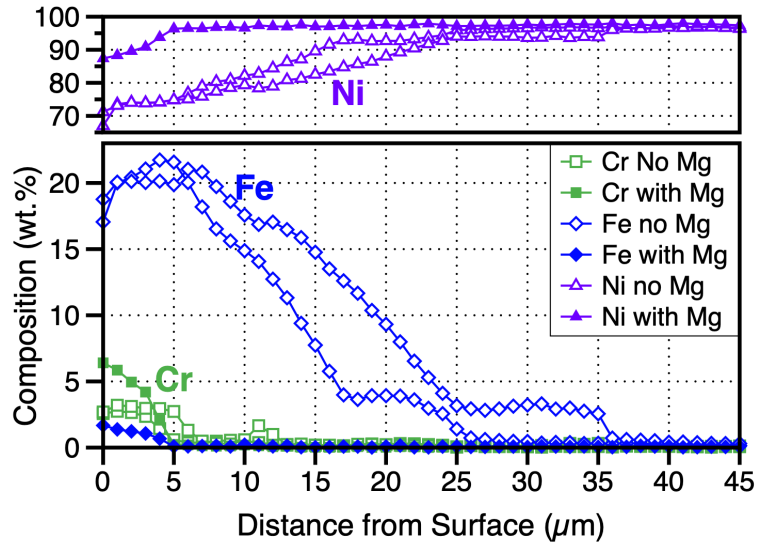


Figure 4-12. EDS line profiles from the Ni capsule after exposure of a 316H specimen for 500 h at 700°C to NaCl-MgCl₂ salt with and without a Mg addition in the salt.

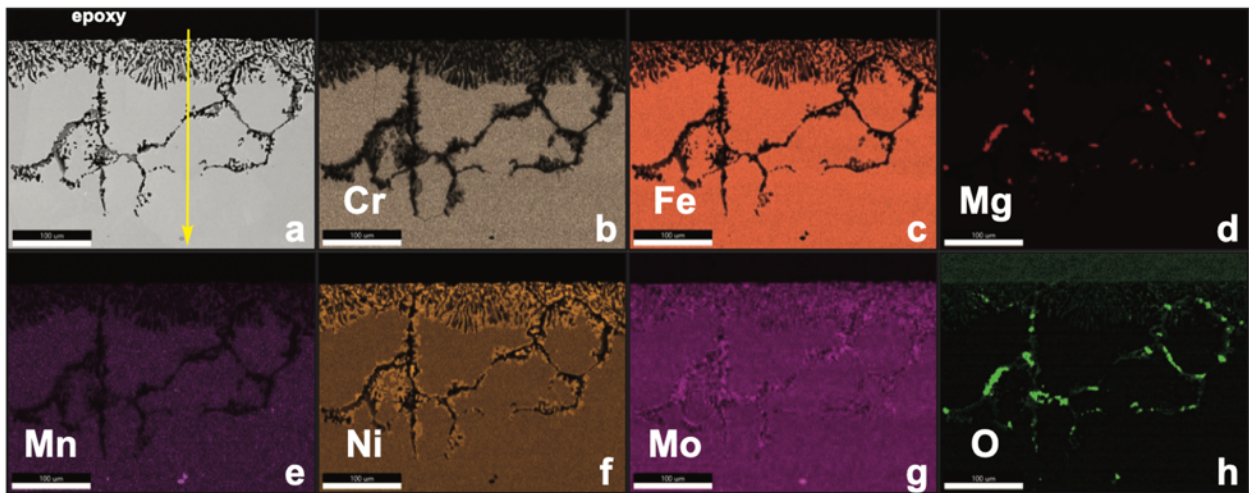


Figure 4-13. (a) SEM image of a polished cross-section of a 316H specimen exposed for 500 h at 700°C to NaCl-MgCl₂ salt with a Mg addition in a Ni capsule and (b-h) EDS maps of the same region.

4-2, 4-3 and 4-4), there was not clear evidence of nitride formation. Nevertheless, it is a possible concern with a BN container that a reaction could occur and BN might not be as inert as proposed [Olson 2015]. The salt analysis from BN crucibles in Figure 4-7 is from the first set of BN capsules where the mass losses were higher and more variable. Compared to the salt exposure in a 316H capsule, the Cr and Mn levels were similar in the BN crucibles. Two BN crucibles without Mg additions were examined because of the large scatter in mass change results. Some differences in the post-test salt Fe content were noted but the Cr and Mn levels were very similar in each case.

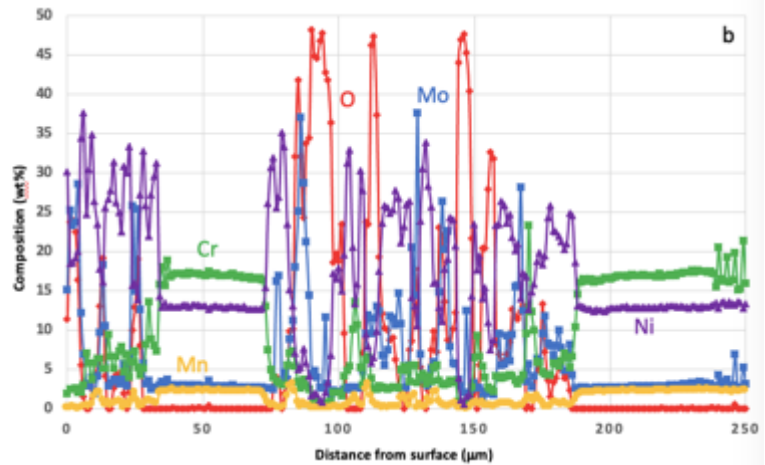
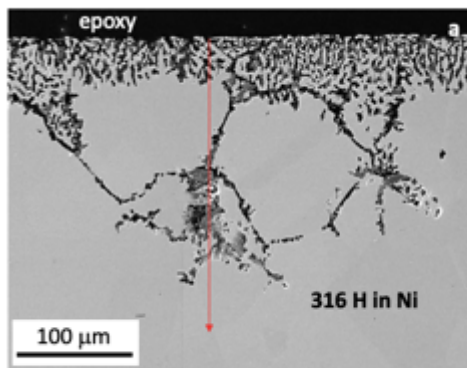


Figure 4-14. (a) SEM image of a polished cross-section of a 316H specimen exposed for 500 h at 700°C to NaCl-MgCl₂ salt with a Mg addition in a Ni capsule and (b) EDS profile from the line shown in (a).

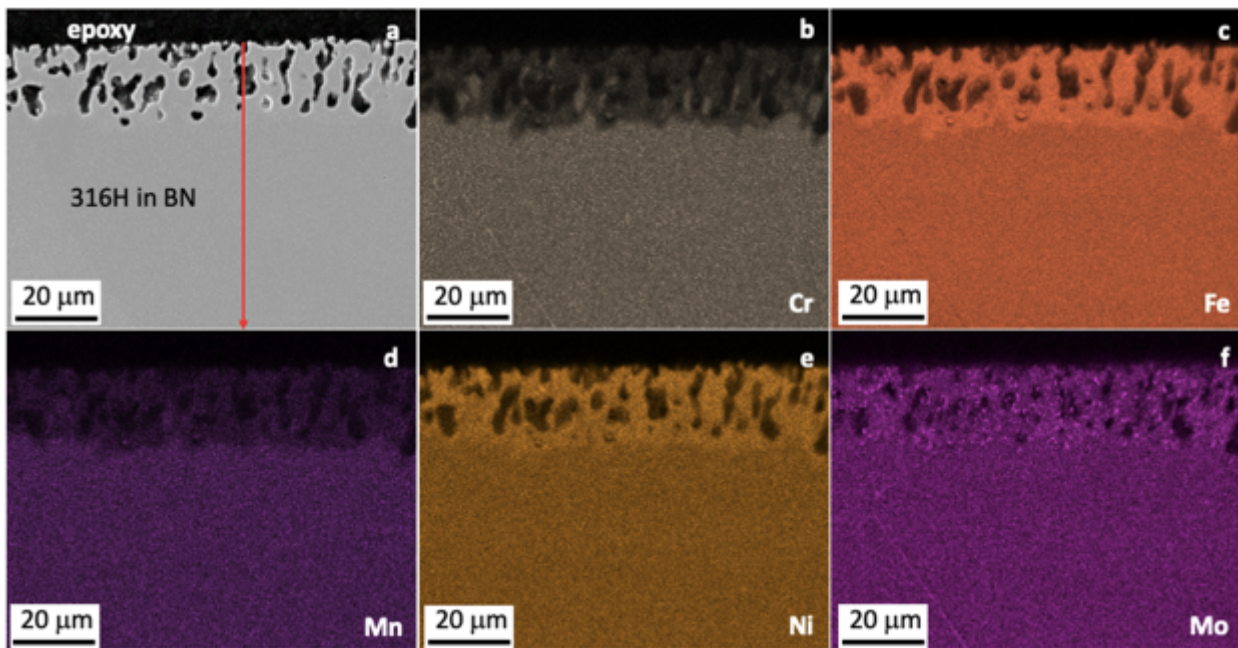


Figure 4-15. (a) SEM image of a polished cross-section of a 316H specimen exposed for 500 h at 700°C to NaCl-MgCl₂ salt in a BN container and (b-f) EDS maps of the same region.

Finally, when the experiment was conducted in a graphite crucible, the attack was concentrated on the alloy grain boundaries without Mg, Figures 4-18 and 4-19. Similar to other cases, the boundaries were severely Cr depleted and enriched in Ni while the grain interiors were not strongly affected. Very little attack was observed when Mg was added to the salt, Figure 4-3j, and the specimen was not further characterized. Unfortunately, salt samples were not retained to measure the post-test salt chemistry. The effect of a graphite crucible on FLiNaK salt chemistry will be discussed in the next section.

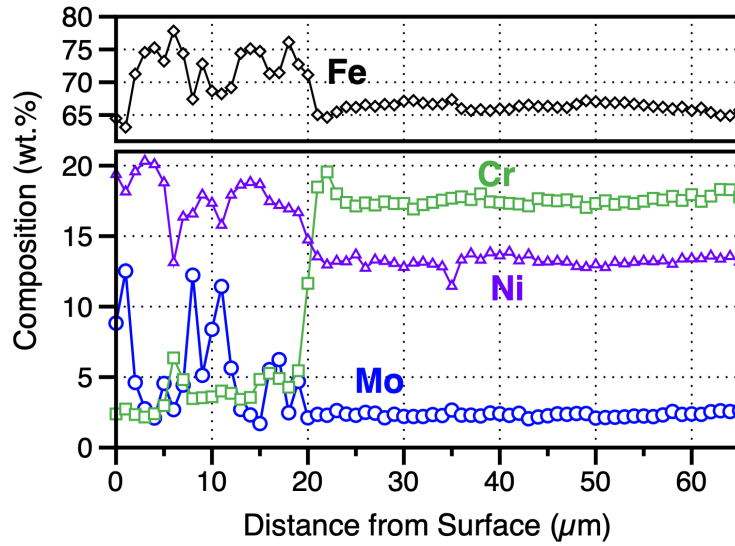


Figure 4-16. EDS profile from the line shown in Figure 4-15a of a 316H specimen exposed for 500 h at 700°C to NaCl-MgCl₂ salt in a BN container.

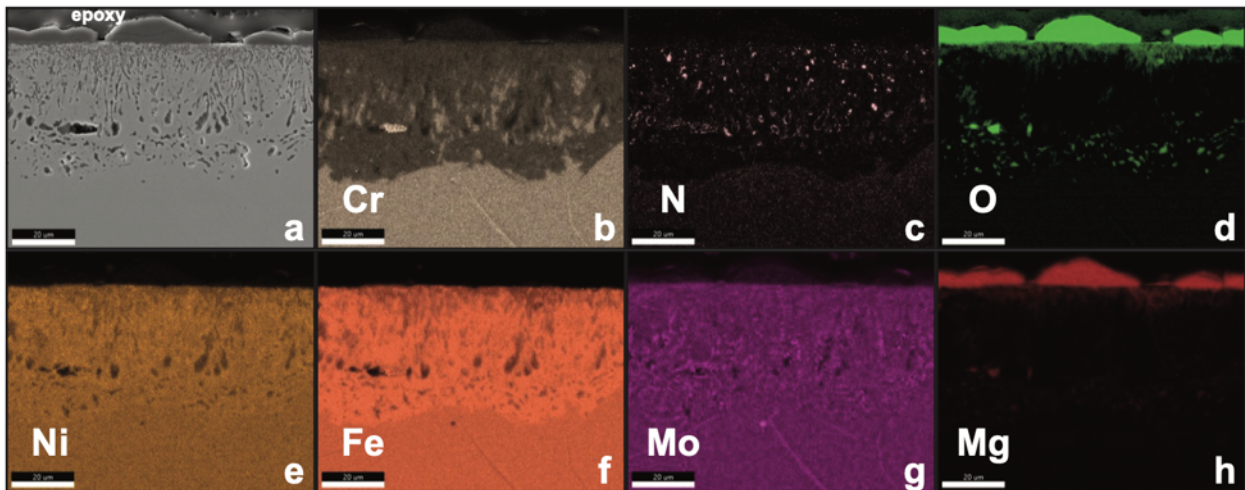


Figure 4-17. (a) SEM image of a polished cross-section of a 316H specimen exposed for 500 h at 700°C to NaCl-MgCl₂ salt with a Mg addition in a BN container and (b-h) EDS maps of the same region. This experiment was repeated and nitride formation was not detected.

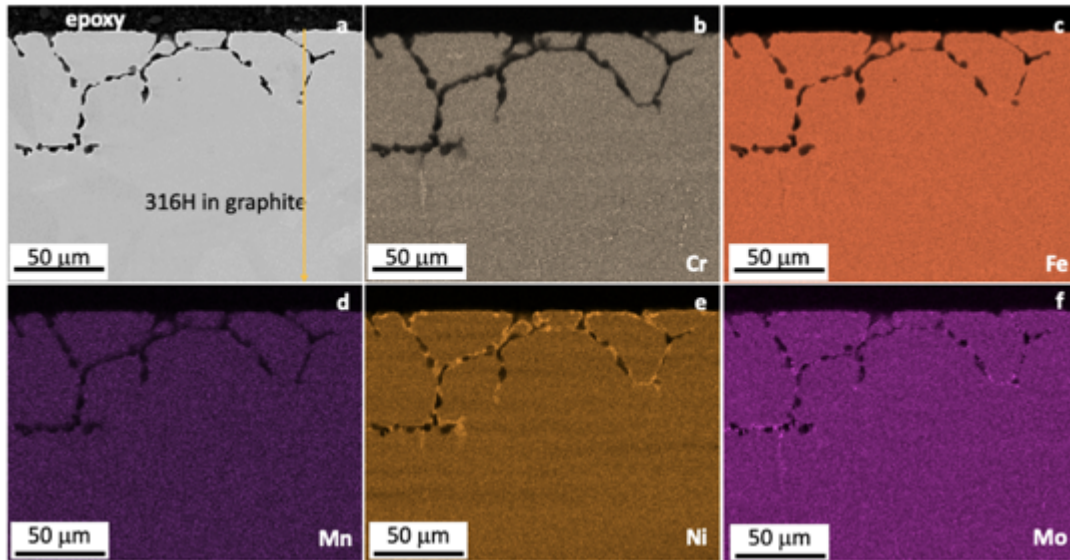


Figure 4-18. (a) SEM image of a polished cross-section of a 316H specimen exposed for 500 h at 700°C to NaCl-MgCl₂ salt in a graphite container and (b-f) EDS maps of the same region.

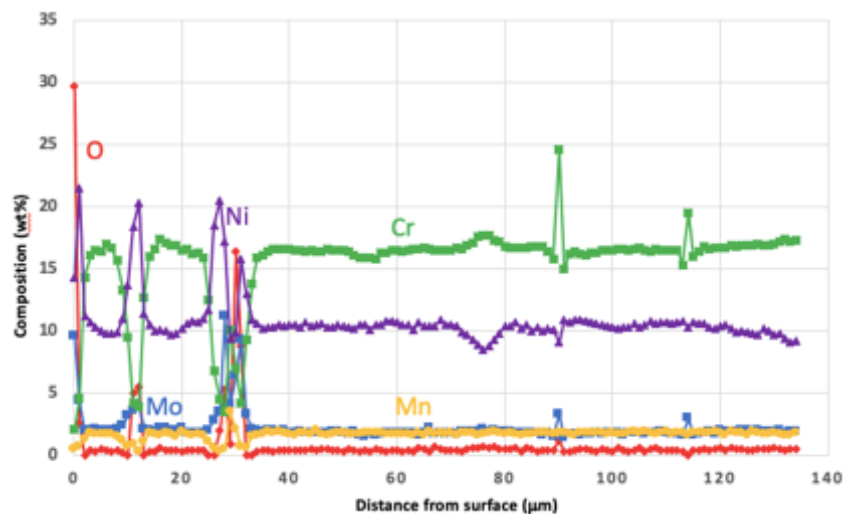


Figure 4-19. EDS profile from the line shown in Figure 4-18a of a 316H specimen exposed for 500 h at 700°C to NaCl-MgCl₂ salt in a graphite container.

4.3 FLiNaK RESULTS

Figure 4-20 summarizes the mass change results for the Fe-based specimens exposed to dried, commercial FLiNaK salt using five different containers. Alloy 709 specimens were exposed in three conditions. This alloy is of interest because of its much higher strength compared to conventional stainless steels [Kikuchi 1985, Viswanathan 2001]. However, its higher Cr content (Table 3-1) makes it potentially less attractive in molten salt applications. Based on mass change, the attack on alloy 709 was

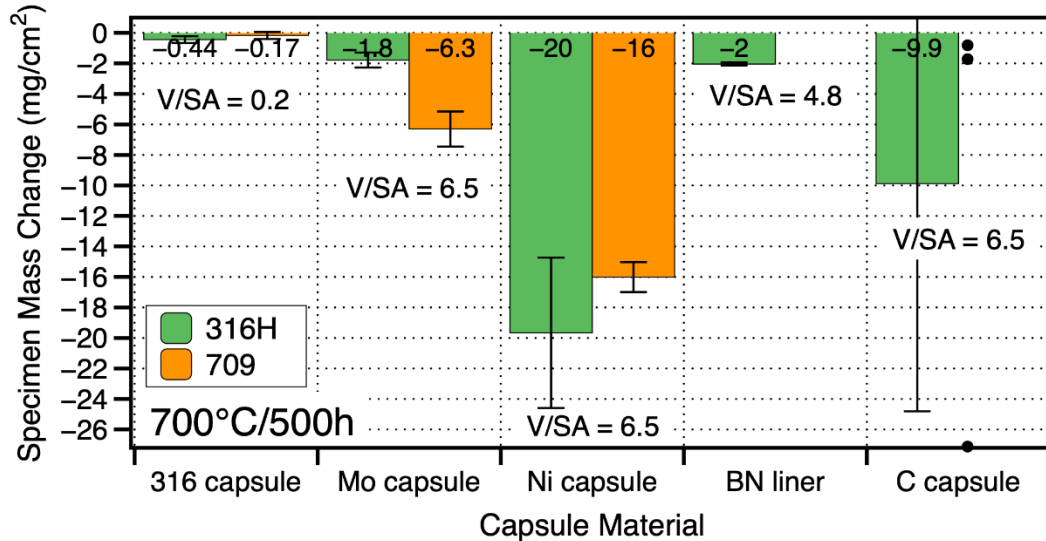


Figure 4-20. Specimen mass loss for 316H and 709 specimens in 5 different container materials after 500 h at 700°C in dried FLiNaK salt. The whiskers show the variation for three capsule experiments.

less severe except when a Mo capsule was used, which was somewhat surprising because of its higher Cr content compared to 316H. Assuming Cr is selectively attacked by the salt, one would expect the higher Cr alloy to show more mass loss associated with Cr dissolution into the salt. However, as will be shown later in this section, the higher Cr content in 709 may have led to more surface oxide formation (as a result of the high O content in the commercial FLiNaK), resulting in mass gain that would offset the mass loss due to dissolution.

Figure 4-21 shows light microscopy of representative sectioned specimens after exposure at one magnification. There is a general concern about these results because of the high O content in this FLiNaK, Table 4-1. In some cases, an oxide may have formed on the specimens, which affected the mass change. Nevertheless, the salt container strongly affected the observed results. Figure 4-22 summarizes depth of attack measurements based on images like those in Figure 4-21.

Figures 4-23 to 4-39 show EDS maps and line profiles to better understand the observations. Similar to the Cl salt experiment, the attack was limited when a 316H specimen was exposed in a 316H capsule, Figure 4-23, due to the small V/SA ratio (see Section 2). The maps indicate Fe and Ni were enriched near the surface and the Cr depletion was limited to 7-8 μm in depth in the line profile, Figure 4-24. For the alloy 709 specimen exposed in a 316H capsule, a similar minor attack was observed, Figures 4-25 and 4-26. The attack was limited such that deeper in the specimen, Cr was enriched on the alloy grain boundaries, Figure 4-25b, likely due to the formation of Cr-rich carbides on the grain boundaries. In this case, the EDS line profile suggests that a Cr-rich oxide formed on the specimen surface which may explain the smaller average mass loss for the 709 specimens, Figure 4-20.

Figure 4-27 shows post-test salt chemistry. The highest Cr levels were observed with a 316H capsule because both the specimen and capsule were reacting in a similar manner.

With Mo capsules, the depth of attack was considerably increased for 316H but the attack was primarily on grain boundaries, Figure 4-28. The line profile shown in Figure 4-28a, shows only a few locations where Cr was depleted, Figure 4-29. However, the grain boundaries were significantly depleted in both Cr, Fe and Mn such that the maps show Ni and Mo enriched at the grain boundaries, Figure 4-28. Particularly the Mo-rich grain boundaries is very different than other specimens. For the 709 specimen

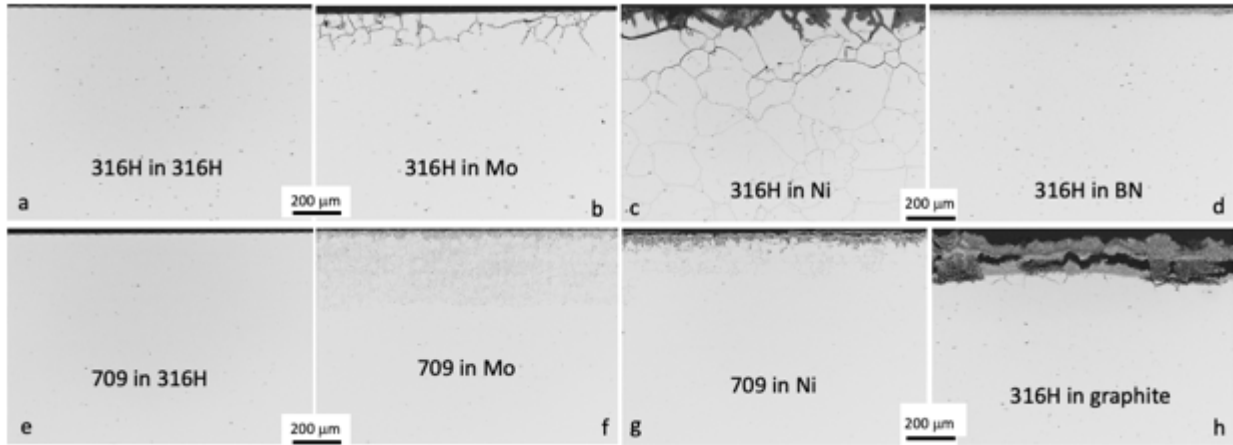


Figure 4-21. Light microscopy of polished sections of representative (a-d,h) 316H and (e-g) 709 specimens exposed for 500 h at 700°C in FLiNaK salt (a,e) 316H capsule, (b,f) Mo capsule, (c,g) Ni capsule, (d) BN container and (h) graphite container.

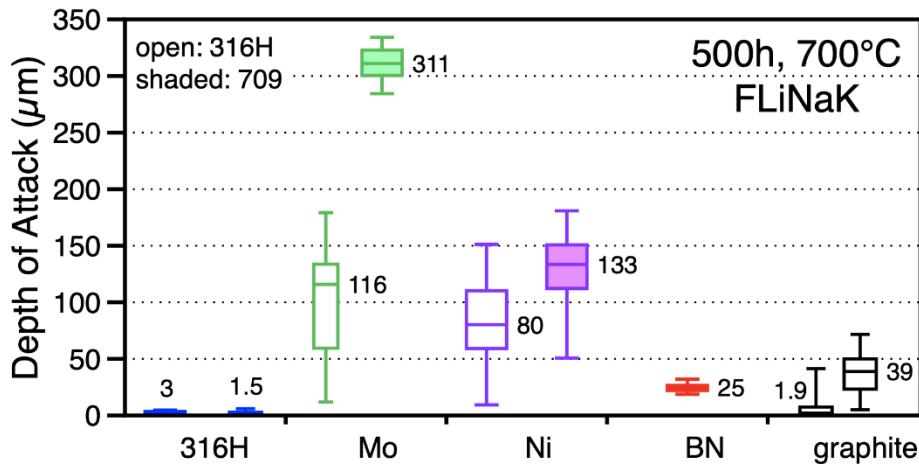


Figure 4-22. Box and whisker plots of the depth of attack based on the light microscopy images of selected specimens exposed to FLiNaK salt. The median values are shown and the boxes are defined by the 25% and 75% values. The whiskers show the minimum and maximum values measured. Two 316H specimens exposed in graphite are shown with the lowest and highest attack from Figure 4-20.

examined, the microstructure appeared to be affected much deeper, Figure 4-30. The line profile indicated a Cr depleted layer of $>30\mu\text{m}$, Figure 4-31, which is similar to the depletion in the Cr map in Figure 4-30b. Both the maps and line profiles suggest a Mo-rich oxide at the surface, which was not observed in other cases. The post-test salt chemistry in Figure 4-27 only shows results for one 316H specimen. In this case, the Cr level was lower but the ratio of Cr:Fe was higher compared to the 316H capsules. Perhaps this is because as the surface of the 316H specimen becomes depleted in Cr and Mn, Fe starts to react and dissolve into the salt.

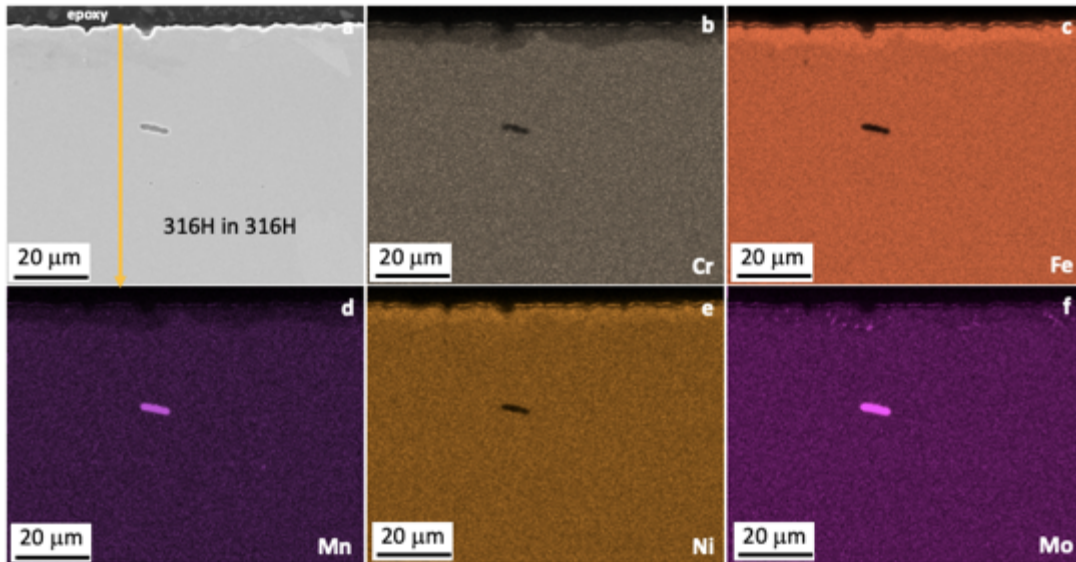


Figure 4-23. (a) SEM image of a polished cross-section of a 316H specimen exposed for 500 h at 700°C to dried FLiNaK salt in a 316H capsule and (b-f) EDS maps of the same region.

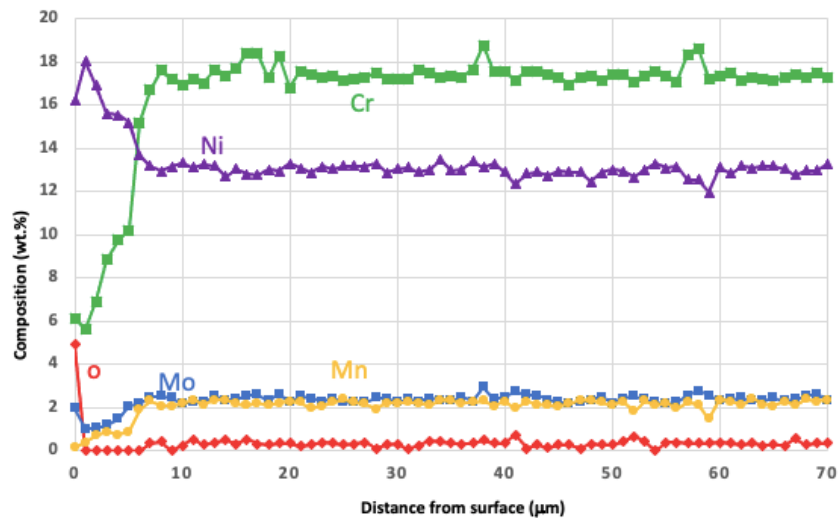


Figure 4-24. EDS profile from the line shown in Figure 4-23a of a 316H specimen exposed for 500 h at 700°C to dried FLiNaK salt in a 316H capsule.

The most severe attack based on mass loss was observed with Ni capsules for both alloys, Figure 4-20. The maps for the 316H specimen in Figure 4-32 show a severe Fe depletion at the surface (Figure 4-32c) which suggests a reaction occurred with the Ni capsule, similar to what was observed in Cl salt, Figure 4-12. The line profile in Figure 4-33 also suggests a Cr-rich oxide formed at the surface. At the same time, grain boundaries were depleted in Cr to a depth of more than 450 μm . For the 709 specimen, the attack was not as deep, which is consistent with the mass loss data in Figure 4-20. The maps in Figure 4-34 suggest a Cr-rich layer.

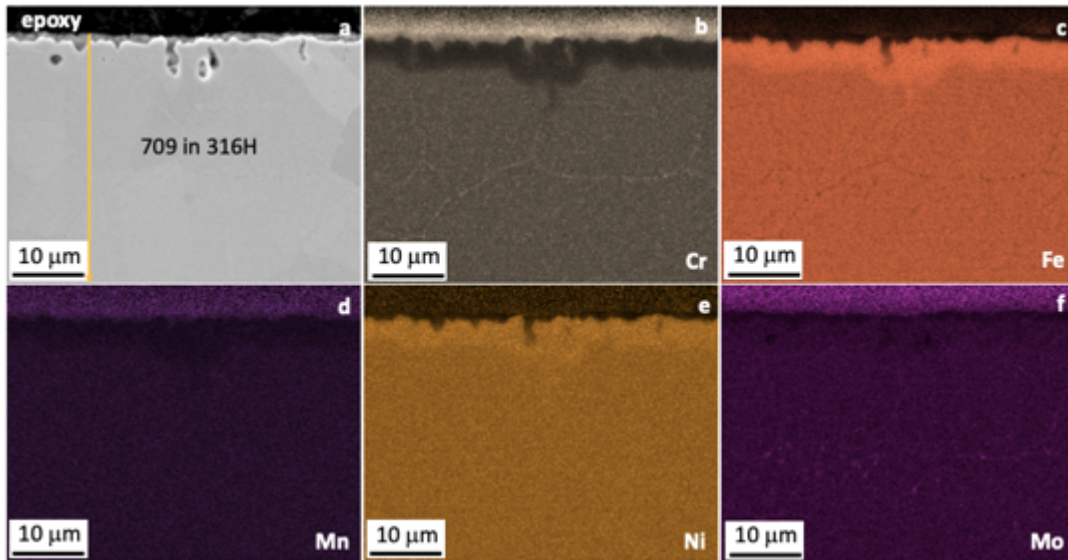


Figure 4-25. (a) SEM image of a polished cross-section of a 709 specimen exposed for 500 h at 700°C to dried FLiNaK salt in a 316H capsule and (b-f) EDS maps of the same region. The Cr, Mn and Mo signals in the epoxy is an artifact.

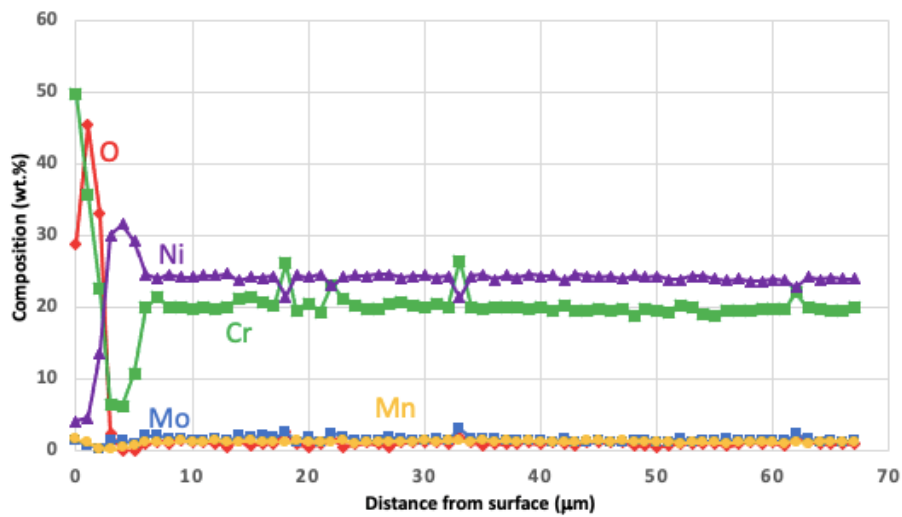


Figure 4-26. EDS profile from the line shown in Figure 4-25a of a 709 specimen exposed for 500 h at 700°C to dried FLiNaK salt in a 316H capsule.

The line profile in Figure 4-35 indicates it is an oxide and that the underlying Cr depletion is more than 100 μm.

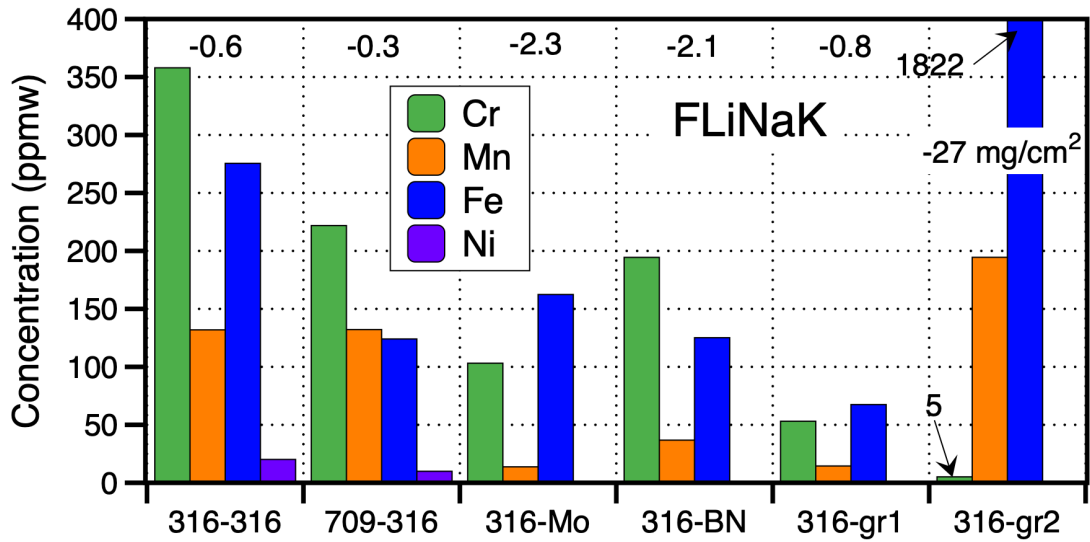


Figure 4-27. Post-test metallic salt impurities measured by ICP-OES in the dried FLiNaK salt in the various capsule experiments with 316H and 709 specimens. Two different graphite capsules were measured (gr1 gr2).

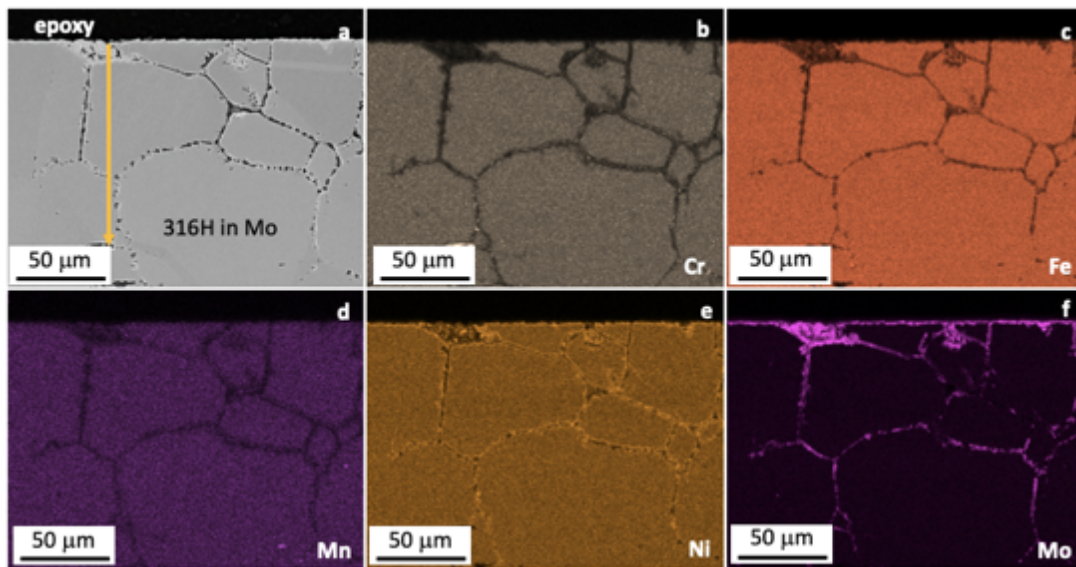


Figure 4-28. (a) SEM image of a polished cross-section of a 316H specimen exposed for 500 h at 700°C to dried FLiNaK salt in a Mo capsule and (b-f) EDS maps of the same region.

For the BN crucible, the attack on the 316H specimen was ~25 μm and fairly uniform, Figures 4-36 and 4-37. There was no indication of a Cr-rich layer but O was slightly enriched at the specimen surface. The affected surface layer was depleted in Cr and rich in Ni and Fe with some Mo-rich precipitates, Figure 4-36f. The post-test salt chemistry showed similar Cr and Fe levels as the Mo capsule but with the Cr:Fe ratio reversed and a higher Cr content in the salt from the BN crucible.

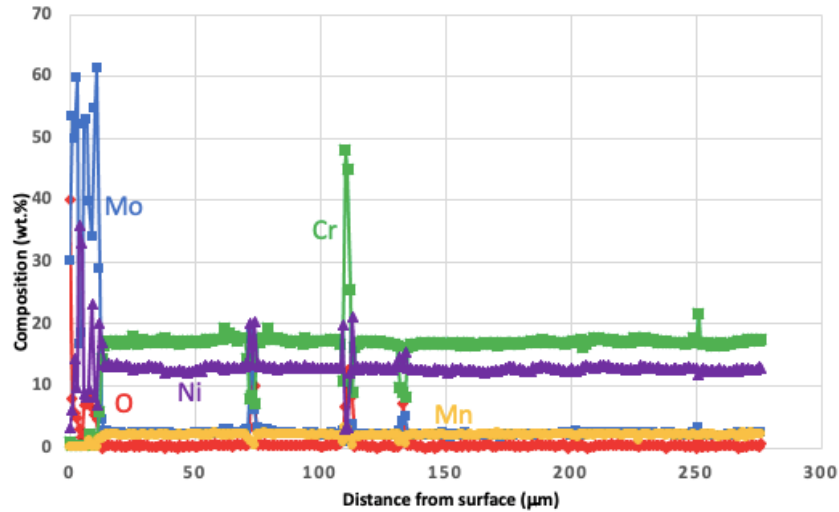


Figure 4-29. EDS profile from the line shown in Figure 4-28a of a 316H specimen exposed for 500 h at 700°C to dried FLiNaK salt in a Mo capsule.

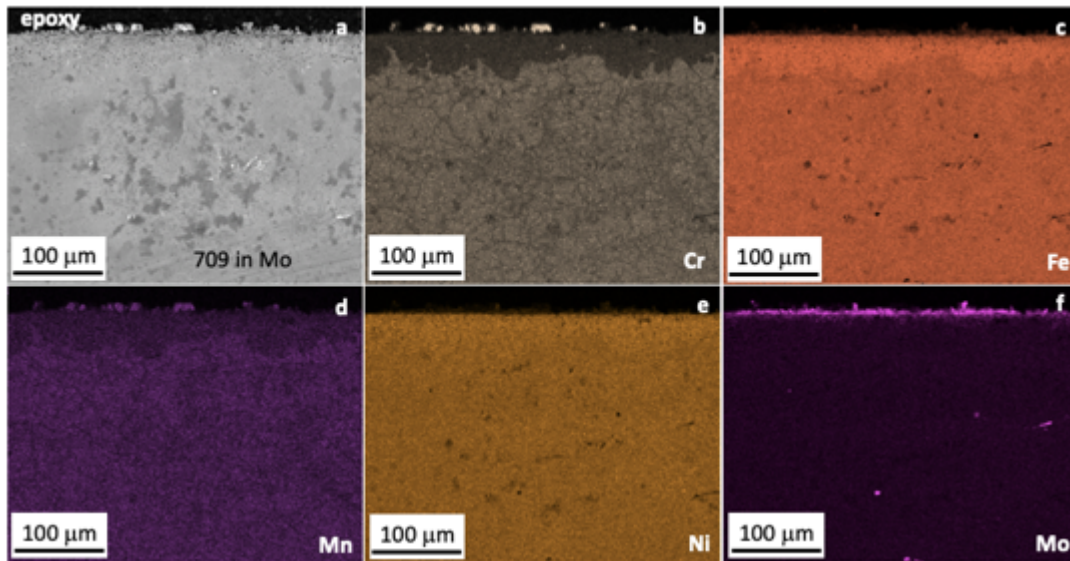


Figure 4-30. (a) SEM image of a polished cross-section of a 709 specimen exposed for 500 h at 700°C to dried FLiNaK salt in a Mo capsule and (b-f) EDS maps of the same region.

With a graphite crucible, a complex reaction layer formed on the 316H specimen, Figures 4-38 and 4-39. The whisker in Figure 4-20 indicates a high standard deviation with mass changes of -0.8 , -1.7 and -27.1 mg/cm^2 in the three capsule experiments with graphite crucibles. The formation of a reaction product could affect the results depending on its adhesion. The EDS system is not well-suited for detecting and quantifying light elements like C and O. The algorithms to convert EDS x-ray counts to compositions are most accurate for common elements like Fe, Cr and Ni. In this case, both Cr-rich oxides and carbides could have formed. Two salt samples were analyzed from graphite crucibles, gr1 and gr2 in Figure 4-27. With the small mass loss of 0.8 mg/cm^2 , small amounts of Cr, Mn and Fe were detected (gr1). With the large mass loss of 27.1 mg/cm^2 , a very large Fe content was observed and a low Cr content (gr2).

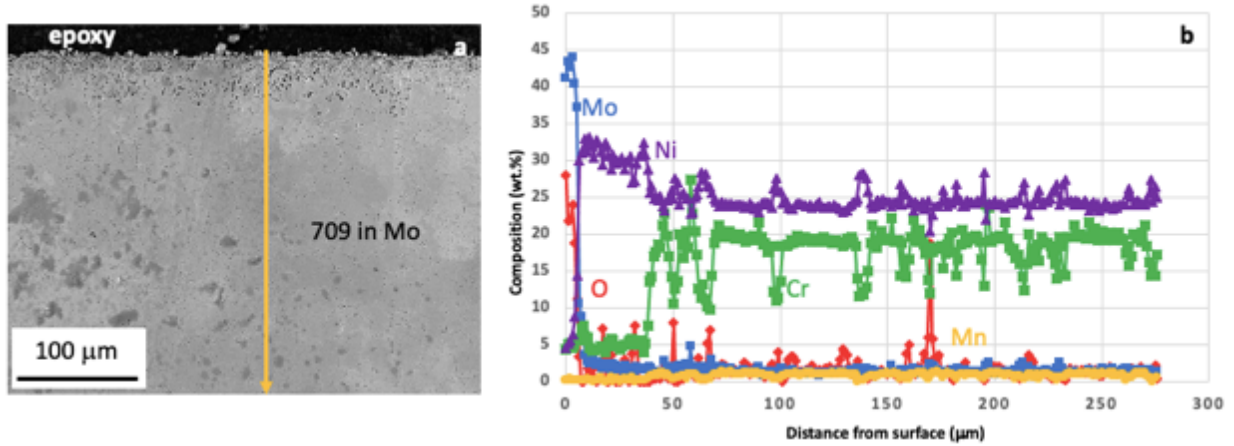


Figure 4-31. (a) SEM image of a polished cross-section of a 709 specimen exposed for 500 h at 700°C to dried FLiNaK salt in a Mo capsule and (b) EDS profile from the line shown in (a).

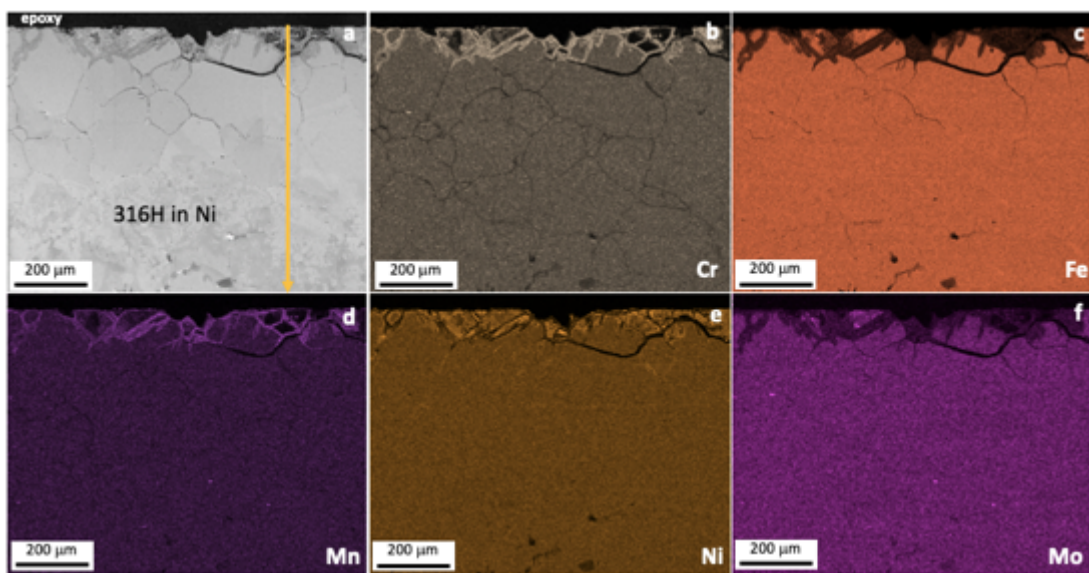


Figure 4-32. (a) SEM image of a polished cross-section of a 316H specimen exposed for 500 h at 700°C to dried FLiNaK salt in a Ni capsule and (b-f) EDS maps of the same region.

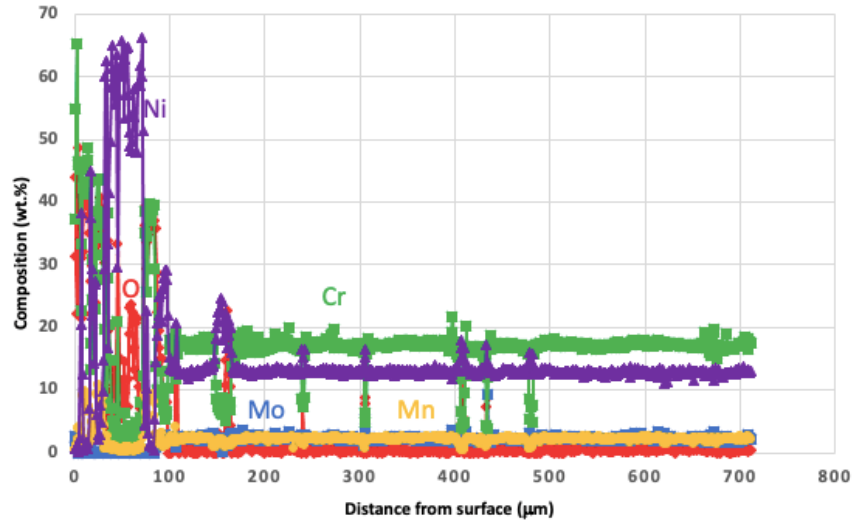


Figure 4-33. EDS profile from the line shown in Figure 4-28a of a 316H specimen exposed for 500 h at 700°C to dried FLiNaK salt in a Ni capsule.

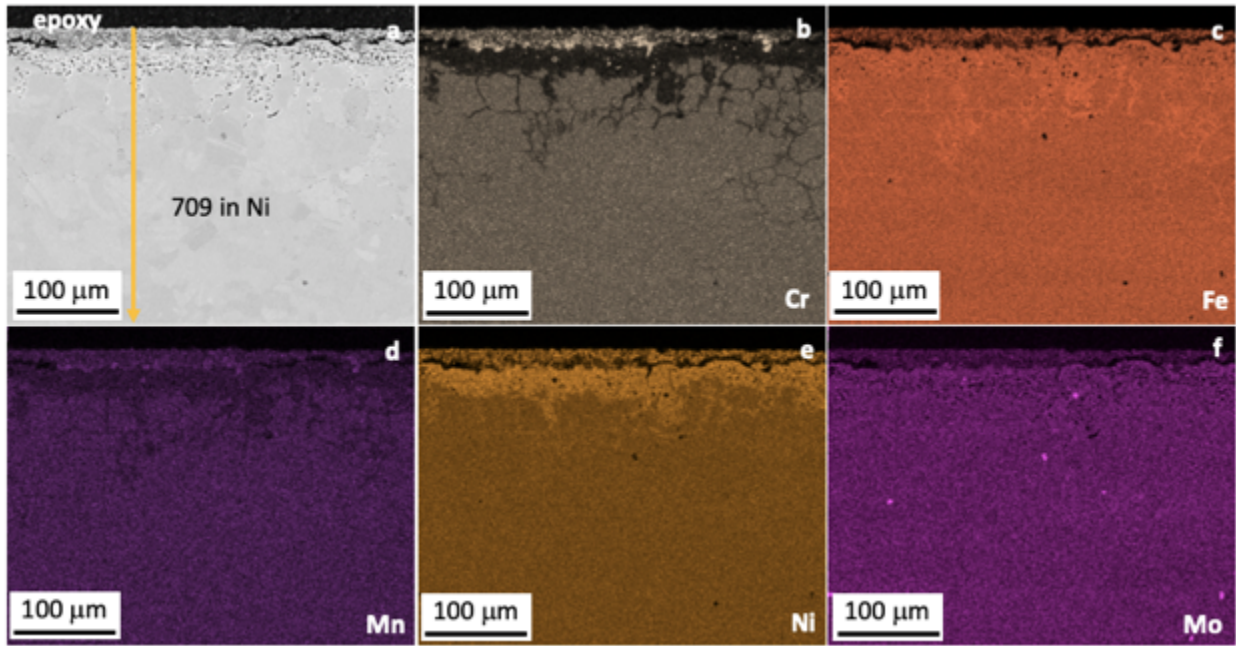


Figure 4-34. (a) SEM image of a polished cross-section of a 709 specimen exposed for 500 h at 700°C to dried FLiNaK salt in a Ni capsule and (b-f) EDS maps of the same region.

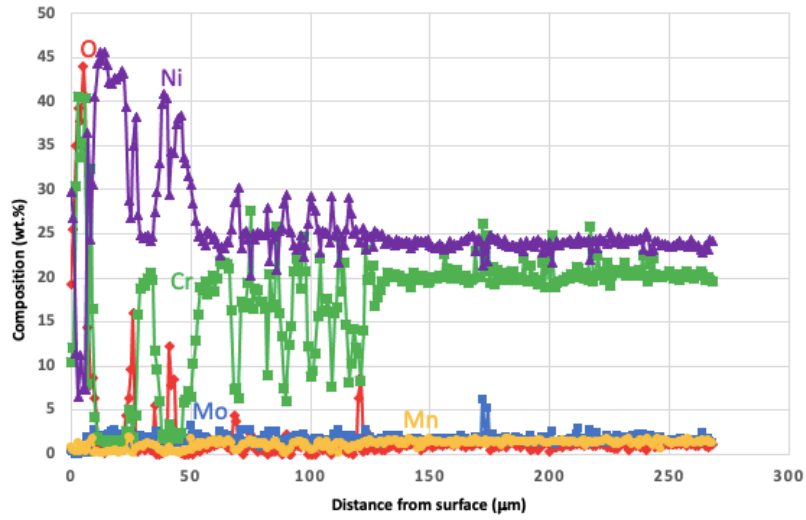


Figure 4-35. EDS profile from the line shown in Figure 4-34a of a 709 specimen exposed for 500 h at 700°C to dried FLiNaK salt in a Ni capsule.

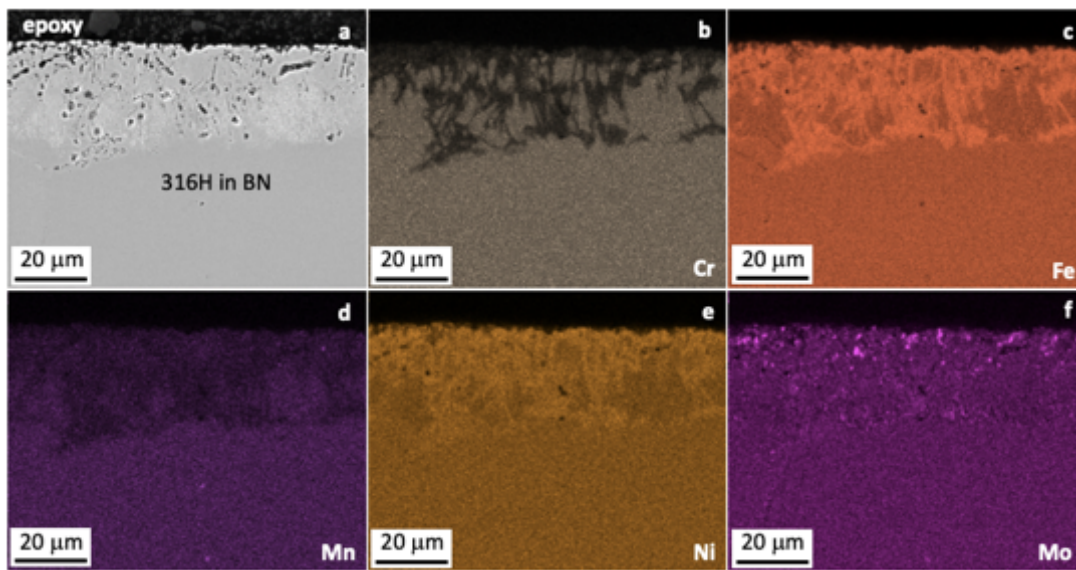


Figure 4-36. (a) SEM image of a polished cross-section of a 316H specimen exposed for 500 h at 700°C to dried FLiNaK salt in a BN crucible and (b-f) EDS maps of the same region.

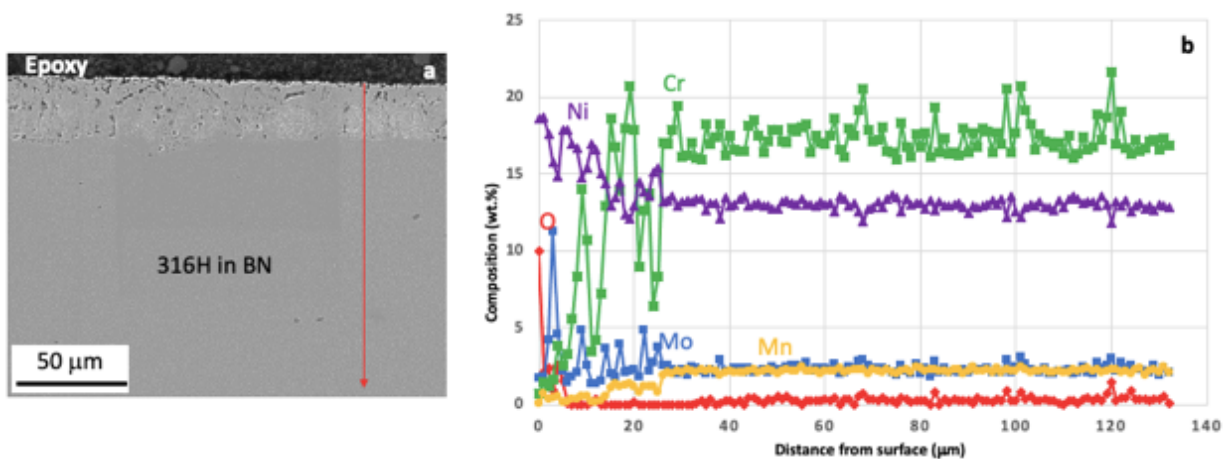


Figure 4-37. (a) SEM image of a polished cross-section of a 316H specimen exposed for 500 h at 700°C to dried FLiNaK salt in a BN container and (b) EDS profile from the line shown in (a).

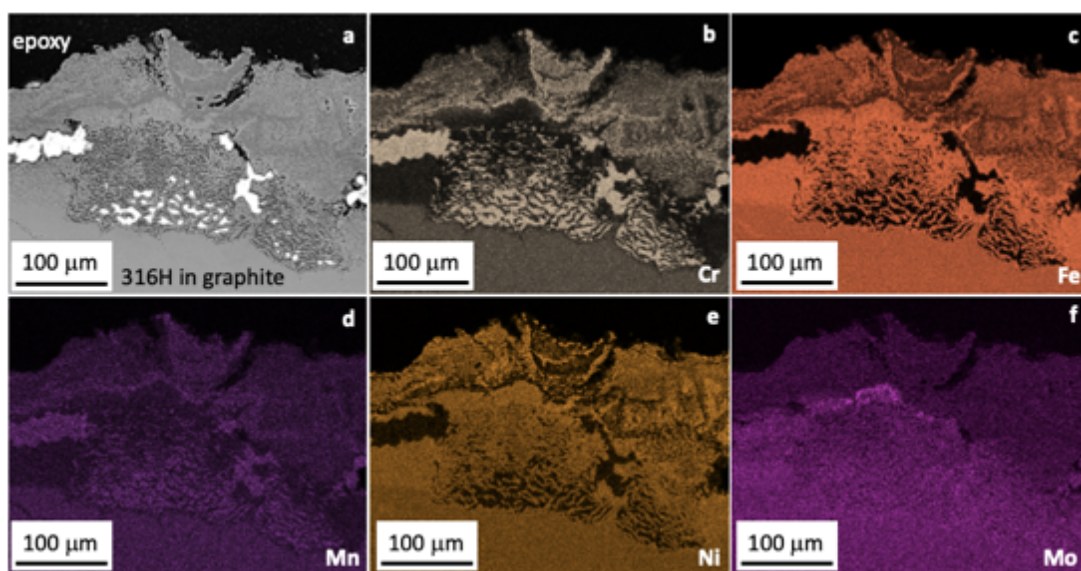


Figure 4-38. (a) SEM image of a polished cross-section of a 316H specimen exposed for 500 h at 700°C to dried FLiNaK salt in a graphite crucible and (b-f) EDS maps of the same region.

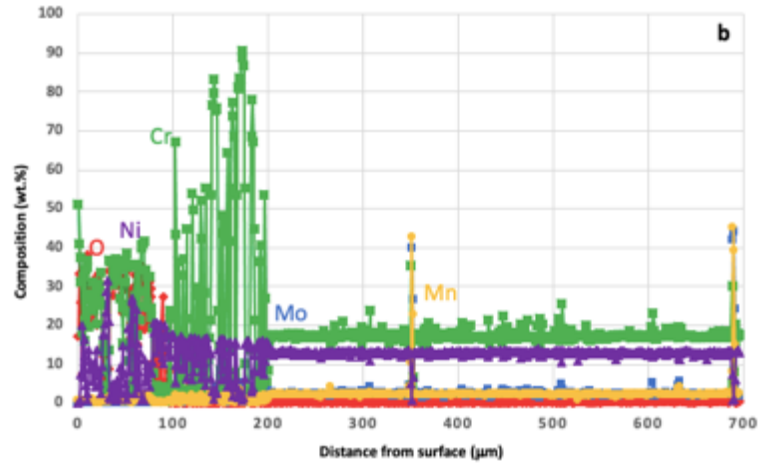
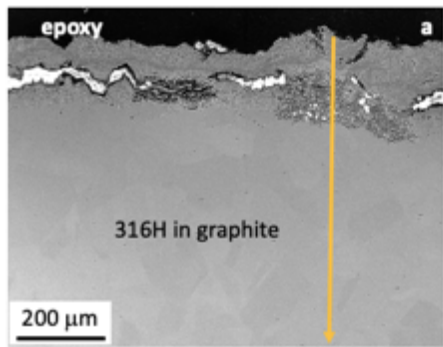


Figure 4-39. (a) SEM image of a polished cross-section of a 316H specimen exposed for 500 h at 700°C to dried FLiNaK salt in a graphite container and (b) EDS profile from the line shown in (a).

Finally, two Ni-based alloys, Hastelloy N and 617 were compared in three different capsules, Figure 4-40. Especially the results for alloy 617 with 22%Cr (Table 3-1) may have been heavily influenced by the high O content in the FLiNaK. All three 617 specimens exposed in Mo and in Hastelloy N capsules exhibited mass gains (only one Hastelloy N specimen showed a mass gain with a Mo capsule). Similar to the other groups of results, the largest mass losses occurred with Ni capsules.

Figure 4-41 shows a representative image of each condition. In this case, the magnification is higher than in other cases (Figures 4-3 and 4-21). For the Hastelloy N specimens, the results suggest uniform Cr depletion. In contrast, the alloy 617 results suggest that a reaction product formed that had poor adhesion which may have complicated the mass change results.

In Figure 4-42, depth of attack measurements are shown for Hastelloy N specimens and they are generally consistent with the light microscopy in Figure 4-41. In general, the alloy 617 specimens showed more attack than the low Cr alloy N. Also, the deepest attack occurred in the Ni capsules.

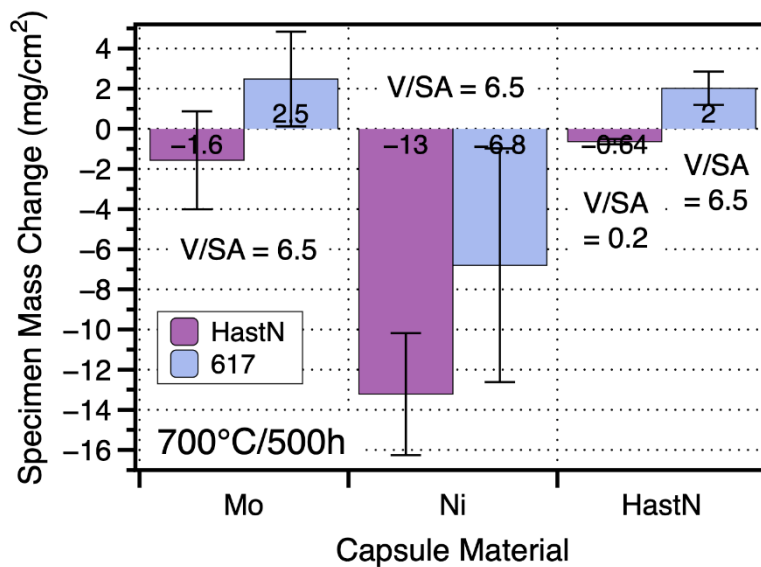


Figure 4-40. Specimen mass loss for Ni-based Hastelloy N and 617 specimens in 3 different container materials after 500 h at 700°C in dried FLiNaK salt. The bars show the average of three capsule experiments and the whiskers show one standard deviation.

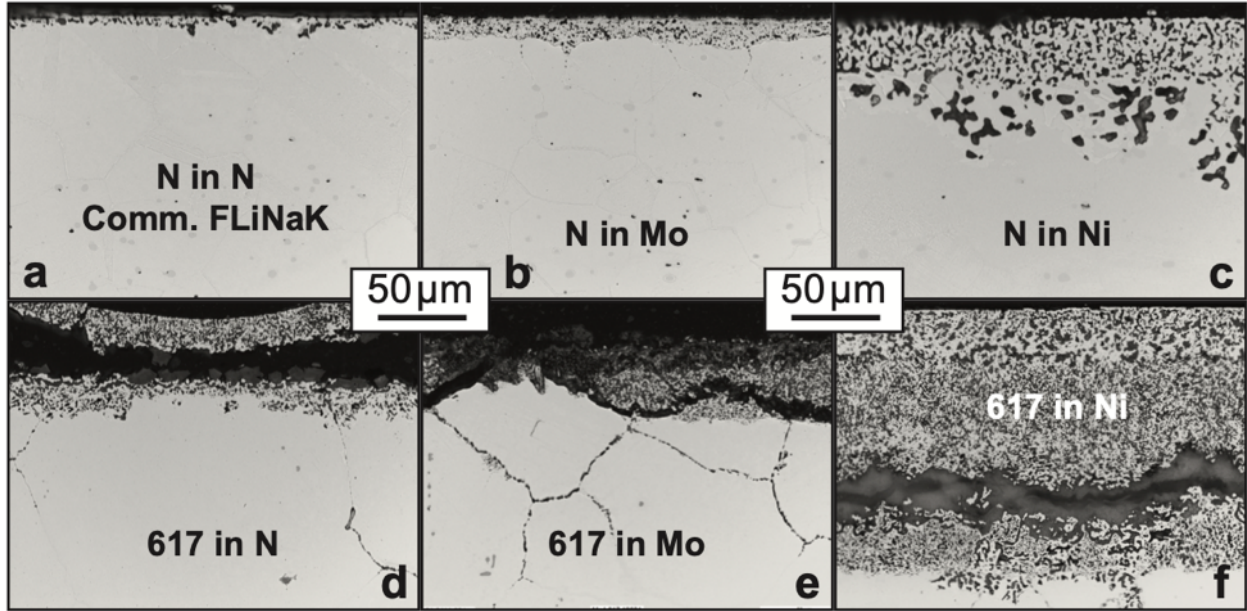


Figure 4-41. Light microscopy of polished sections of representative Ni-based alloys (a-c) Hastelloy N and (d-f) 617 specimens exposed for 500 h at 700°C in FLiNaK salt (a,d) 316H capsule, (b,e) Mo capsule and (c,f) Ni capsule.

Figure 4-43 shows the smallest attack with Hastelloy N in a Hastelloy N capsule because of the low V/SA ratio (see section 2). The Cr depletion was to a depth of ~20 μm (Figure 4-44) with voids forming to a shallower depth. The Cr and O maps suggest that oxides formed in some voids. The slight Mo depletion near the surface shown in the line profile could be due to Mo oxidation. Figure 4-45 summarizes the post-test salt chemistry results. With the alloy N capsule and specimen, the Cr content was relatively low with a surprisingly high Mn content, considering the low (0.3%, Table 3-1) Mn content in alloy N.

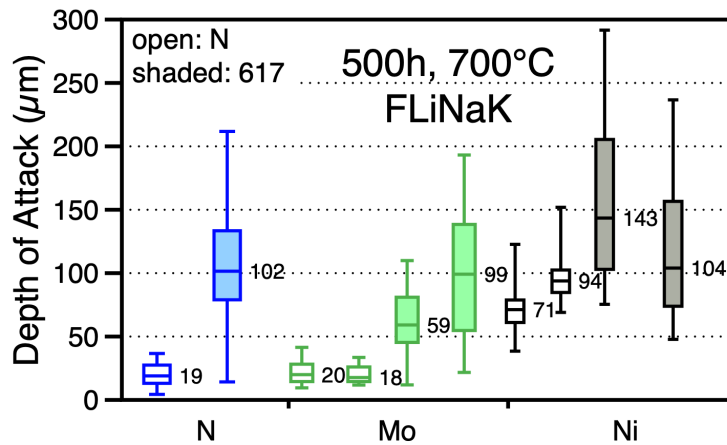


Figure 4-42. Box and whisker plots of the depth of attack based on the light microscopy images of selected specimens exposed to FLiNaK salt. The median values are shown and the boxes are defined by the 25% and 75% values. The whiskers show the minimum and maximum values measured.

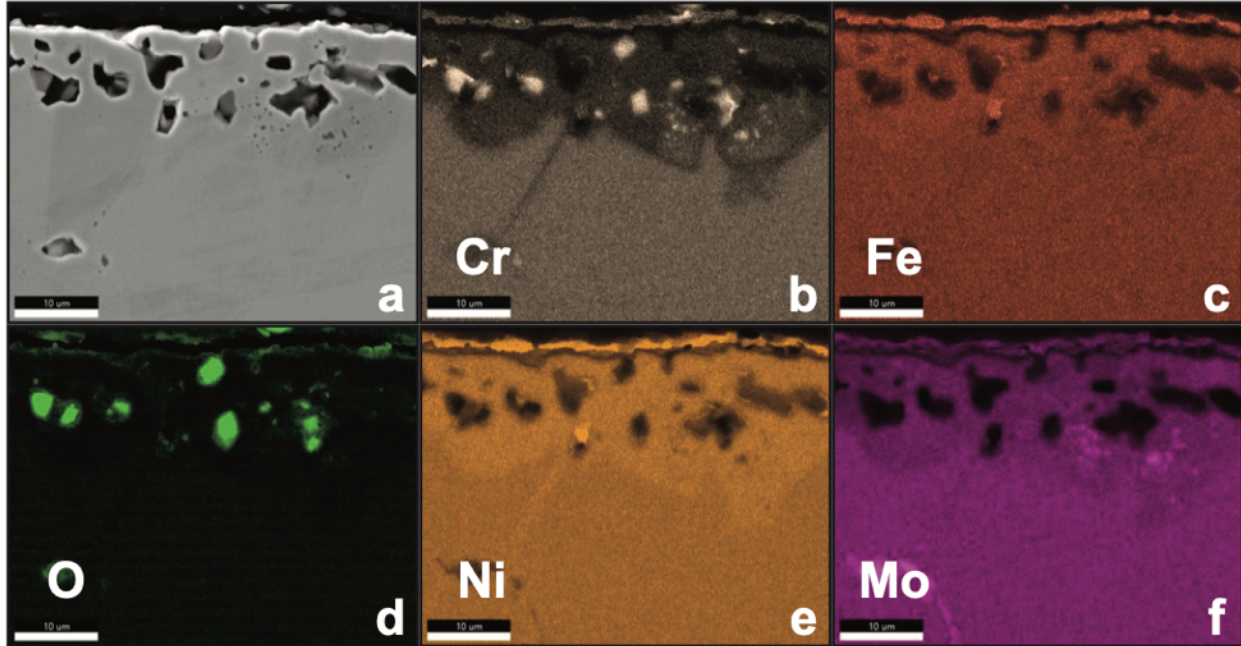


Figure 4-43. (a) SEM image of a polished cross-section of a Hastelloy N specimen exposed for 500 h at 700°C to dried FLiNaK salt in an alloy N capsule and (b-f) EDS maps of the same region.

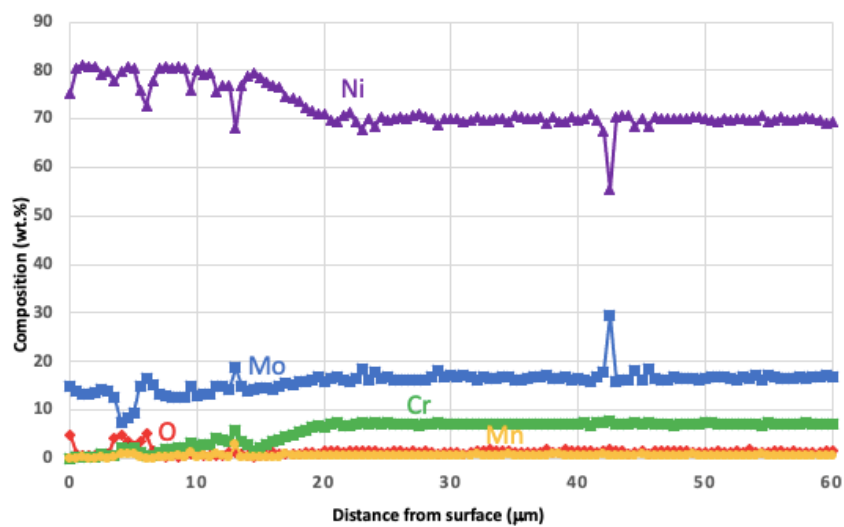


Figure 4-44. EDS profile from the line shown in Figure 4-39a of a Hastelloy N specimen exposed for 500 h at 700°C to dried FLiNaK salt in an alloy N capsule.

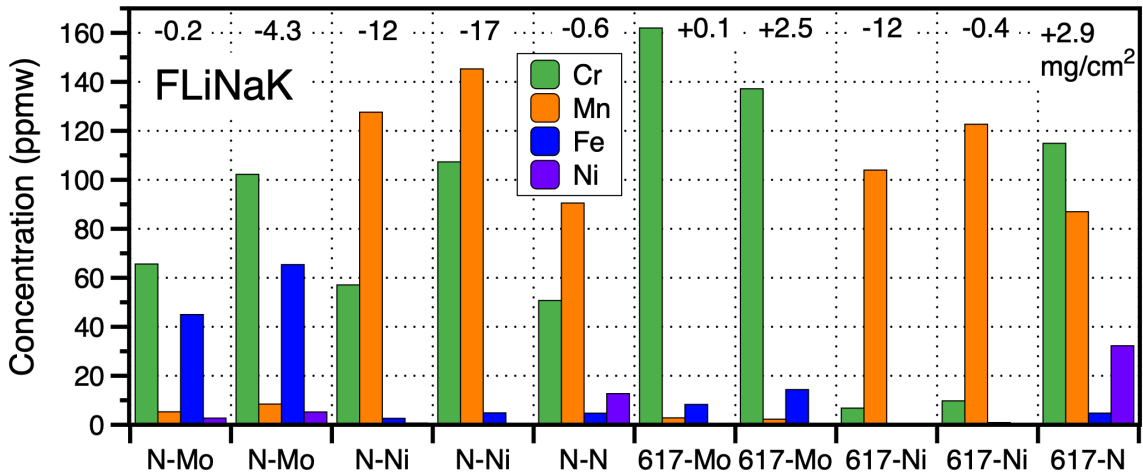


Figure 4-45. Post-test metallic salt impurities measured by ICP-OES in the dried FLiNaK salt in the various capsule experiments with alloys N and 617 specimens.

Switching to a Mo capsule, the depth of attack on the alloy N specimen was not significantly deeper but the voids were smaller, Figure 4-46. The Cr depletion was >20 μm and the outer layer contained mainly Ni, Mo and O, Figure 4-47. Salt from two capsules was analyzed because of the range in mass change observed, Figure 4-45. Compared to the alloy N capsule salt chemistry, the post-test salt in a Mo capsule had much higher Fe and was slightly higher in Cr.

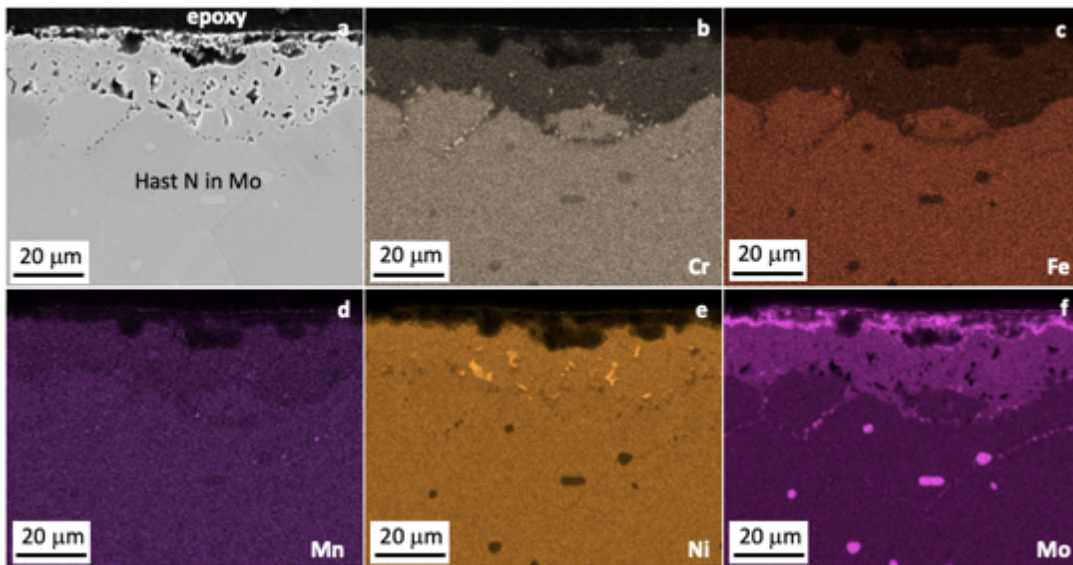


Figure 4-46. (a) SEM image of a polished cross-section of a Hastelloy N specimen exposed for 500 h at 700°C to dried FLiNaK salt in a Mo capsule and (b-f) EDS maps of the same region.

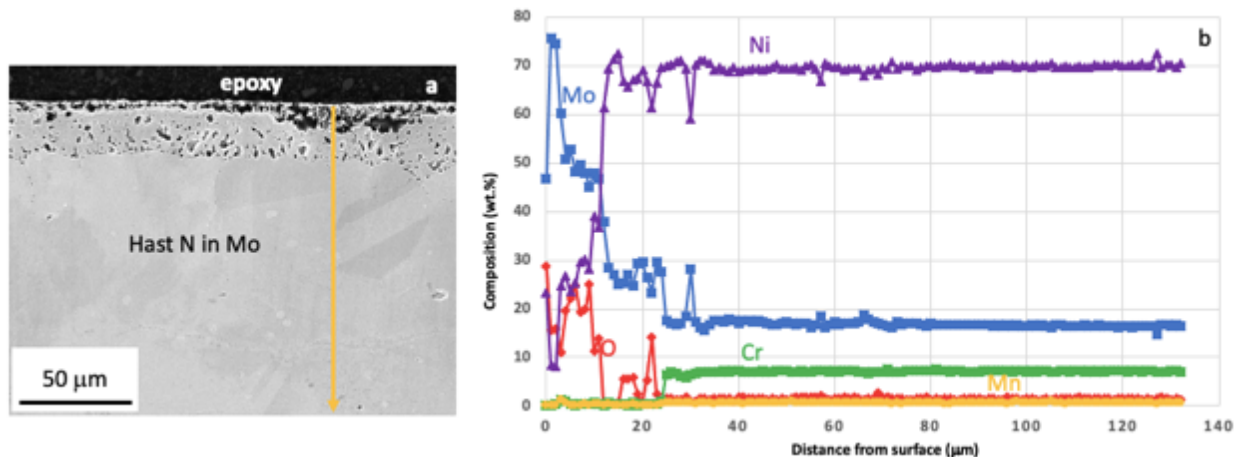


Figure 4-47. a) SEM image of a polished cross-section of a Hastelloy N specimen exposed for 500 h at 700°C to dried FLiNaK salt in a Mo capsule and (b) EDS profile from the line shown in (a).

For the Ni capsule, the depth of attack on the alloy N specimen was substantially increased, Figures 4-48 and 4-49. The Cr depletion was $\sim 75 \mu\text{m}$ and the Mo also was depleted to a depth of $\sim 60 \mu\text{m}$. A small O signal was detected in the porous outer layer that was rich in Ni. In the salt after exposure, high levels of Mn were observed, Figure 4-45. Similar levels of Cr were measured as in the Mo capsules but the Fe levels were much lower.

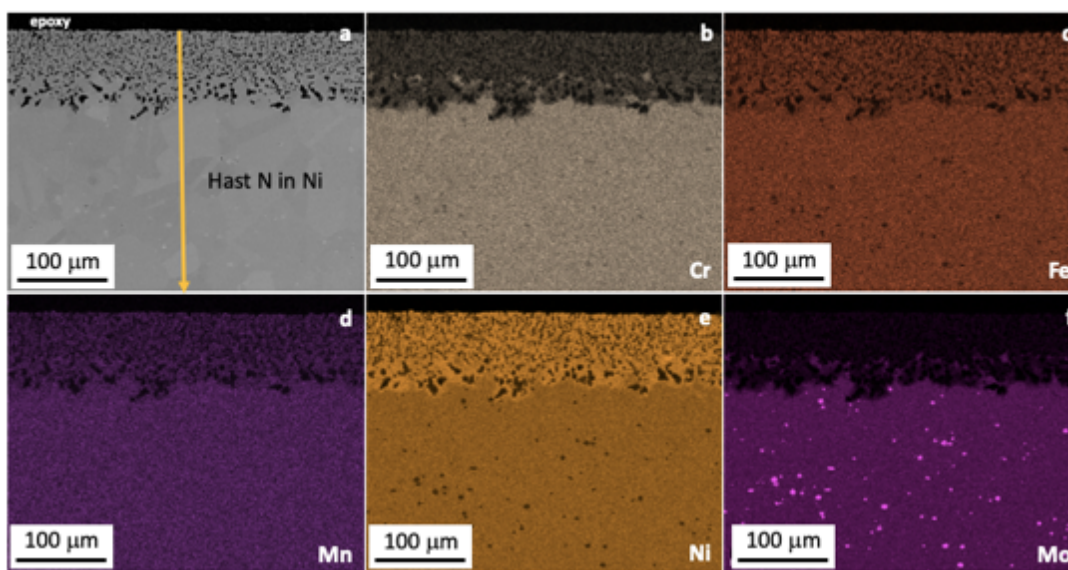


Figure 4-48. (a) SEM image of a polished cross-section of a Hastelloy N specimen exposed for 500 h at 700°C to dried FLiNaK salt in a Ni capsule and (b-f) EDS maps of the same region.

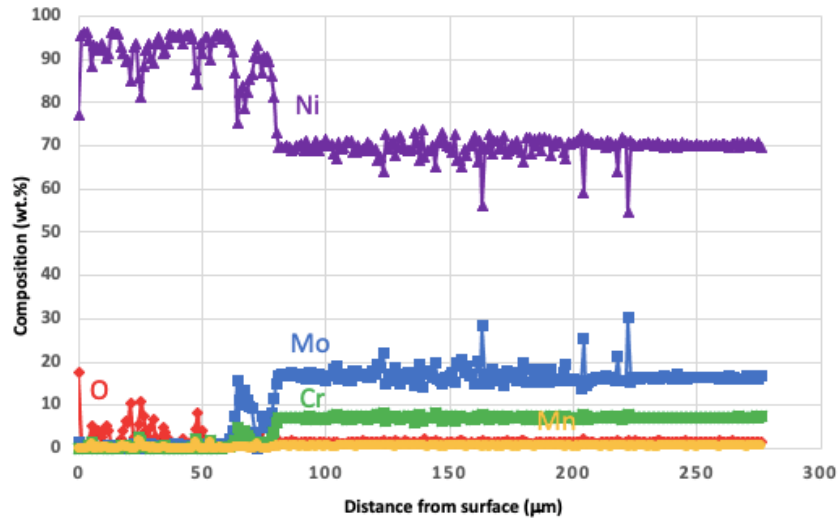


Figure 4-49. EDS profile from the line shown in Figure 43a of a Hastelloy N specimen exposed for 500 h at 700°C to dried FLiNaK salt in a Ni capsule.

More complex reaction products formed on the 617 specimens in all three cases. With the Hastelloy N capsule, the Ni- and Mo-rich outer layer appeared to lift off the surface, Figures 4-50 and 4-51. The Cr-rich particles appear to be oxides. The post-test salt analysis showed high levels of Cr, Mn and Ni after this exposure, Figure 4-45.

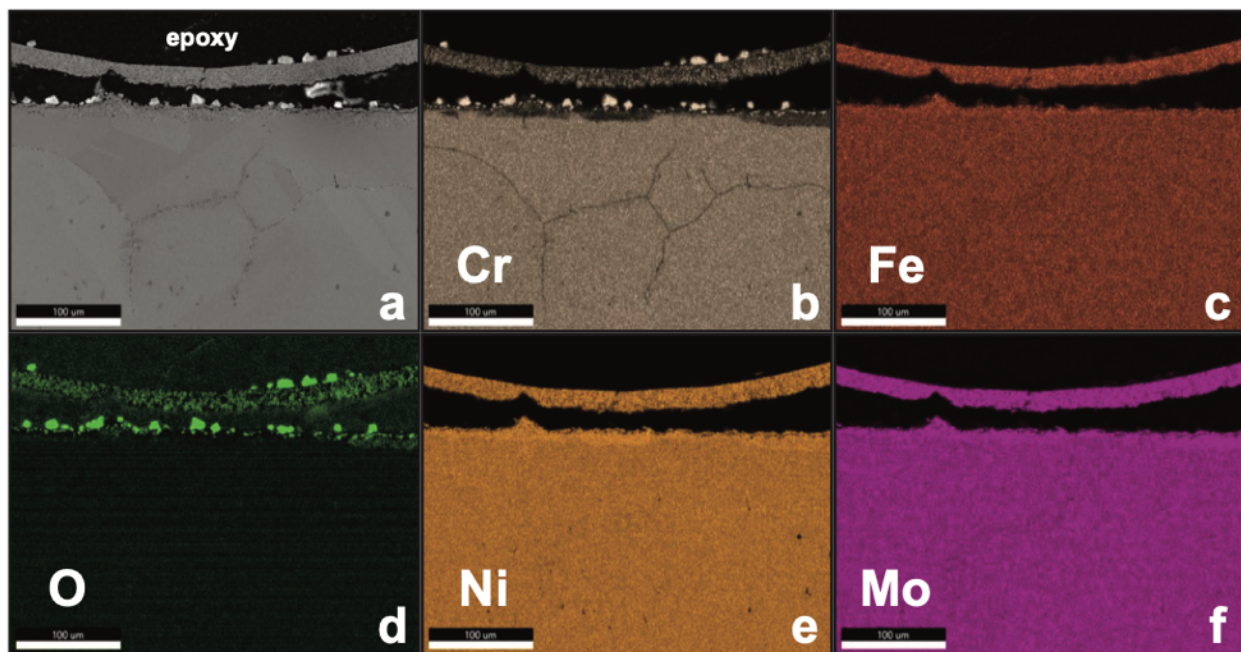


Figure 4-50. (a) SEM image of a polished cross-section of a 617 specimen exposed for 500 h at 700°C to dried FLiNaK salt in an alloy N capsule and (b-f) EDS maps of the same region.

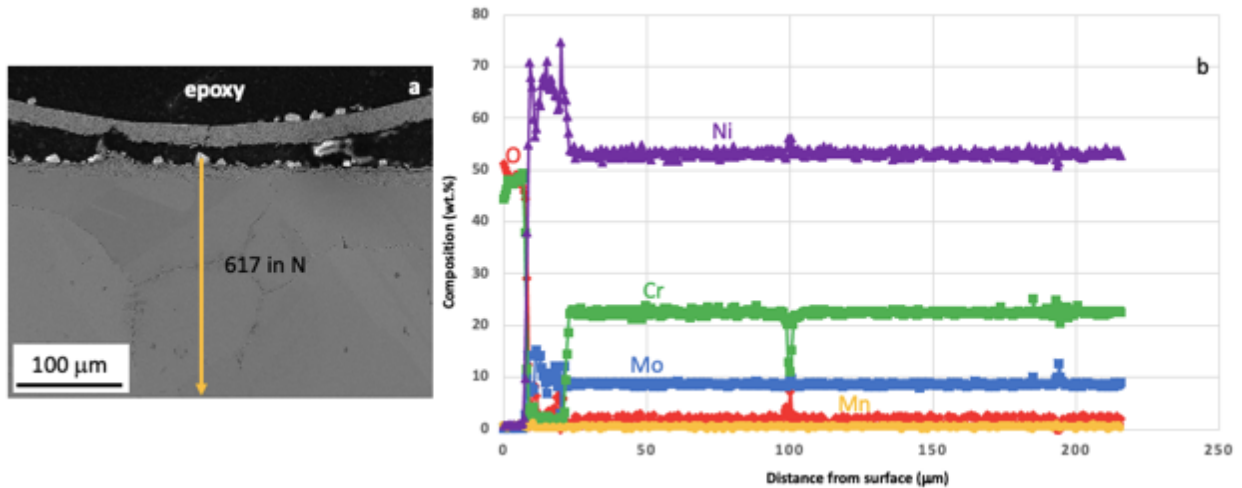


Figure 4-51. (a) SEM image of a polished cross-section of a 617 specimen exposed for 500 h at 700°C to dried FLiNaK salt in an alloy N capsule and (b) EDS profile from the line shown in (a).

With a Mo capsule, a similar, but thicker, Ni-Mo-O outer layer appeared to form on the 617 specimen, Figures 4-52 and 4-53. Whiskers at the outer surfaces may be Cr-rich oxide. Similar to the alloy N capsules, the post-test salt analysis showed low Mn and Fe levels and high Cr contents, Figure 4-45.

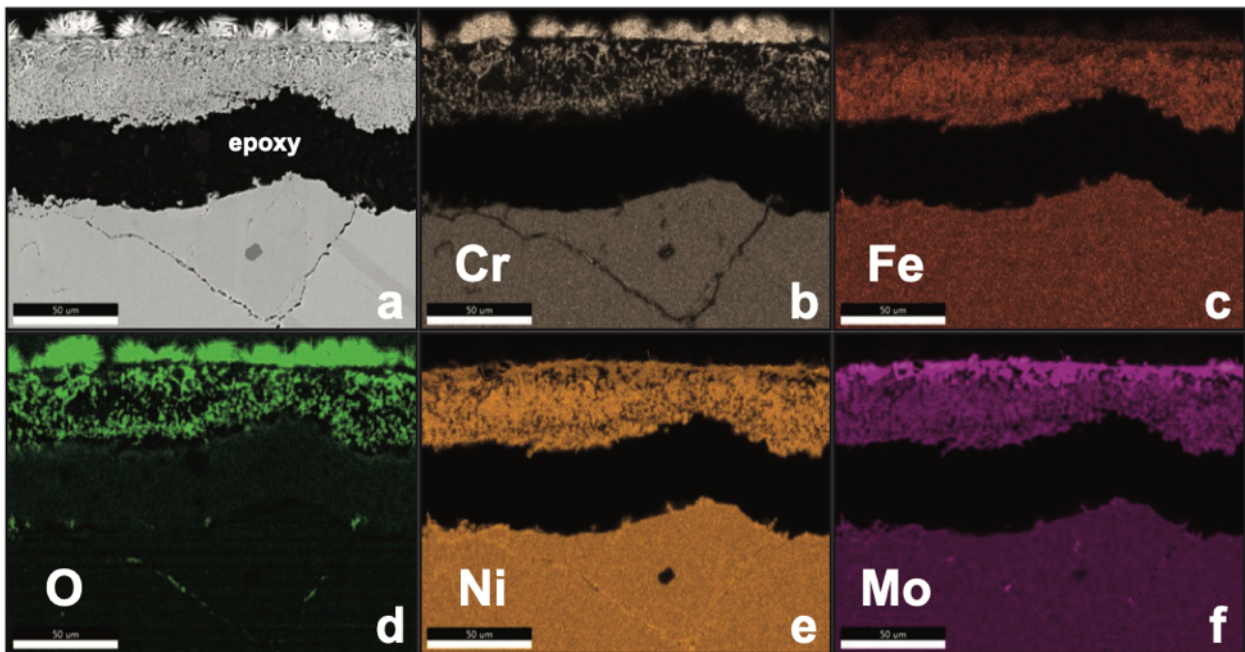


Figure 4-52. (a) SEM image of a polished cross-section of a 617 specimen exposed for 500 h at 700°C to dried FLiNaK salt in a Mo capsule and (b-f) EDS maps of the same region.

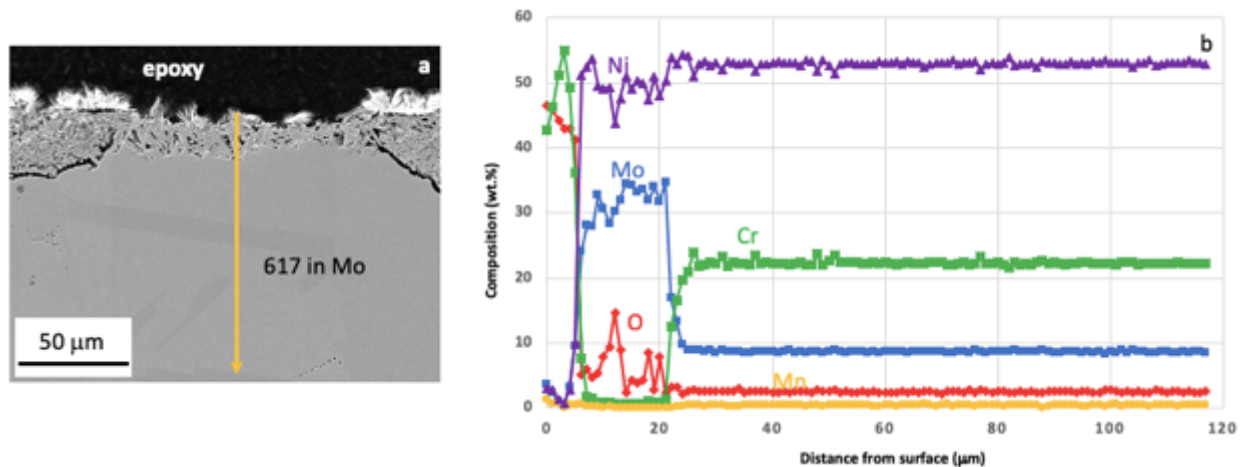


Figure 4-53. (a) SEM image of a polished cross-section of a 617 specimen exposed for 500 h at 700°C to dried FLiNaK salt in a Mo capsule and (b) EDS profile from the line shown in (a).

Switching to a Ni capsule, the Cr depleted region increased to ~140 μm on the 617 specimen, Figures 4-54 and 4-55. The small amount of Cr in the outer layer may be oxides. Figure 4-45 shows mainly Mn in the salt after the test. This is quite unusual since the Mn content of 617 is only 0.1%.

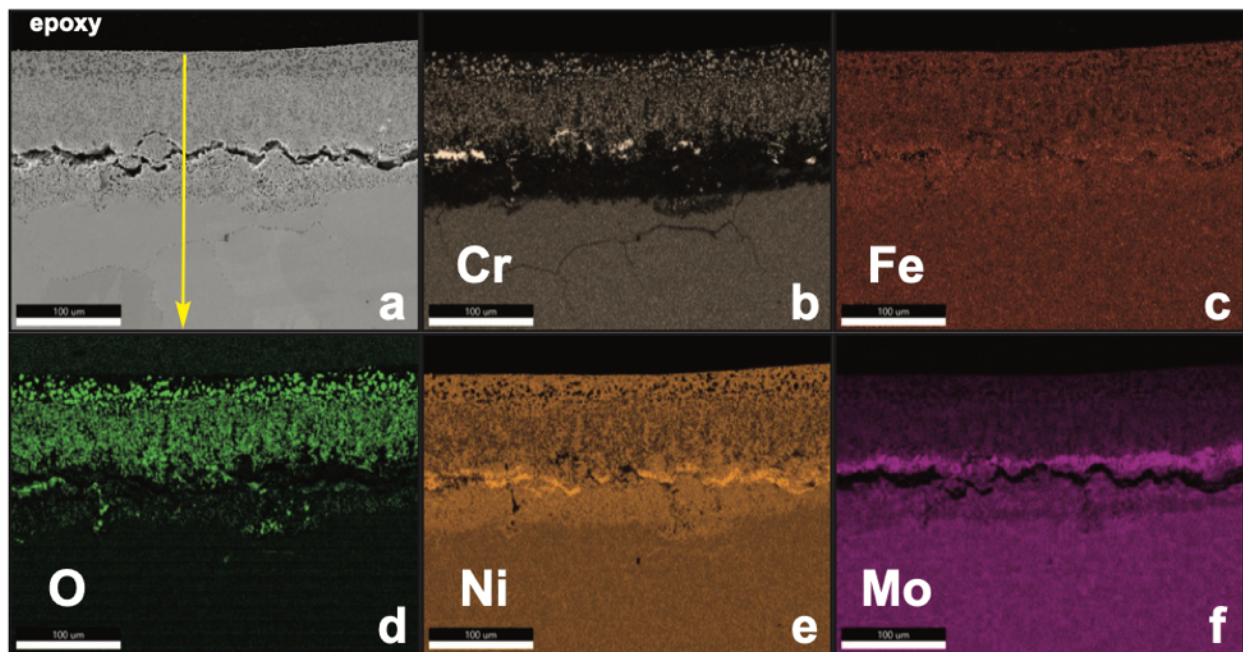


Figure 4-54. (a) SEM image of a polished cross-section of a 617 specimen exposed for 500 h at 700°C to dried FLiNaK salt in a Ni capsule and (b-f) EDS maps of the same region.

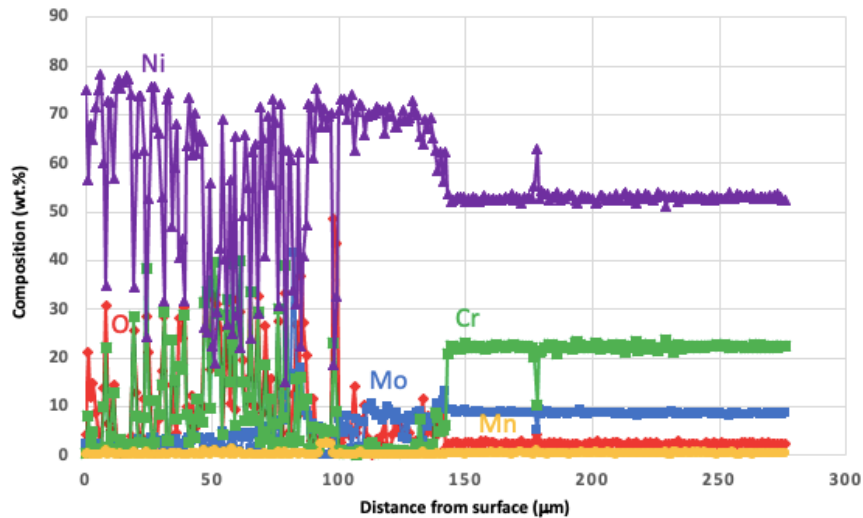


Figure 4-55. EDS profile from the line shown in Figure 4-54a of a 617 specimen exposed for 500 h at 700°C to dried FLiNaK salt in a Ni capsule.

4.4 DISCUSSION

It is very clear from the results that the salt container has a considerable effect on the mass change results. It is already known from the literature that graphite, quartz and Ni crucibles are not useful as they are likely more reactive than Mo [Olson 2015, Raiman 2021, Parker 2022]. It remains to be determined if this is mainly a chemical effect or an electrochemical effect [Olson 2015, Guo 2018, Ding 2019, Parker 2022]. A monometallic experiment, i.e. 316H in a 316H container, is the most ideal experiment to eliminate any dissimilar material effects. It may also be the most realistic for the application depending on the V/SA of the reactor design. However, the low V/SA ratio results in very small mass changes, Figure 4-2. From a chemistry standpoint, the use of graphite containers could lead to the formation of Cr- or Fe-rich carbides. The use of Ni could result in alloying of Fe and Cr into the capsule wall which would greatly accelerate attack for 316H with relatively high levels of Fe and Cr. The acceleration with a Ni capsule was observed previously for capsule experiments conducted at 800°C [Pint 2019]. Reactions with Mo are less extensive but also could occur. With these experiments at 700°C, the surface reaction would be harder to quantify after only 500 h.

Table 4-2 summarizes the capsules that were examined after salt exposure for 500 h at 700°C. For the FLiNaK salt, only a few capsules were examined. The initial Ni capsules examined showed low levels of Cr (Figure 4-12) but much higher Fe contents without Mg in the Cl salt. This is understandable because Mg lowers the salt redox potential and reduces the amount of Fe dissolution. Because the capsule is removing Fe from the salt, the specimen continues to dissolve and does not approach equilibrium. Figure 4-56 shows an EDS profile from a 316H capsule. Some residual salt debris was on the surface but the metal surface clearly showed Cr and Mn depletion, similar to the specimen shown in Figure 4.6. As noted in Table 4-2, the amount of interdiffusion in FLiNaK was much less and not as easy to detect.

Table 4-2. Summary of capsules analyzed after salt exposure for 500 h at 700°C

Capsule	Specimen	Salt	Comments
Ni	316H	Mg ₂ Cl+NaCl	Large Fe interdiffusion observed
Ni	316H	Mg ₂ Cl+NaCl+Mg	Less interdiffusion, higher Cr level
Mo	316H	Mg ₂ Cl+NaCl+Mg	No clear evidence of Cr or Fe
316H	316H	Mg ₂ Cl+NaCl+Mg	~5μm Cr and Mn depletion

Ni	N	FLiNaK	Minor Cr, Fe signal at surface
Ni	617	FLiNaK	Possible Cr-rich layer at surface, very thin

The salt chemistry data (Figures 4-7, 4-27 and 4-45) was a small sampling from the total number of capsules run in this task. The measurements were conducted after it was recognized that such information was useful in assessing behavior. Mass change is the easiest metric for assessment but specimen microstructure and salt chemistry help to assess behavior in a more comprehensive manner.

The commercial, dried FLiNaK used in this experiment is a concern, primarily because of the high O content. Among the three batches of FLiNaK compared in Table 4-1, the mass losses were the highest for the ORNL laboratory batch (Figure 4-57) which also contained high levels of Ni. No direct comparisons have been conducted with the commercial FLiNaK that was used for a flowing salt experiment [Raiman 2022] and in section #5.

Ultimately it should be recognized that capsule experiments are limited in value and that flowing experiments in a temperature gradient are needed particularly in prototypical conditions to verify salt compatibility.

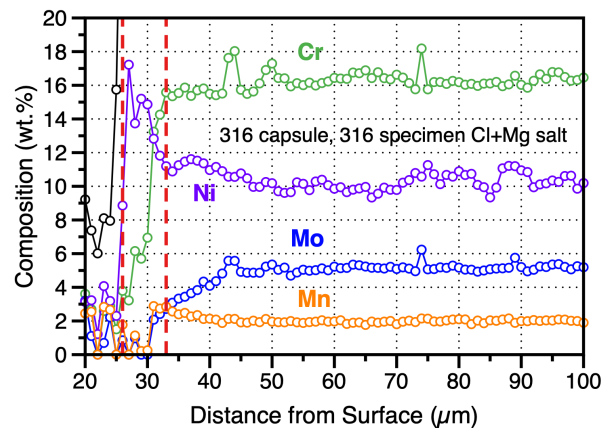


Figure 4-56. EDS line profiles from capsules exposed for 500 h at 700°C to NaCl-Mg₂Cl salt with 316H specimens in a 316H capsule with a Mg addition.

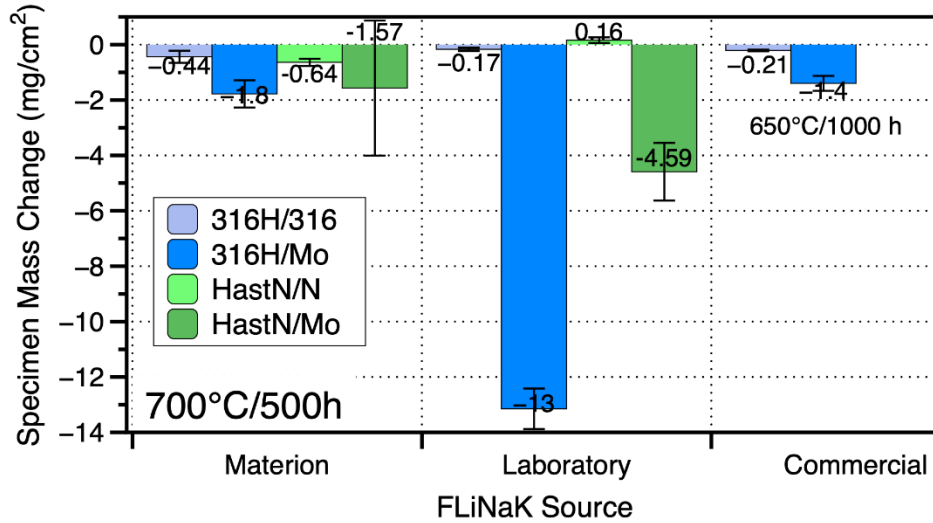


Figure 4-57. Specimen mass loss for 316H and Hastelloy N specimens exposed to three different batches of FLiNaK. The primary comparison between a contaminated batch was conducted for 500 h at 700°C. For a legacy batch of FLiNaK made by ECS, the exposure was 1000 h at 650°C.

4.5 SUMMARY

A set of capsule experiments were conducted to quantify the effect of changing the salt container on the corrosion behavior of 316H in NaCl-MgCl₂ salt with and without Mg additions, and 316H, 709, alloy N, and 617 specimens in dried FLiNaK salt. All of the experiments were conducted in triplicate at 700°C for 500 h. The Ni and graphite crucibles appeared to lead to the largest reactions and should be avoided. This could be easily determined by the large mass losses in these experiments. The high O content of the dried (not purified) FLiNaK salt used in these experiments may have affected the results, particularly for the high Cr alloys, 709 and 617, due to the formation of oxides.

In comparing diverse molten salt compatibility data sets, the container material needs to be considered. While a monometallic experiment is the most ideal, it is not always practical. An inert capsule material was not clearly identified. The BN crucible is the most promising container for these screening experiments but the possible reaction with the alloy to form a nitride needs to be further explored. The results here indicate that issues with the capsule material affecting the compatibility results can be investigated using a thorough characterization methodology where dissolution is quantified by mass loss and metallography and then the dissolution products are quantified in the salt to determine if a reaction with the capsule material affected the reaction.



5. EFFECT OF THE TEST METHODOLOGY (TASK 2)

5.1 EXPERIMENTAL PROCEDURE

5.1.1 Capsule Tests

This procedure was used in the previous sections with 316H specimens (1.5 x 6.5 x 12.5 mm) polished to a 600-grit finish and attached using Mo wire. The Mo capsules were cleaned in a mixture of acetic, nitric and hydrofluoric acids prior to welding and loading with ~24 g FLiNaK salt. As shown in Figure 3-1, the Mo capsule was welded shut and then welded inside a type 304 SS outer capsule. The two FLiNaK salt batches used in this experiment were discussed previously and their compositions are listed in Table 4-1. The commercial FLiNaK had higher purity and contains a Zr getter. This salt has been used in prior capsule and TCL experiments [Raiman 2022]. A batch of laboratory FLiNaK was selected with higher impurities to induce more attack in this experiment as a comparison to the higher-purity commercial salt. Both salts have been previously characterized [Sulejmanovic 2021]. The capsules were exposed in a box furnace for 100 h at 700°C. The time was reduced in this experiment from 500 h to allow the glovebox test to be completed during the work week. The experimental details are summarized in Table 5-1.

5.1.2 Crucible Test

Crucibles (80 ml capacity) were used in this experiment and three 316H specimens (1.5 x 6.5 x 12.5 mm) were attached to a Mo wire and suspended close to the bottom of the crucible, Figure 5-1. While in the glovebox, the two crucibles were loaded with salt and placed in a 304 stainless-steel vessel (15 cm diameter x 20 cm tall) with a flange that can be bolted shut with a Cu gasket, Figure 5-1. Once the vessel was shut, the vessel was removed from the glovebox and placed in a box furnace for the 100 h/700°C isothermal exposure. The experiment details are summarized in Table 5-1.

Table 5-1. Task 2 test matrix showing the V/SA ratios for three test methods

	Test conditions	Commercial FLiNaK	Laboratory FLiNaK
1	Welded Capsule	1 small coupon (5.6 V/SA) 24g salt, 2.1cm ² SA	1 small coupon (5.8 V/SA) 24g salt, 2.1cm ² SA
2	Glovebox	1 medium coupon (5.5 V/SA) 63g salt, 5.7cm ² SA	1 medium coupon (5.5 V/SA) 63g salt, 5.7cm ² SA

3	Crucible	3 small coupons (5.4 V/SA) 72g salt, 3 x 2.2cm ² SA	3 small coupons (5.6 V/SA) 72g salt, 3 x 2.2cm ² SA
---	----------	---	---

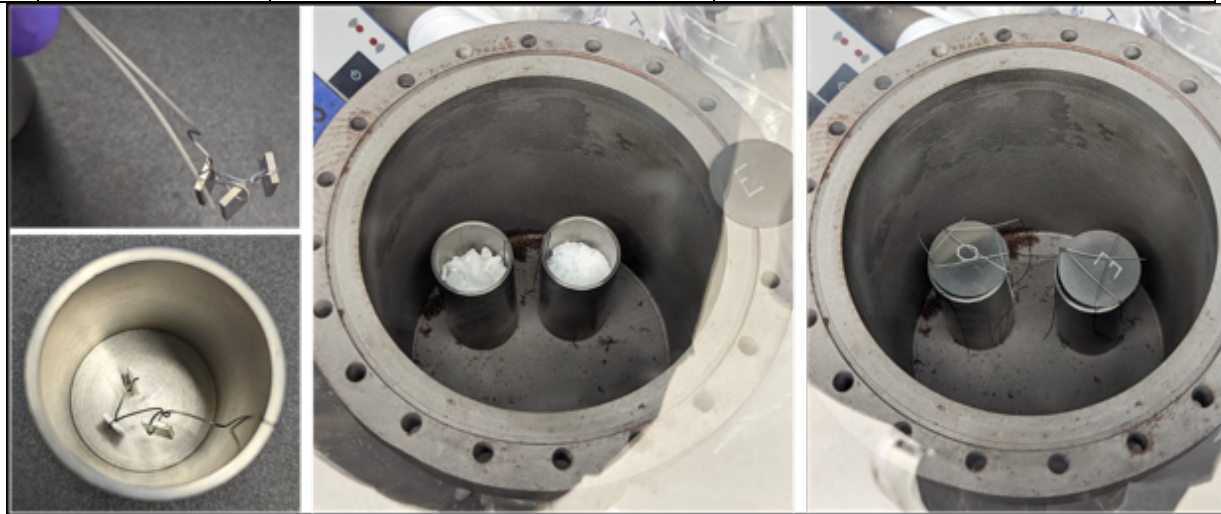


Figure 5-1. A picture of the experimental setup for the crucible test to assess compatibility of alloys in molten salts.

5.1.3 Glovebox Test

The crucible tests inside the glovebox were done in 40 ml molybdenum crucibles with one larger 316H specimen (1.5 x 12 x 20 mm) per crucible and three crucibles tested at a time. The specimens were attached with Mo wire and suspended close to the bottom of each crucible. Additional Mo wires for electrodes were added to one of the crucibles in each test, Figure 5-2. Prior to the start of the test in the glovebox, the oxygen and moisture content inside the glovebox were at <0.1 ppm O₂ and <0.1 ppm H₂O. The experiment details are summarized in Table 5-1.

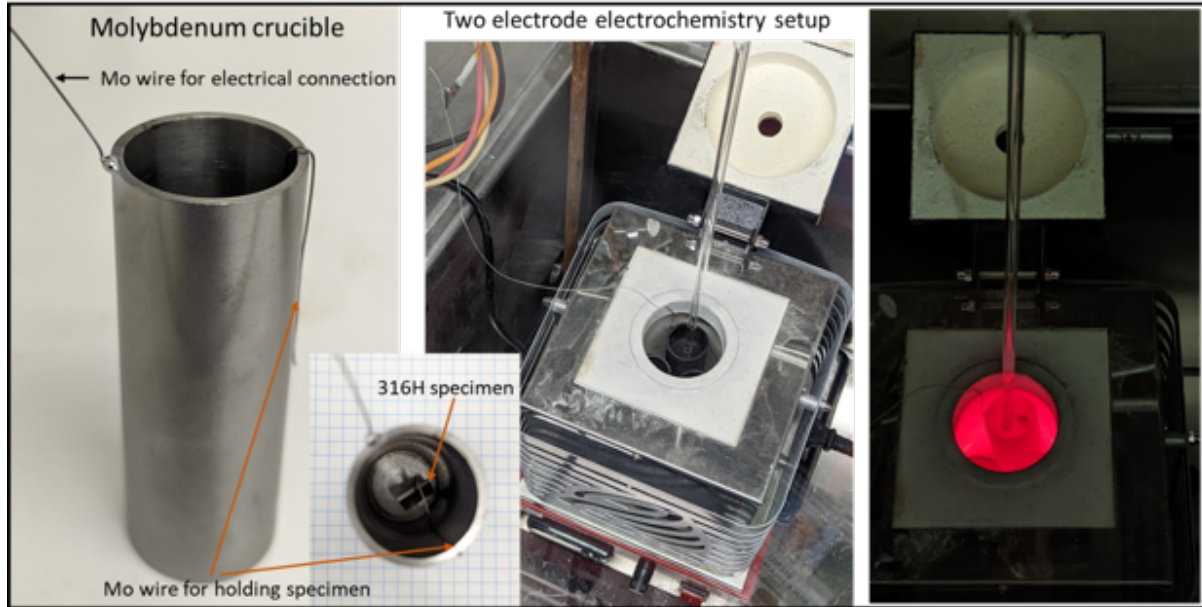


Figure 5-2. A picture showing the glovebox crucible test with electrochemistry setup.

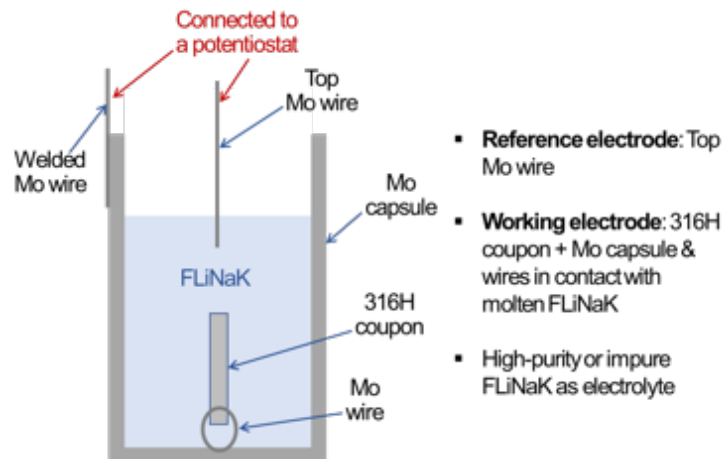


Figure 5-3. Schematic of the electrochemical measurement configuration used during the glovebox tests.

The electrochemical potentials of the 316H coupon and Mo capsule were recorded. The top Mo wire was used as a reference electrode, and the 316H coupon surface, the Mo inner wall and the wires acted as the working electrode (Figure 5-3). Measurements were made using a Gamry Reference 600+ potentiostat. The Mo wire only served as a pseudo-reference electrode from the Pt and molten salt interface and it was assumed that possible differences in the reference potential reading between the two salts could be ignored.

5.2 RESULTS

Figure 5-4 summarizes the mass change data for each test method in the two FLiNaK salts. The bars show the average mass loss for the three specimens (individual results are shown as black dots in each case) and the whiskers show one standard deviation. As expected, the mass losses were higher in the laboratory salt

with higher impurities, Table 4-1. For the lower purity commercial salt, the mass losses were very similar in the capsule and crucible tests with low variability. For the laboratory salt, the mass losses were lower in the crucible experiment where all three specimens were in the same Mo crucible. For both salts in the glovebox test, the mass gains were higher with more variability than in the sealed crucible and capsule experiments with a static Ar environment. The glovebox test was the only experiment where the test was conducted in a dynamic Ar environment.

The laboratory FLiNaK test was done first. During the initial heating, the moisture content jumped to ~7 ppm. After about an hour, the moisture content dropped back to <0.1 ppm starting point but the oxygen content increased to ~16 ppm. Between experiments, the oxygen content did not drop and the second experiment with commercial FLiNaK was done with the H₂O content <0.1 ppm but the oxygen remained near 16 ppm for the duration of the second 100 h test. Heating of the commercial FLiNaK did not result in an increase in the H₂O or O₂ content.

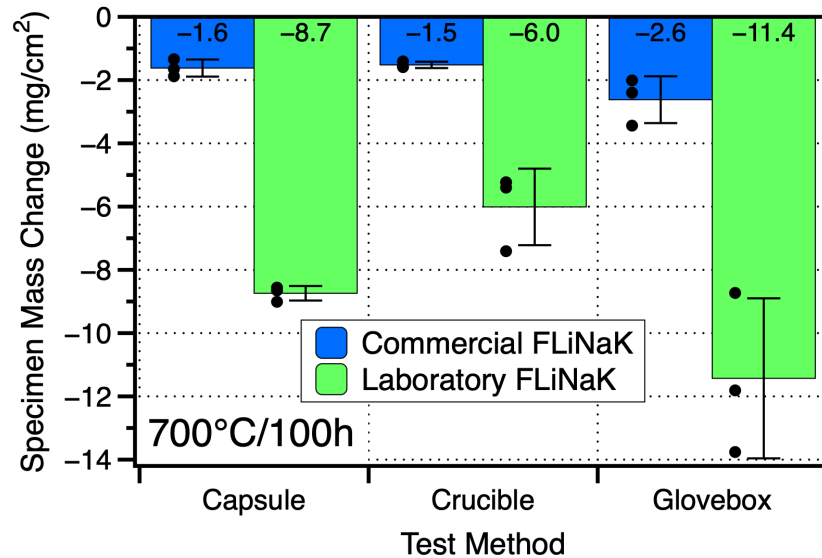


Figure 5-4. Mass change data of 316H specimens exposed in commercial and laboratory FLiNaK using three different exposure methods. The bars show the average of three specimens (dots) and the whiskers show one standard deviation.

Figure 5-5 shows the electrochemical potential curves for the two salts during the 100-h exposures with 316H specimens in the glovebox. Also included is a baseline test run with a Mo specimen and commercial FLiNaK salt.

Figure 5.6 shows representative metallography results from the three experiments and two salts. Note the difference in magnification for the limited attack observed in the commercial FLiNaK salt, Figures 5.6a-c,

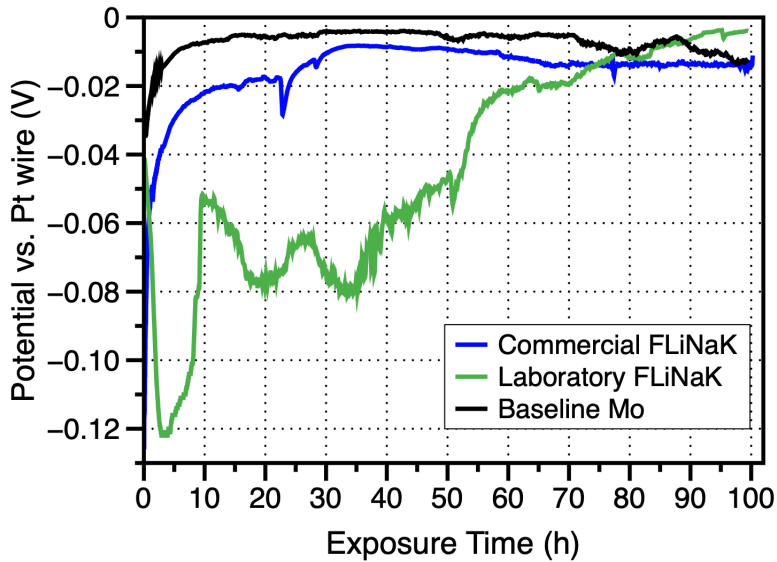


Figure 5-5. Corrosion potential transients measured from 100 h exposures in two FLiNaK salts.

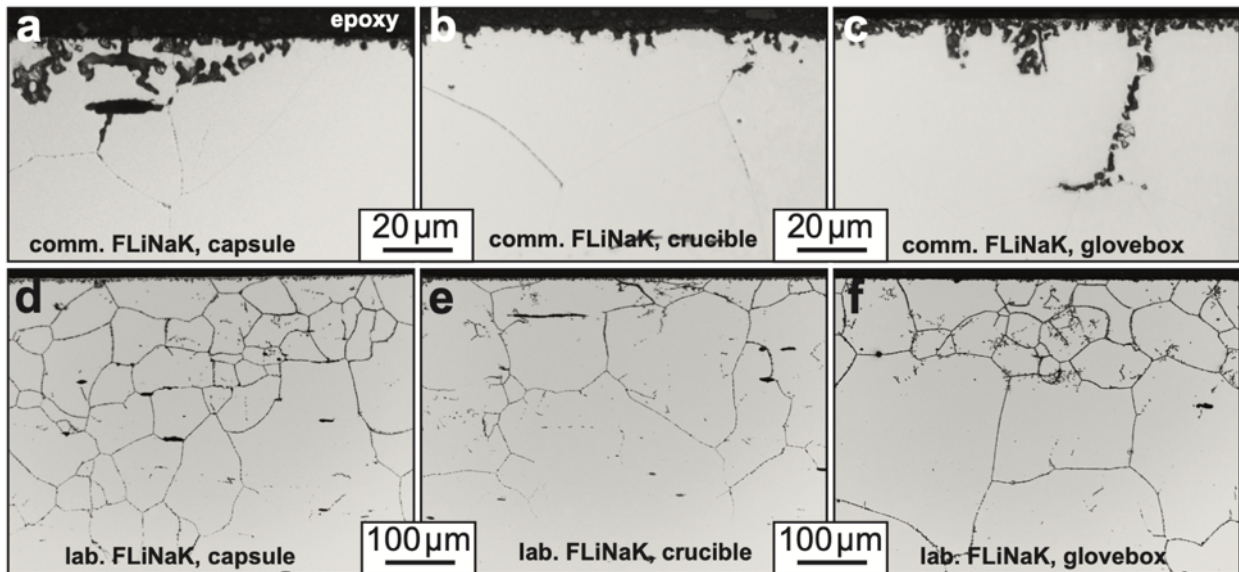


Figure 5-6. Light microscopy of the 316H specimens exposed for 100 h at 700°C in (a-c) commercial FLiNaK and (d-f) laboratory FLiNaK using (a,d) capsules, (b,e) crucibles and (c,f) glovebox

and the lower magnification for the much deeper attack observed with the laboratory salt, Figures 5.6d-f. The attack is consistent with the mass changes in Figure 5.4 and is quantified in Figure 5.7. For the commercial salt, the depth of attack was similar in each environment, although one capsule experiment showed an unusually large attack, which is why the experiments are conducted in triplicate. Similarly for the laboratory FLiNaK salt, the much deeper depth of attack was similar in each experiment.

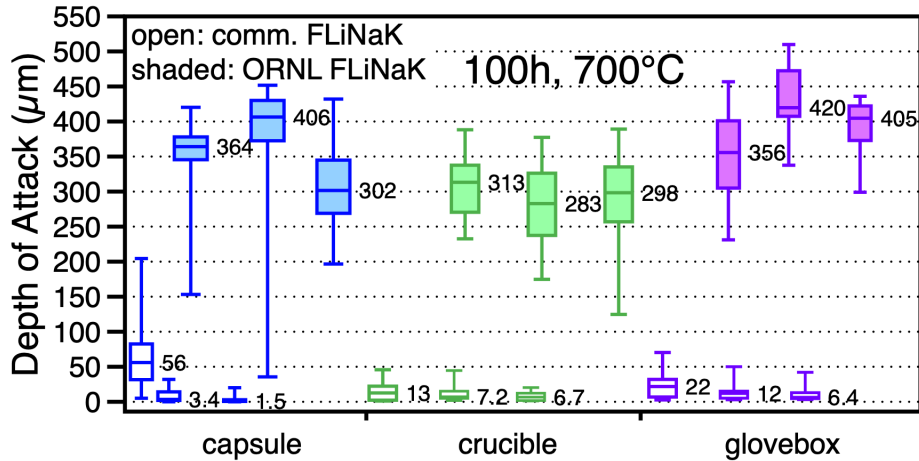


Figure 5-7. Box and whisker plots of the depth of attack based on the light microscopy images of selected specimens exposed to FLiNaK salt for 100 h at 700°C using three different methods. The median values are shown and the boxes are defined by the 25% and 75% values. The whiskers show the minimum and maximum values measured.

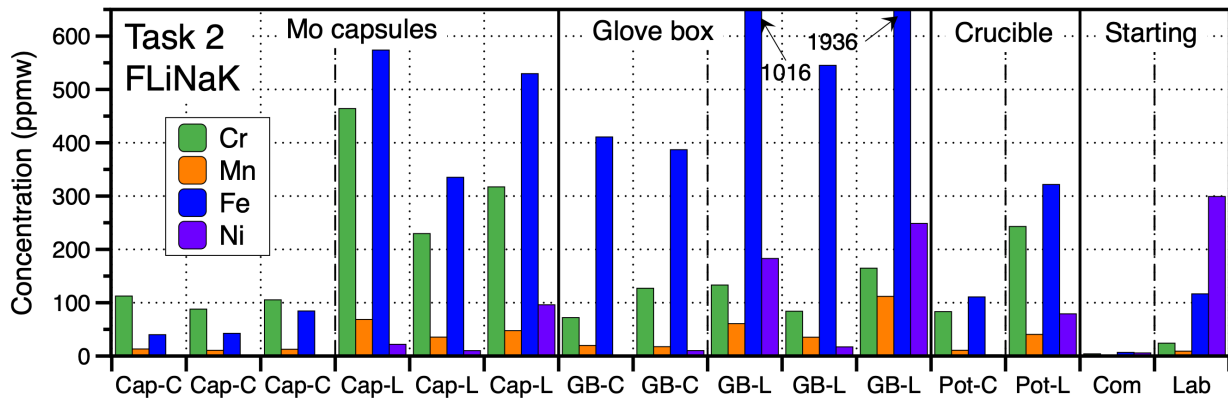


Figure 5-8. Pre- and post-test metallic salt impurities measured by ICP-OES in the commercial (C) or laboratory (L) FLiNaK salt in the capsule (cap), glovebox (GB) and crucible (pot) experiments.

Figure 5-8 show the pre- and post-test salt chemistry measured using inductively coupled plasma-optical emission spectroscopy (ICP-OES). The chemistry helps explain the reactions observed and gives more insight into the mass change. One reason the laboratory FLiNaK salt was more corrosive was because of the 300 ppm Ni in the salt. The less stable NiF_2 in the salt reacts to form other compounds such that the Ni content in the laboratory salt is lower after testing. This is especially true in capsule and crucible experiments where the highest Cr contents were observed after the experiments with the laboratory salt. In the glove box exposure, very high Fe contents were observed after the experiment. This was also the case in the commercial salt. For the commercial salt, the Cr and Fe contents in the salt were higher after the capsule and crucible tests compared to the starting salt which had very low impurity levels (all <10 ppmw). As noted, in the glovebox test, the Cr contents were similar to the other experiments but much higher Fe contents were measured.

5.3 DISCUSSION

These experiments were designed so that the V/SA ratios shown in Table 5-1 were very similar in each case. Average V/SA values are shown based on slight variability in the amount of salt and specimen

surface area in each experiment. These differences would not be expected to change the results significantly. The most significant difference among the three experiments was the higher mass losses in the glovebox tests. The larger mass loss for the glovebox exposures may be because the tests were performed with crucibles open to the glovebox environment during the 100 h exposures. The depth of attack results in Figure 5-7 do not show significantly deeper attack after exposure in the glove box. However, the salt chemistry results in Figure 5-8 indicate that more Fe was dissolved in these exposures which explains the larger mass loss. The commercial (high purity) salt experiment was conducted with a higher oxygen content in the glovebox argon than the starting oxygen content for the first experiment with laboratory salt. Heating the laboratory salt in the glovebox disrupted the environment for an extended time. It is not known if this could affect the results by the 2nd (commercial) salt getting oxygen from the environment during the 100 h exposure.

Another point to note is that the crucible test was more like the capsule test because the secondary SS container was bolted shut. In some tests reported in the literature, flowing argon is used as a cover gas in crucible tests making it more similar to the glovebox test.

The electrochemistry results in Figure 5-5 generally show the more corrosive laboratory salt with the most negative potential. A very small potential was observed for the Mo specimen in the high-purity commercial salt. This type of information could be used to verify the quality of salt batches but more characterization is needed to fully understand these observations including the change in potential with time. The advantage of the glovebox experiment is the ability to gather this type of information during the exposure.

In general, there was larger variability in the mass loss results in the laboratory (high impurity) FLiNaK. This may be attributed to an inhomogeneity of impurities present in individual pieces of solid salt placed into each crucible/capsule. This has not been confirmed by testing multiple pieces of solid salt from this batch of salt before testing. However, Figure 5-8 shows considerable variation in the post-test impurities which might result from variations in the pre-test chemistry.

5.4 SUMMARY

This experiment compared two batches of FLiNaK in three different salt exposure experiment methods. The higher purity FLiNaK resulted in less mass loss and less depth of attack after 100 h exposures at 700°C. For both salts, the mass losses were higher in the glovebox experiment where the salt was exposed to the argon environment and may have reacted with impurities in the argon. For both salts, higher Fe impurities were found in the salt exposed in the glovebox. For the low purity laboratory salt, the oxygen and water vapor monitors increased when the salt was heated suggesting that the salt gave off O₂ and H₂O when heated. The results for the capsule and crucible experiments were very similar as both followed a similar strategy of individual containers for each specimen and a static gas environment (i.e. no flowing cover gas).

Ultimately, the selection of experimental parameters is always a tradeoff and these experiments were selected to explore some of those issues. Especially for longer duration and higher temperature exposures, there is a greater risk of contaminating the salt when the salt container is not sealed. However, sealing the container requires more expense and prevents in-situ monitoring.

6. COMMENTS ON CHARACTERIZATION (TASK 8)

Based on work over the past five years, understanding of molten salt compatibility seems to be maximized by a combination of:

- (a) Specimen mass change
- (b) Post-exposure microstructure characterization
- (c) Pre- and post-exposure salt chemistry
- (d) Electrochemistry

Specimen mass change is straightforward, normalized for the specimen surface, it is normally reported in units of mg/cm^2 . Mass change is not always reported or measurable if a coupon is not used. However, if it is not reported then that makes it more important that microstructure and salt chemistry are reported. Some studies convert results to rates (e.g., $\mu\text{m}/\text{yr}$) but these rates assume a rate law that is not established and sometimes calculate μm based on converting mass loss using the alloy density. Particularly for static tests, mass change measurements almost always decrease with time which may be due to changes in salt chemistry with time that are not representative of application conditions. The reaction also may become limited by diffusion in the alloy substrate. Converting directly from mass change to depth of attack does not consider selective attack of one or more alloying elements that may lead to a porous reaction product rather than uniform dissolution.

Sections 3, 4 and 5 show standard light microscopy and SEM/EDS characterization of the specimens exposed in these experiments. In some cases, it was difficult to characterize the reaction product because they were thin or contained many light elements. Higher resolution characterization techniques like transmission electron microscopy were not used in this study. These techniques may be better suited for mechanistic studies. It could be argued that small depths of attack mean relatively good compatibility and no further characterization is needed. Additional techniques for capturing depth profiles include glow discharge optical emission spectroscopy (GDOES), which also was not used in this study. For identifying light elements, electron probe microanalysis (EPMA) using wavelength dispersive spectroscopy (WDS) with standards can be more effective.

At the start of the project, it was hoped that 3-dimensional characterization might be employed to better understand the resulting porous microstructure. Focused ion beam (FIB) systems can perform serial sectioning but the volume is relatively small. A Robomet performs serial sectioning by polishing and imaging successive layers through a specimen to create a 3D reconstruction. However, the Robomet at ORNL was not functional during this project.

Salt chemistry before and after experiments is very useful in identifying which elements are dissolving into the salt. It also can identify issues with the container material if evidence of the container dissolving is found. While the literature often focuses on Cr dissolution into the salt, chemistry measurements show that after 316H exposures, Cr, Mn and Fe are all found in the salt. Examples were shown in Figure 4-7, 4-27, 4-45 and 5-8. Another example is shown in Figure 6-1 for FLiNaK salt after a 1000 h flowing test in 316H stainless steel with a peak temperature of 650°C .

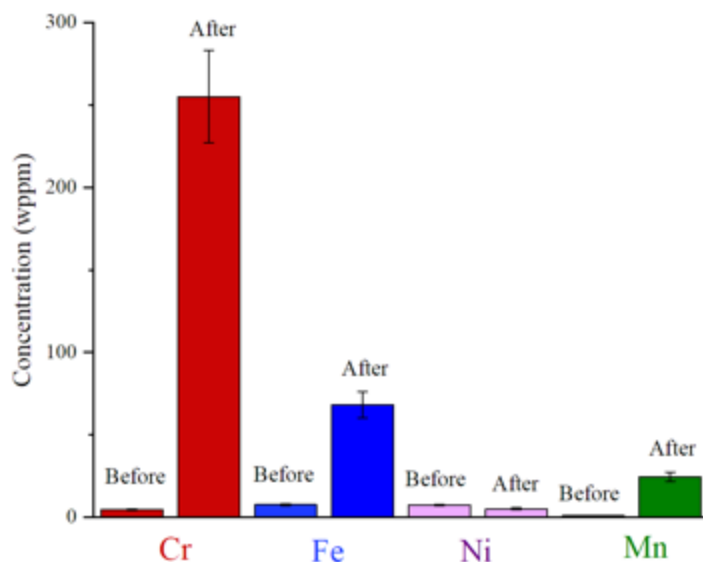


Figure 6-1. Concentration of metallic species in FLiNaK salt before and after flowing for 1000h in the 316H TCL. [Raiman 2022].

Electrochemistry also might be used to characterize the salt before, during and after static or flowing experiments with an example shown in Figure 5-5. However, standards have not been published to, for example, determine salt purity or identify impurities in the salt. This is an area where proprietary industry data may be available but individual electrochemistry reports in the literature have not yet resulted in a clear methodology for using this technique. It also has been difficult to convert electrochemistry data to long-term rates of attack. More work may be needed to develop standards and compare results to other methodologies.

The current state of knowledge about chemical interactions between molten salts and structural metals is that multivalent cationic species exist with different solvation shell structures which are strongly dependent on the type and amounts of available halide species, and on the chemical nature of other cations in the melt. The extremely low fraction of species reacting in the boundary regions between phases or molecular regions together with the non-equilibrium reaction kinetics, make detailed analyses of the relevant physical processes extremely challenging. Despite the advances discussed in the previous section, identifying speciation of transition metals in molten alkali/alkali earth halides during high temperature exposures remains an extremely challenging task and there is currently no conclusive evidence for the different complexes existing in the melt or enough knowledge of their proportions as a function of composition and temperature.

In-situ characterization efforts to identify reaction products in molten salts have primarily focused on detecting changes in the molten salt chemistry while some studies have looked at the speciation of metal-salt complexes that have formed. Common goals of these investigations were to identify the nature of chemical complexes in the melt and coordination nature of first neighbors around cations and anions. [Bessada 2007,2009,2010,2017, Lacassagne 2002, Matsura 2009, Okamoto 2001, Rollet 2008, Smith 2019, Watanabe 2006]. The main characterization techniques employed to study salt metal interactions were Raman spectroscopy, Nuclear Magnetic Resonance (NMR) and Extended X-ray Absorption Fine Structure (EXAFS). Raman spectroscopy is limited in that it requires sufficiently high concentrations of species and is unable to provide information on interionic distances; both these limitations can be overcome by NMR and EXAFS. EXAFS is a powerful tool to analyze local structures of materials at high temperatures and transient states, and its applicability to a variety of systems is being explored, e.g., to

obtain structural information on systems containing nuclear materials and to elucidate the mechanism of in situ electrochemical and/or redox reactions by following their temporal and spatial variations. Note that EXAFS is generally collected using a high energy X-ray beam, the source of which is often a synchrotron; hence EXAFS data is not easily obtained.

Recent promising developments have combined X-ray spectroscopy with molecular dynamics simulations to overcome the complications in modeling the spectra of highly disordered molten melt [Moon 2019, Wu 2019]. Structural parameters (coordination number, first neighbors and distances) in the liquid state were extracted from molecular dynamics calculations based on the polarizable ionic model (PIM). This enabled adjustment of fine structure spectra calculated by the FEFF code [Rehr 2000,2010] with experimental data. It allowed generating the trajectories of ions via classical molecular dynamics calculations inside a periodically replicated simulation cell, and then extracting the relevant physicochemical properties of the melt. The interaction potential consists of a sum of pairwise additive interactions supplemented with a many-body polarization term. To determine forces and dipoles of each ion, the first principles electronic structure was calculated for a given system using the plane waves density functional theory (DFT) formalism. Parameters of the potential are then obtained by minimizing the difference between the forces and dipoles predicted by the model to the first principles calculated ones.

The relation between salt chemistry and alloy composition is not well understood. Identifying local structure and coordination numbers of metal halide complexes will provide vital clues to the alloying elements participating in corrosion reactions and interfacial reactions. There is a need to develop techniques to observe and quantify salt-metal reactions with spectroscopic and neutron scattering techniques. Raman spectroscopy and pair-distribution function (PDF) analysis of neutron diffraction data will elucidate the local structure of the corrosion products whereas a combination of neutron reflectometry and X-ray Absorption Near Edge Spectroscopy (XANES) techniques can be employed to probe short and intermediate range correlations and identify structures of corrosion products during exposure of the chosen binary and ternary model alloys (Fe-Cr, Ni-Cr, Fe-Cr-Ni) in molten salts. XANES data is often collected along with EXAFS data and is a powerful technique to identify oxidation state information of an element. It is simultaneously important to understand the role of alloying elements (Mn, Al, Ti, C) in changing subsurface chemistry, phase transformations and driving forces. Identification of metal-halide complexes will build toward an understanding of the non-equilibrium interfacial kinetics at a multicomponent salt-alloy interface and help develop insights into the interdependence of salt and alloy chemistry and how this governs corrosion processes and subsurface microstructural changes.

7. EXAMPLE DATA COMPARING FLOWING AND STATIC EXPERIMENTS

Several recent experiments compared results in static isothermal conditions to flowing conditions with a temperature gradient but the data set is small. As noted earlier, static experiments are much easier to conduct but flowing experiments are more relevant to operational conditions and allow material down selections for further development. One of the key issues with working fluids like molten salts and liquid metals is that dissolution of structural materials can result in mass transfer where material dissolved in the hot section deposits in a colder region. If the deposition is significant, a catastrophic blockage could occur. Koger [1974] showed graphic examples of reaction products blocking flow in a TCL experiment using Na-B-K fluoride salt and Hastelloy N tubing. Despite other attractive features, this particular salt was not further explored because of these compatibility issues, especially with Hastelloy N which was developed to be compatible with FLiBe salt and used for the Molten Salt Reactor Experiment (MSRE) [Haubenreich 1970] at ORNL. In order to study mass transfer, a flowing salt in a temperature gradient is needed.

Figure 7-1 highlights a difference between static and flowing experiments. This study used the same commercial purified FLiNaK salt as was used in section #5 [Raiman 2022]. Typical of most static capsule tests mass losses were observed at both 550° and 650°C exposures for 316H specimens in 316H specimens. Comparing the static and flowing results, the mass changes are all similar in magnitude. However, in the flowing TCL experiment, a mass gain was observed in the cold leg (550°C) due to mass transfer (Fe was detected at the specimen surfaces). The complete mass change data from the TCL experiment is shown in Figure 7-2. Chains of 20 type 316H specimens were exposed in the hot and cold legs. Figure 7-2 also shows results for a FLiBe TCL [Pint 2022a] with very similar conditions as the FLiNaK TCL experiment. All of the specimens and TCL tubing were 316H in both experiments. In both TCL experiments, increased mass loss was observed at 650°C compared to the static experiment. The static FLiBe experiment results are also shown in Figure 7-2. In the FLiBe experiment, issues with cleaning the specimens may have increase the mass loss in the cold leg. These are just two recent examples but it is important to be cognizant of the potential differences observed in static and flowing salt experiments and the limitations of the static test.

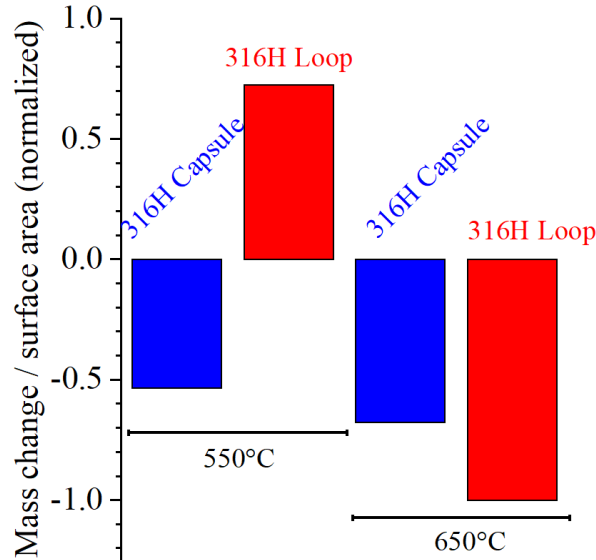


Figure 7-1. Normalized mass change of 316H samples exposed to FLiNaK salt for 1000 h in capsules or a TCL. Actual temperatures of the loop specimens were 552°C and 647°C.

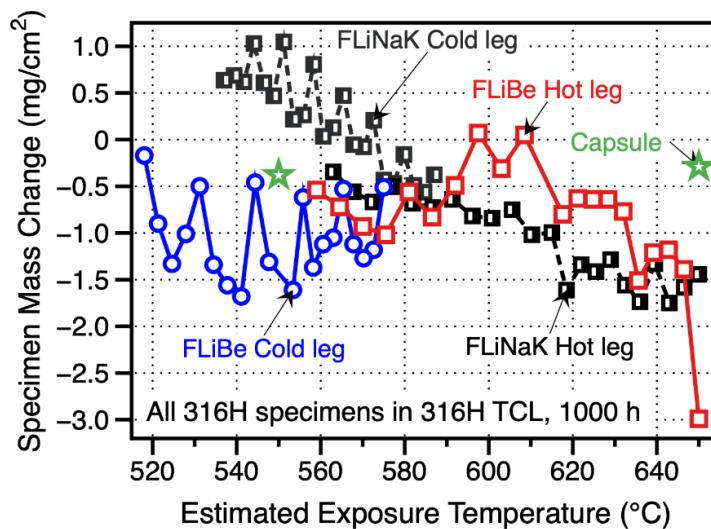


Figure 7-2. Specimen mass change of 316H specimens as a function of estimated exposure temperature in flowing FLiBe salt compared to values for FLiNaK salt after 1,000 h. The capsule mass change values are shown as stars [Pint 2022a].

Traditionally, static tests were used as screening experiments followed by TCL experiments to verify adequate compatibility before moving to more expensive forced convection experiments [Vreeland 1953]. Currently, the majority of testing reported in the literature is static testing and relatively few flowing experiments are reported.

A recent paper [Kelleher 2022] from TerraPower LLC, described the operation of ~49 thermal convection ‘microloops’ to test compatibility of Cl salts as well as an extensive review of the molten salt compatibility literature. The term microloops refers to the 6.4 mm (0.25”) diameter, 0.89 mm wall thickness tubing and ~0.5 m height used compared to 25.4 mm tubing and ~1 m height used with ORNL

TCLs mentioned above [Raiman 2022, Pint 2022a, 2022b]. Combining the smaller dimensions, the volume of salt is minimized to better enable the testing of fuel salts (which was mentioned, but no results were provided [Kelleher 2022]). Collectively these experiments have generated over 9 years of flowing data (>79,000 h) on nine different alloys using both NaCl-MgCl₂ and eutectic NaCl-MgCl₂-KCl salt (385°C melting point). Because of the small tubing, no specimens can be placed in the microloop (see Figure 7-2) so characterization of the tubing wall is the only corrosion performance metric and salt chemistries were not reported after testing. In addition, because the starting tubing wall thickness varied by -12.5%/+20% the loss in wall thickness could not be accurately determined and only the thickness of the reaction zone (e.g. depth of Cr depletion) could be measured which the author notes does not capture uniform dissolution. Thus, no reaction rate data was provided for alloy 200 and 201 Ni tubing because there was no reaction product to characterize. The reported depth of attack results are summarized in Figure 7-3. The authors reported that microloops are sensitive to corrosion and plugging due to mass transfer and many tests were terminated due to plugging of the loop after <1,000 h. Even Ni tubing (alloy 200 or 201) resulted in Ni crystals forming in the cold leg and restricting flow. As with all salt studies, salt purification was an issue and nominally better results were obtained when the salt was purified using Mg additions to the salt at 700°C [Kelleher 2022], shown as closed symbols in Figure 7-3.

Alloy N tubing was significantly attacked without salt purification resulting in short loop run times shown by the open red diamonds in Figure 7-3. Alloy N performance improved in Mg purified salt (clogging after ~8,300 h) but because of the poor performance of alloy N, additional loops of Ni-based, Mo-containing alloys 617, 625 and C276 also were evaluated for comparison. Both 316L and 316H variations were

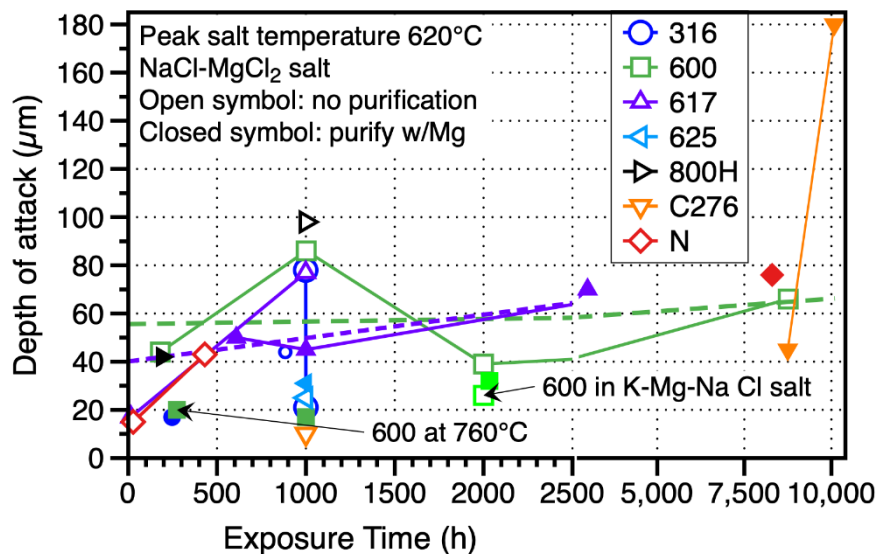


Figure 7-3. Measured depth of attack on alloy tubing exposed to flowing Cl salt as a function of exposure time with some tests stopped due to plugging of the loop. Most of the tests were run with NaCl-MgCl₂ (58-42 mol.%) at a peak temperature of ~620°C and a temperature gradient of >100°C. The open symbol tests used unpurified salt while the closed symbols were given a heat treatment with a Mg getter. Adapted from [Kelleher 2022] table of data.

evaluated. None of these loops ran beyond 1000 h because of significant attack. Changes in microloop temperature profiles were used to identify potential plugging of the loop with reaction products which required some tests to be stopped in < 1000 h. Readily available Ni-based alloy 600 was the most heavily studied material and did show reduced attack when the salt was purified, closed green square symbols, including one test at 760°C, Figure 7-3. Numerous examples were shown of mass transfer and deposition of reaction products on the cold leg of microloops. The use of Mg additives to the salt as a redox agent (as was done in section 4) was not discussed. Based on the experience with four ORNL Cl salt TCL's the

results may have been significantly different if the salt had been purified or dried and Mg added to the salt (0.04wt.%) [Pint 2022b].

The next step in the progression of understanding compatibility is moving from TCL experiments to more prototypical conditions in a forced circulation or pumped loop. Forced-circulation loops were employed during the 1950's Aircraft Reactor Experiment with a maximum fuel temperature of 871°C (1600°F) and a maximum wall temperature of 927°C (1700°F) [Manly 1957]. Comparison of the results obtained from TCLs with the data obtained from forced-circulation loops showed that the flow rate had a very minor effect on the corrosion of Ni-based alloy 600 by the NaF-ZrF-UF₆ (50-46-4 mole %) fuel salt. Furthermore, the forced-circulation loops were operated at different flow velocities to evaluate the impact of increased flow velocities on corrosion. Based on the limited scatter observed in the corrosion data and a lack of correlation between flow rates and depths of attack, it was concluded that flow velocities (in the investigated range of Reynolds numbers from 5,000-15,000, proportional to velocity) had a negligible effect on corrosion.

In summary, static tests are the start of the experimental process to evaluate salt compatibility. The subsequent steps are a progression towards more prototypic application conditions including peak temperature, temperature gradient, salt velocity and geometry. While static tests focus on compatibility (i.e. salt corrosion), as the experiments progress in complexity, typically compatibility becomes less of a concern and broader system functionality is the focus including sensors, inline purification and exploring off-normal and accident scenarios.

8. RECOMMENDATIONS ON EVALUATING COMPATIBILITY DATA

This set of experiments and supporting information is an attempt to lay out recommendations for how to interpret corrosion data, especially because there are no available standards for such experiments. Several factors are important to take into account with questions included to consider:

1. Static vs. Flowing tests: Section #7 outlined that flowing experiments, especially in a temperature gradient, should provide more relevant information than static experiments.
2. Salt chemistry: Have impurities been quantified or additives made? Also, consider whether impurity evolution has been measured during experiments. Are ranges specified for salt purity during operation?
3. Experiment container: Is this the same as the structural material? If different, is it impacting the experiment? Has adequate characterization been used to assess and quantify the impact?
4. Environment. Is the environment static (e.g., sealed) or is a flowing gas present? Is the test environment prototypical of operation? Could the experimental environment contribute impurities to the salt as a function of time? Has the potential for contamination been quantified?
5. Temperature: Are experimental temperatures relevant to operation? Do they capture the expected temperature range in the salt during operation? Do the experiments consider off normal or accident conditions? How will temperature impact compatibility?
6. Time: Are experimental times relevant to operation? How has time evolution been considered? In a static environment, can the reaction be limited because equilibrium is approached, thereby inhibiting the reaction? Has modeling been verified? (Modeling will be addressed in a subsequent report.)

A repeated point of emphasis is that some combination of assessments is needed to produce a comprehensive understanding of salt compatibility including specimen mass change, depth and type of attack, changes in salt chemistry and changes in electrochemical potential.

8.1 HOW TO EVALUATE TECHNOLOGIES

During exposure of a structural material in molten halide salts, multiple corrosion mechanisms such as galvanic corrosion, anodic dissolution, impurity driven corrosion, and thermal gradients might be simultaneously active [DeVan 1969, Ozeryanaya 1985]. Experimental evaluations under realistic test conditions are essential to evaluate compatibility of the candidate materials during exposures in molten salts. Quantitative effects of salt chemistry and temperature on the salt chlorine/fluorine potential during the interaction with multicomponent alloys are not well established. Ultimately, the lack of a standard procedure for testing corrosion in molten salts results in non-representative mass change measurements which complicates quantifying the extent of corrosion damage. The main variables resulting in discrepancies of reported corrosion rates are a lack of consistency in salt chemistry (different purification

procedures), use of different container materials (dissimilar capsule/test material combinations and variations in the V/SA ratio) and employing distinct test procedures (capsule/loop tests).



9. ACKNOWLEDGEMENTS

The authors would like to thank C. Parker, A. Willoughby, B. Johnston, T. Lowe, V. Cox and C. O'Dell for assistance with the experimental work. This research was funded by the US Nuclear Regulatory Commission.

10. REFERENCES

- C. Bessada, et al. (2007) "Lanthanide and actinide speciation in molten fluorides: A structural approach by NMR and EXAFS spectroscopies," *Journal of Nuclear Materials*, 360, 43-48.
- C. Bessada, et al. (2009) "High temperature NMR approach of mixtures of rare earth and alkali fluorides: An insight into the local structure," *Journal of Fluorine Chemistry*, 130, 45-52.
- C. Bessada, et al. (2010) "In situ experimental approach of the speciation in molten lanthanide and actinide fluorides combining NMR, EXAFS and Molecular Dynamics," *Molten Salts and Ionic Liquids* 17, 361-369.
- C. Bessada, et al. (2017) "High temperature EXAFS experiments in molten actinide fluorides: The challenge of a triple containment cell for radioactive and aggressive liquids," *Journal of Nuclear Materials* 494, 192-199.
- K. Britsch, M. Anderson, P. Brooks, K. Sridharan, "Natural circulation FLiBe loop overview," *International Journal of Heat and Mass Transfer* 134 (2019) 970–983.
- G.-S. Chen, I-W. Sun, K. D. Sienerth, A. G. Edwards and G. Mamantov (1993) "Removal of Oxide Impurities from Alkali Haloaluminate Melts Using Carbon Tetrachloride," *J. Electrochemical Soc.* 140, 1523-1526.
- H. S. Cho, J. W. Van Zee, S. Shimpalee, B. A. Tavakoli, J. W. Weidner, B. L. Garcia-Diaz, M. J. Martinez-Rodriguez, L. Olson, J. Gray (2016) "Dimensionless Analysis for Predicting Fe-Ni-Cr Alloy Corrosion in Molten Salt Systems for Concentrated Solar Power Systems," *Corrosion* 72, 742–760.
- O. K. Chopra, D. L. Smith, P. F. Tortorelli, J. H. DeVan and D. K. Sze (1985) "Liquid Metal Corrosion," *Fusion Technology*, 8, 1956-69
- J. H. DeVan, R. B. Evans, III (1962) "Corrosion behavior of reactor materials in fluoride salt mixtures," Report ORNL-TM-328, Oak Ridge National Laboratory, Oak Ridge, TN.
- J. H. De Van (1969) "Effect of Alloying Additions on Corrosion Behavior of Nickel- Molybdenum Alloys in Fused Fluoride Mixtures," Report ORNL/TM-2021/1, Oak Ridge National Laboratory, Oak Ridge, TN.
- J. H. DeVan, "Compatibility of Structural Materials with Fusion Reactor Coolant and Breeder Fluids," *J. Nucl. Mat.*, 85-86 (1979) 249-256.
- W. Ding, H. Shi, A. Jianu, Y. Xiu, A. Bonk, A. Weisenburger, T. Bauer (2019) "Molten chloride salts for next generation concentrated solar power plants: Mitigation strategies against corrosion of structural materials," *Solar Energy Materials and Solar Cells* 193, 298–313
- L. F. Epstein (1957) "Static and Dynamic Corrosion and Mass Transfer in Liquid Metal Systems," *Liquid Metals Technology, Chem. Eng. Prog. Symp. Ser.* 20, 53 67-81.
- C. Falconer, M. Elbakhshwan, W. Doniger, M. Weinstein, K. Sridharan, A. Couet (2022) "Activity gradient driven mass transport in molten fluoride salt medium," *npj Materials Degradation* 6 (2022) 29.
- J. Feng, L. Mao, G. Yuan, Y. Zhao, J. Vidal, L. Liu, "Grain size effect on corrosion behavior of Inconel 625 film against molten MgCl₂-NaCl-KCl salt," *Corrosion Science* 197 (2022) 110097.
- C. Guminski and H. U. Borgstedt, "Solubility of Vanadium in the Liquid Alkali Metals Lithium and Sodium," *Z. Metallkd.* 85 (1994) 771-774.

- S. Guo, J. Zhang, W. Wu, W. Zhou (2018) “Corrosion in the molten fluoride and chloride salts and materials development for nuclear applications,” *Progress in Materials Science* 97, 448–487
- P. N. Haubenreich and J. R. Engel (1970) “Experience with the Molten-Salt Reactor Experiment,” *Nuclear Applications and Technology*, 8(2), 118-136. DOI: 10.13182/NT8-2-118.
- ISO standard 17245:2015 “Corrosion of metals and alloys — Test method for high temperature corrosion testing of metallic materials by immersing in molten salt or other liquids under static conditions,” (re-reviewed in 2020), www.iso.org/standard/59473.html
- B. C. Kelleher, K.P. Dolan, P. Brooks, M.H. Anderson, K. Sridharan (2015) “Batch-Scale Hydrofluorination of ${}^7\text{Li}_2\text{BeF}_4$ to Support Molten Salt Reactor Development,” *J. Nucl. Eng. Radiat. Sci.* 1, 041010
- B. C. Kelleher, S. F. Gagnon, I. G. Mitchell, Thermal Gradient Mass Transport Corrosion in NaCl-MgCl₂ and MgCl₂-NaCl-KCl Molten Salts,” *Materials Today Communications* 33 (2022) 104358.
- M. Kikuchi, M. Sakakibara, Y. Ootoguro, H. Mimura, S. Araki and T. Fujita, (1985) “An Austenitic Heat Resisting Steel Tube Developed for Advanced Fossil-Fired Steam Plants,” in *High Temperature Alloys, Their Exploitable Potential*, eds. J. B. Marriott, M. Merz, J. Nihoul and J. Ward, Elsevier, London, p.267-276
- J. W. Koger (1973) “Fluoride Salt Corrosion and Mass-Transfer in High-Temperature Dynamic-Systems,” *Corrosion* 29(3), 115-122.
- J. W. Koger (1974) “Corrosion Product Deposition in Molten Fluoride Salt Systems,” *Corrosion* 30 (4), 125-130.
- J. M. Kurley, P. W. Halstenberg, A. McAlister, S. Raiman, S. Dai and R. T. Mayes (2019) “Enabling chloride salts for thermal energy storage: implications of salt purity,” *RSC Adv.* 9, 25602-25608.
- V. Lacassagne, et al. (2002) “Structure of high-temperature NaF-AlF₃-Al₂O₃ melts: A multinuclear NMR study,” *Journal of Physical Chemistry B*, 106, 1862-1868.
- W. D. Manly, G. M. Adamson, Jr., J. H. Coobs, J. H. DeVan, D. A. Douglas, E. E. Hoffman, and P. Patriarca, “Aircraft Reactor Experiment–Metallurgical Aspects,” Technical Report ORNL-2349, Oak Ridge National Laboratory, Oak Ridge, TN 1957. doi:10.2172/4227617
- H. Matsuura, et al. (2009) “XAFS analyses of molten metal fluorides,” *Journal of Fluorine Chemistry*, 130, 53-60.
- R. T. Mayes, J. M. Kurley III, P. W. Halstenberg, A. McAlister, D. Sulejmanovic, S. S. Raiman, S. Dai and B. A. Pint (2018) “Purification of Chloride Salts for Concentrated Solar Applications,” Letter Report ORNL/LTR-2018/1052, Oak Ridge National Laboratory, Oak Ridge, TN.
- B. A. T. Mehrabadi, J. W. Weidner, B. Garcia-Diaz, M. Martinez-Rodriguez, L. Olson, S. Shimpalee (2016) “Multidimensional Modeling of Nickel Alloy Corrosion inside High Temperature Molten Salt Systems,” *Journal of the Electrochemical Society* 163, C830–C838.
- J. Moon, et al. (2019) “Application of In Situ X-ray Absorption Spectroscopy to Study Dilute Chromium Ions in a Molten Chloride Salt,” doi: 10.26434/chemrxiv.9959807.v1
- O. Muránsky, C. Yang, H. Zhu, I. Karatchevtseva, P. Sláma, Z. Nový, L. Edwards, “Molten salt corrosion of Ni-Mo-Cr candidate structural materials for Molten Salt Reactor (MSR) systems,” *Corrosion Science* 159 (2019) 108087.
- Y. Okamoto, et al. (2001) “X-ray absorption study of molten yttrium trihalides. *Journal of Synchrotron Radiation*, 8, 1191-1199.
- D. Olander (2002) “Redox condition in molten fluoride salts: Definition and control,” *Journal of Nuclear Materials* 300, 270–272
- L. C. Olson, R. E. Fuentes, M. J. Martinez-Rodriguez, J. W. Ambrosek, K. Sridharan, M. H. Anderson, B. L. Garcia-Diaz, J. Gray and T. R. Allen (2015) “Impact of Corrosion Test Container Material in Molten Fluorides,” *J. Sol. Energy Eng.* 137, 61007.
- I. N. Ozeryanaya (1985) “Corrosion of metals by molten salts in heat-treatment processes,” *Metal Science and Heat Treatment* 27, 184–188.

- C. G. Parker, D. Sulejmanovic, J. M. Kurley, S. S. Raiman and B. A. Pint (2022) “Investigating Test Parameters for Isothermal Salt Compatibility Experiments,” manuscript in preparation for NRC review.
- R. Pillai, W. Sloof, A. Chyrkin, L. Singheiser, W. Quadackers (2015) “A new computational approach for modelling the microstructural evolution and residual lifetime assessment of MCrAlY coatings,” *Materials at High Temperatures* 32, 57–67.
- R. Pillai, S. S. Raiman, B. A. Pint (2021) “First steps toward predicting corrosion behavior of structural materials in molten salts,” *Journal of Nuclear Materials* 543, 152755
- R. Pillai, D. Sulejmanovic, S. S. Raiman, B. A. Pint (2023) “Establishing a design strategy for corrosion resistant structural materials in molten salt technologies,” *JOM*, in press.
- B. A. Pint and K. A. Unocic (2013) “Pb-Li Compatibility Issues for DEMO,” *J. Nucl. Mater.* 442, 572-575.
- B. A. Pint, J. W. McMurray, A. W. Willoughby, J. M. Kurley, S. R. Pearson, M. J. Lance, D. N. Leonard, H. M. Meyer, J. Jun, S. S. Raiman and R. T. Mayes (2019) “Reestablishing the paradigm for evaluating halide salt compatibility to study commercial chloride salts at 600°-800°C,” *Materials and Corrosion*, 70, 1439-1449
- B. A. Pint (2020) “Progression to Compatibility Evaluations in Flowing Molten Salts,” ORNL Report ORNL/SPR-2020/1940, Oak Ridge, TN. doi.org/10.2172/1649281
- B. A. Pint, C. G. Parker, Y.-F. Su, D. Sulejmanovic, M. J. Lance and R. Pillai (2022a) “Assessing Stainless Steel Compatibility in Flowing Fluoride Salts,” in Proceedings of the 20th International Conference on Environmental Degradation of Materials in Nuclear Systems, paper ED2021-18337.
- B. A. Pint, J. M. Kurley, and D. Sulejmanovic (2022b) “Performance of alloy 600 in flowing commercial Cl salt at 600°-750°C,” AIP Conference Proceedings, 2445, 020011; presented at SolarPaces 2020, Sept. 2020.
- S. S. Raiman and S. Lee (2018) “Aggregation and data analysis of corrosion studies in molten chloride and fluoride salts,” *Journal of Nuclear Materials* 511, 523-535
- S. S. Raiman, R. T. Mayes, J. M. Kurley, R. Parrish and E. Vogli (2019) “Amorphous and partially-amorphous metal coatings for corrosion resistance in molten chloride salt,” *Solar Energy Materials and Solar Cells* 201, 110028.
- S. S. Raiman, D. Sulejmanovic, J. M. Kurley, J. J. Lee, C. G. Parker and B. A. Pint (2021) “Technical Assessment of Materials Compatibility in Molten Salt Reactors” NRC Report TLR-RES/DE/CIB-CMB-2021-03, ADAMS Accession No. ML21084A039, March 2021.
- S. S. Raiman, J. M. Kurley, D. Sulejmanovic, A. Willoughby, S. Nelson, K. Mao, C. Parish, M. S. Greenwood and B. A. Pint (2022) “Corrosion of 316H Stainless Steel in Flowing FLiNaK Salt,” *Journal of Nuclear Materials* 561, 153551
- J. J. Rehr and R.C. Albers (2000) “Theoretical approaches to x-ray absorption fine structure,” *Reviews of Modern Physics*, 72, 621-654.
- J. J. Rehr, et al. (2010) “Parameter-free calculations of X-ray spectra with FEFF9,” *Physical Chemistry Chemical Physics*, 12, 5503-5513.
- A. L. Rollet, S. Godier, and C. Bessada, “High temperature NMR study of the local structure of molten LaF₃-AF (A = Li, Na, K and Rb) mixtures,” *Physical Chemistry Chemical Physics*, 10, 3222-3228.
- A. L. Smith, et al. (2019) “In situ high-temperature EXAFS measurements on radioactive and air-sensitive molten salt materials,” *Journal of Synchrotron Radiation* 26, 124-136.
- Y. F. Su, P. I. M. Stack, C. J. Stephens, K. A. Kane, S. Dryepondt, R. Pillai, B. A. Pint and B. M. Tossey (2021) “Quantifying High Temperature Corrosion,” NACE Paper C2021-16805, Houston, TX.
- D. Sulejmanovic, J. M. Kurley, K. Robb, S. Raiman (2021) “Validating Modern Methods for Impurity Analysis in Fluoride Salts,” *Journal of Nuclear Materials*, 553, 152972.
- H. Sun, J. Wang, Z. Lia, P. Zhang, X. Su, “Corrosion behavior of 316SS and Ni-based alloys in a ternary NaCl-KCl-MgCl₂ molten salt,” *Solar Energy* 171 (2018) 320–329

- K. Vignarooban, X. Xu, K. Wang, E.E. Molina, P. Li, D. Gervasio, A.M. Kannan (2015) “Vapor pressure and corrosivity of ternary metal-chloride molten-salt based heat transfer fluids for use in concentrating solar power systems, *Appl. Energy* 159, 206–213.
- R. Viswanathan and W. Bakker (2001) “Materials for Ultrasupercritical Coal Power Plants—Boiler Materials: Part I,” *Journal of Materials Engineering and Performance* 10(1), 81-95
- D. C. Vreeland, E. E. Hoffman and W. D. Manly (1953) “Corrosion Tests for Liquid Metals, Fused Salts at High Temperatures,” *Nucleonics* 11(11), 36-39.
- S. Watanabe, et al. (2006) “XAFS analysis of molten rare-earth-alkali metal fluoride systems,” *Journal of Alloys and Compounds*, 408, 71-75.
- J. R. Weeks (1971) “Lead, bismuth, tin and their alloys as nuclear coolant,” *Nucl. Eng. Des.* 15, 363–372.
- R. N. Wright (2014) “The Effect of Cold Work on Properties of Alloy 617,” Report INL/EXT-14-32965, Idaho National Laboratory, Idaho Falls, ID.
- F. Wu, et al. (2019) “Elucidating Ionic Correlations Beyond Simple Charge Alternation in Molten $MgCl_2$ -KCl Mixtures,” *Journal of Physical Chemistry Letters*, 10, 7603-7610.
- G. L. Yoder Jr, A. Aaron, B. Cunningham, D. Fugate, D. Holcomb, R. Kisner, F. Peretz, K. Robb, J. Wilgen, D. Wilson (2014) “An experimental test facility to support development of the fluoride-salt-cooled high-temperature reactor,” *Annals of Nuclear Energy* 64, 511-517
- J. P. Young, G. Mamantov, J. E. Coffield and S. Dai (1993) “In-Line Sensors for Electrolytic Magnesium Cells,” Technical Report ORNL/M-3003, Oak Ridge National Laboratory, Oak Ridge, TN.
- J. Zhang, C. W. Forsberg, M. F. Simpson, S. Guo, S. T. Lam, R. O. Scarlat, F. Carotti, K. J. Chan, P. M. Singh, W. Doniger, K. Sridharan, J. R. Keiser (2018) “Redox potential control in molten salt systems for corrosion mitigation,” *Corrosion Science* 144, 44–53
- G. Zheng, L. He, D. Carpenter, K. Sridharan (2016) “Corrosion-induced microstructural developments in 316 stainless steel during exposure to molten Li_2BeF_4 (FLiBe) salt,” *Journal of Nuclear Materials* 482, 147-155.